

UNIVERSITA' DI GENOVA
Dottorato di Ricerca in Meccanica e Costruzione di Macchine
XVII Ciclo
Settore Scientifico Disciplinare ING-IND/14

Marco La China

TESI DI DOTTORATO

**SHAPE STABILITY OF
THE LHC SUPERCONDUCTING DIPOLE:
MECHANICAL MODEL AND
EXPERIMENTAL INVESTIGATIONS**

Tutor:

Prof. Alessandro Rebora

Supervisor:

Dr. Walter Scandale

May 2006

Contents

I	INTRODUCTION	1
1	Introduction	3
1.1	Particle accelerators	3
1.2	Dipole magnets for accelerators	3
1.3	Problem definition	5
1.4	Aim of the work and tools	6
1.5	Contents of the thesis	7
1.6	Structure of the thesis	8
2	The Large Hadron Collider and its main dipole	11
2.1	The Large Hadron Collider	11
2.2	The superconducting main dipole	12
2.2.1	The cable	15
2.2.2	The superconducting coil	17
2.2.3	The magnetic field	18
2.2.4	The collars	20
2.2.5	The yoke and the shrinking cylinder	22
2.2.6	The cold mass and the cryostat	23
2.2.7	The composite support posts	24
2.2.8	Magnet extremities	25
2.3	Cold mass geometry	26
2.3.1	Tolerance on the shape	26
2.3.2	Tolerance on the interconnecting components	27
2.3.3	Tolerance on the multi-polar correctors	27
3	The superconducting dipole models	29
3.1	Introduction	29
3.2	The analytical model	29
3.3	The 3D finite element model	32
3.4	The 2D finite element model	36

II QUALITY CONTROL OF DIPOLE GEOMETRY 39

4	Phenomenology of dipole shape geometrical susceptibility	41
4.1	Introduction	41
4.2	Characteristic parameters of cold mass shape	42
4.3	Errors on Sag	43
4.4	Cold mass End positions	48
4.5	Curvature correction	52
4.6	Cold mass shape in vertical plane.	54
4.6.1	Measured flexions.	55
4.6.2	Intrinsic shape and gravity effect	56
4.7	Summary	59
5	Geometrical issues on dipole production	61
5.1	Introduction	61
5.2	Accuracy of geometric tolerance checking procedure	61
5.2.1	Measuring procedure	61
5.2.2	Saw-tooth effect	64
5.2.3	Parameters for analysis and experimental results	66
5.2.4	Numerical simulation and experimental result comparison	67
5.3	Influence of test bench planarity on field orientation measurement	70
5.3.1	The main field angle	70
5.3.2	Poorly planar bench influence test	71
5.3.3	Results	73
5.3.4	Evaluation of the cold mass torsional rigidity	76
5.4	Summary	77

III ANALYSIS OF PRE-OPERATIVE AND OPERATIVE PHASES 81

6	Geometrical susceptibility in pre-operative stages.	83
6.1	Introduction	83
6.2	Mechanical interference between the dipole and the cryostat.	83
6.2.1	Test set-up	84
6.2.2	Test result	84
6.2.3	Model description	88
6.2.4	Measurements and simulation comparison	88
6.3	Cryo-dipole transport, handling and stocking.	90
6.3.1	Transport specifications	91
6.3.2	The finite element model	93
6.3.3	Results	95
6.4	Summary	106

7	Operational experience on prototype and pre-series dipoles	109
7.1	Introduction	109
7.2	String2 and monitoring system	109
7.2.1	String powering	112
7.2.2	String quenches	114
7.2.3	String cool-down and warm-up	117
7.3	Loads on central composite support in working conditions.	118
7.4	Modeling of cross-section deformations in working conditions.	120
7.4.1	Mechanical modeling versus measurements at 1.9 K	121
7.5	Summary	122
8	Conclusions	125
IV	APPENDICES	129
A	Analytic beam model.	131
B	Custom finite element model	137
B.1	Element definition	138
B.2	Node locations	138
B.3	Element nodal connectivity	139
B.4	Element stiffness matrix	139
B.5	From local to global	141
B.6	Assembly of global stiffness matrix	143
B.7	Concentrated loads and constraints	144
B.8	Nodal solution	146
B.9	Element solution	146
C	Azimuthal pre-stress in the shrinking cylinder	149
D	Sag error computation	153
E	From extremity to central foot displacement.	155
F	Screw modeling in transport restraints.	157
G	Montecarlo based multi-station measurement simulation	163

List of Figures

2.1	Mechanical structure of a short-prototype dipole cold mass.	13
2.2	The cryo-dipole cross-section.	13
2.3	Cross-section of Rutherford type cable.	15
2.4	The cable insulation.	15
2.5	Schematic view of the superconducting coil.	17
2.6	The superconducting coil cross-section in the LHC dipole.	17
2.7	Generation of a pure dipole by a $\cos \theta$ current distribution.	18
2.8	The collared coil.	20
2.9	The pole shims.	22
2.10	The cold mass cross-section.	22
2.11	The composite supporting post for the dipole cold mass.	25
2.12	The cold mass end cover.	25
2.13	The tube axes shape in the horizontal plane.	27
2.14	The tube axis shape in the vertical plane.	27
2.15	The multipolar correctors and the adjustable support.	28
3.1	The 2D slim beam model. See Appendix A for details.	30
3.2	A cut of the cryo-dipole finite element model.	33
3.3	A slice of the cryo-dipole finite element model.	35
3.4	The finite element model of the cold mass cross-section.	37
3.5	Collars and coils cross section. Short and long collars are put alternatively up and down.	38
4.1	Theoretical geometry of the cold bore tube in assembling condition. Horizontal plane (curvature strongly magnified).	42
4.2	Typical measurement outcome. Interpolating polynomials and relevant points for analysis are plotted along with the tolerance range. . .	43
4.3	Sag error trend along the production of each firm. Average and standard deviation are computed on samples of 30 cold mass per time. X-axis reports cold mass serial numbers.	45
4.4	The three typical cold mass shape evolutions observed in the early production. The thin dotted lines envelop the early tolerance range (± 0.3 mm in the extremities)	46

4.5	Sag change across pre-operative stages for the first 11 reshaped cold masses (left plot) and for the first 13 non-reshaped cold masses (right plot).	47
4.6	Distribution of Sag error after the manufacturing and after the cold tests for all the magnets produced and tested up to November 2005 (880 cold masses, 1760 Sags).	48
4.7	Distribution of End positions in the transversal plane at four pre-operative stages: ‘After Manufacturing’, ‘Arrival at CERN’, ‘After Cryostating’ and ‘After Cold Test’; 34 cold masses, 136 Ends.	49
4.8	Vertical shape of cold mass 1138 as measured in the industry (ITP20) and at CERN (WP08). In the top graph WP08 data are the ones stored in the database, in the bottom graph they are corrected imposing the same vertical position of the supports.	50
4.9	Distribution of normalized End positions in the transversal plane at four pre-operative stages (34 cold masses, 136 Ends) and just after the manufacturing and after the cold test (880 cold masses, 3520 Ends).	51
4.10	Effect of ‘Per Magnet’ (top graph) and ‘Per Firm’ (bottom graph) shape correction on the same magnet. The arrow shows the central support shift	53
4.11	Distribution of End horizontal displacements from ITP20 to WP08 with no correction (left), ‘Per Magnet’ correction (center) and ‘Per Firm’ correction (right).	54
4.12	Vertical shape of magnet 2022 as measured right after the manufacturing (ITP20) and at the last pre-operative stage (WP08). Both raw data (solid lines) and 10^{th} degree polynomial interpolation (dashed lines) are plotted.	55
4.13	Result of best fit of magnet 2038 vertical deflection on two supports (top graph) and on three supports (bottom graph).	58
4.14	Original axis shape of magnet 2038 derived from measurement on two and on three supports (solid and dashed line, respectively).	59
5.1	Theoretical geometry of the cold mass in assembly condition in the horizontal plane. The four stations for the laser tracker around the dipole are also shown.	62
5.2	Network points and laser tracker positions around the cold mass.	63
5.3	Horizontal (upper graph) and vertical (lower graph) profiles of the dipole axes with respect to the theoretical shape.	64
5.4	From top to bottom: Horizontal (1^{st}) and vertical (2^{nd}) profiles of the dipole inner tube axis as measured from Connection and Non-Connection ends, horizontal (3^{rd}) and vertical (4^{th}) difference between measurements from Connection and Non-Connection ends.	65
5.5	Graphical output produced by numerical simulation.	68

5.6	Set Up layout and reaction forces in supports. The support configuration shown is ‘OIO’: 3mm shims under the three cold mass supports	72
5.7	Front view of jig and details for installation on end cover.	72
5.8	Twist along cold mass in the hypothesis of linear torsional behavior. .	73
5.9	Distribution of errors associated to the geometrical plane evaluation based on end cover orientations.	74
5.10	Magnet and support section by a transversal plane containing \mathbf{R}_B . . .	76
6.1	Cryo-dipole top view. Applied force and allowed sliding directions in the cold mass/cryostat interfaces are shown.	84
6.2	Schematic of test set-up.	85
6.3	Force-displacement relation in a transversal plane at cold mass extremity. Laser tracker data.	85
6.4	Horizontal and vertical displacement of loaded end. Interferometer data.	86
6.5	Loaded end horizontal displacement vs. applied load.	87
6.6	Axis shape in the horizontal plane under load and rest conditions. Arrows indicate support positions.	87
6.7	Measured and simulated axis deflections in horizontal plane for an applied force of 15.4kN at one extremity (top) and ~ 23 kN at both the extremities.	89
6.8	Nominal transport restraint.	91
6.9	Light transport restraint.	92
6.10	Front view of nominal and light transport restraints.	92
6.11	Cremonian type transport restraint.	92
6.12	Transport configuration with three light restraints.	93
6.13	Clockwise from top left: very rigid transport restraint composed of a net of beams, light transport restraint, three light transport restraints configuration, Cremonian type transport restraint.	94
6.14	Distribution of Tresca equivalent stresses [MPa] in the light restraints induced by a 4 m/s ² longitudinal acceleration. Top image is Connection side, bottom is Non-Connection (Lyre) side.	99
6.15	Distribution of Tresca equivalent stresses [MPa] in the modified light restraints induced by a 4 m/s ² longitudinal acceleration. Top image is Connection side, bottom is Non-Connection (Lyre) side.	100
6.16	Distribution of Tresca equivalent stresses [MPa] in the light restraints induced by a 5 m/s ² lateral acceleration. Top image is Connection side, bottom is Non-Connection (Lyre) side.	101
6.17	Distribution of Tresca equivalent stresses [MPa] in the modified light restraints induced by a 5 m/s ² lateral acceleration. Top image is Connection side, bottom is Non-Connection (Lyre) side.	102
6.18	Effect of a 5 m/s ² lateral acceleration on a cryo-dipole equipped with 3 light restraints. Lateral displacement [m] in the middle cross section.	103

6.19	Effect of a 5 m/s^2 lateral acceleration on a cryo-dipole equipped with 3 modified light restraints. Lateral displacement [m] in the middle cross section.	103
6.20	Effect of a 5 m/s^2 lateral acceleration on a cryo-dipole equipped with Cremonian type restraints. Lateral displacement [m] in the middle cross section.	104
6.21	Effect of a 5 m/s^2 lateral acceleration on a cryo-dipole equipped with ideal restraints. Lateral displacement [m] in the middle cross section.	104
7.1	String2 magnets layout (LHC standard cell).	109
7.2	Original SOFO system.	110
7.3	Double pass delay line replacing the measuring fiber.	111
7.4	Installation of the SOFO modified sensor.	112
7.5	Energization effect on horizontal displacement and outer cold mass diameter variation of prototype magnet MB2.	113
7.6	Horizontal displacement and diameter variation induced by quench at 11.75 kA	115
7.7	Horizontal shift and temperature raise provoked by quench at 11.75 kA	116
7.8	Different possible scenarios featuring the same extremity horizontal displacement ΔS (view of X section is out of scale).	119
7.9	Diameter variation versus current intensity for two magnets (MB2, MB5) and two current ramps (ct1,ct2).	121
A.1	Thin beam model of cold mass on three supports. Model is composed of four beams.	132
A.2	Distributed and concentrated loads in the vertical plane. Local reference system of each beam is also shown.	133
A.3	Right inner beam (n. 3).	133
B.1	3D beam.	138
B.2	Discretization of cold mass by 10 beams and 11 nodes (numbered in squares and circles , respectively).	139
B.3	System of four elements and four nodes (numbered in squares and circles, respectively). Element stiffness matrices are assembled together to form the global stiffness matrix.	143
C.1	Equivalent system to model the stress distribution in the cold mass cross-section.	150
D.1	Ideal representation of magnet axis shape in horizontal half plane. Arc 1 has nominal sagitta, Arc 2 bigger than nominal.	153
E.1	Cold mass deformation associated to a curvature increase.	155

F.1	Detail of setscrew model. Two layers of radial beams transmit the load to the hole walls as the first three/four threads in reality do. . . .	158
F.2	Detail of bolt model. The radial beams transmit the load to a circular surface around the hole edge.	158
F.3	Detail of cryostat/light restraint interface.	159
F.4	Detail of light restraint/cold mass interface. For every screw a network of beams connects the screw extremity node (orange dot) to the 8 nodes (blue dots) of the closest tetrahedral element.	159
F.5	Setscrew equivalent spring model.	160
F.6	Bolt equivalent spring model.	160
F.7	Equivalent stiffness of radial beams $K = F/s$	160
G.1	Algorithm flowchart.	164

List of Tables

2.1	Dipole parameters.	14
2.2	Strand and cable characteristics.	16
2.3	Multipole classification.	20
2.4	Figure of merit for structural support materials.	24
3.1	Degrees of freedom (DOF's) and wave front maximum size for different mesh densities.	35
3.2	Young's modulus, Poisson's ratio and tangential elasticity of materials implemented in the cryo-dipole finite element model.	36
4.1	Convention for Sag error sign.	43
4.2	Sag errors of cold mass after manufacturing (ITP20 stage)	46
4.3	Effect on extremity positions of different kinds of shape correction. . .	53
4.4	Peak to peak analysis of measurements on two and on three supports. Number of magnets per sample is given in parentheses.	56
4.5	Values of flexural rigidity EI computed from measurements of cold mass on two and on three supports	57
5.1	Accuracy of the LTD500 LEICA laser tracker.	62
5.2	Statistical values of rotation and shift between opposite stations and saw-tooth height. Values are given in rad for p and in mm for q and h . 66	
5.3	Results of the numerical simulation after 100 iterations. Values in the right table include ground accommodation. Values are in rad for p and in mm for q and h	69
5.4	Data from test 1 (top) and 2 (bottom). See text for details.	75
6.1	Elasticity of materials used in the FEM	88
6.2	Maximum allowed accelerations during transport.	90
6.3	Sum of forces on support bases and transport restraints induced by a 4 m/s ² longitudinal acceleration.	96
6.4	Sum of forces on support bases and transport restraints induced by a 5 m/s ² lateral acceleration and by a 7 m/s ² vertical acceleration. . . .	97
6.5	Sum of forces on support bases and transport restraints induced by a 30 K temperature difference.	98

6.6	Relative cold mass-cryostat extremity displacement in longitudinal direction induced by a 30 K temperature difference.	105
6.7	Lateral (u_x) and longitudinal (u_y) displacements of the central support top respectively induced by a 5 m/s ² lateral and 4 m/s ² longitudinal acceleration.	105
6.8	Maximum longitudinal stress in the screws connecting the restraint to the cold mass. Values are scaled from a 1 g lateral acceleration simulation.	105
6.9	Forces on central support and stress distributions in the 3 modified transport restraints for all the loads.	106
7.1	SOFO main features.	112
7.2	Energization-Induced Displacements	114
7.3	Displacements Induced by Quenches	116
7.4	Displacements Induced by Slow Cool-Down	117
7.5	Residual Displacements after String Shut-Down	118
7.6	Displacements of extremities (measured) and of central support (computed).	120
A.1	Polynomial coefficients for outer beams (n. 1 and 4) and inner beams (n. 2 and 3). Contributions of distributed force q , concentrated force F and moment M are given separately. Specific expressions of q , F and M are given in Table A.2.	133
A.2	Specific parameters of beams.	134
A.3	Internal moments exchanged between adjacent beams.	135
A.4	Parameters for local to global coordinate transformation.	135
C.1	Fictitious thermal expansion coefficient used to implement the pre-stress exerted by the shrinking cylinder.	152
F.1	Geometrical properties of setscrew equivalent beam system.	161
F.2	Geometrical properties of bolt equivalent beam system.	162

Part I

INTRODUCTION

Chapter 1

Introduction

1.1 Particle accelerators

Particle accelerators [1] are machines that accelerate charged elementary particles to high kinetic energy. Particles are usually electrons or positrons or ionized atoms. A beam of such particles is then smashed against other particles. The other particles may be stationary atomic nuclei in a fixed target or fast moving particles in another beam who is brought into a head-on collision with the first beam. Collisions with very high energy beams correspond to very high temperatures in the interactions. The study of matter in these extreme conditions can be related to the conditions prevailing in the Universe in the first moments after the so-called ‘Big Bang’.

In circular accelerators the energy of the beam is increased into closed circular. Since the particles travel in a straight line if no external forces are acting on them, in these machines a magnetic field imparts a Lorentz force to them inducing a curved path. The amount of curvature of the orbit depends on the strength of the magnetic field and on the energy of the particle: the greater the magnetic field, the greater the curvature; the greater the energy, the less the curvature.

As particle energy and momentum increase with every pass around the track, the strength of the magnetic field is gradually augmented. The increase of energy and magnetic field are synchronized, ensuring that the particles circulate in the same path every time: we say that the field ‘ramps up’ with particle energy increase. Circular accelerator producing a synchronized increase of energy and magnetic field are called synchrotron.

1.2 Dipole magnets for accelerators

Dipole magnets for accelerators [1] fulfill the requirement of generating the magnetic field necessary to force the beam into a circular orbits. They have two poles producing field lines in the aperture of the magnet (where the beam passes) perpendicular to the plane of the particle beam orbit. They are in general electro-magnets, with

magnetic fields generated by the flow of electric current in the wire winding of their coils. The coils are encased in a ferromagnetic yoke which provides a return path to close the field lines and to increase the field in the aperture. Depending on the field strength several designs are possible :

- low field (up to 2 T) iron-dominated magnets;
- high-field rectangular magnets;
- high-field round magnets;
- very high-field magnets.

In the iron-dominated magnets the peak magnetic field is limited by the iron saturation at about 2 T. The field shape depends principally on the shape of the iron yoke, which determines the 'good field' region where the beam can travel safely. In most of the cases, such magnets are resistive, although there are examples of iron-dominated superconducting magnets, where the yoke can remain either at ambient or at cryogenic temperature.

For fields above 2 T the magnets should be superconducting and the coil should produce the additional magnetic flux. The coil becomes larger and the placement of the conductors determines the shape and the quality of the field. Laminated steel spacers called collars are in general positioned around the coils and inside the yoke in order to confine the conductors and keep them in place. In many cases, the yoke itself is used to support the coils. These magnets, called high-field magnets, may be rectangular or circular. In the high-field rectangular magnets [2], the conductors are placed above and below the aperture and the coil features a rectangular shape. In the round magnet design, the coil is placed in a cylindrical shell around the magnet bore. This coil configuration is called the $\cos\theta$ configuration, since the current distribution in the cylindrical shell approximately varies as the cosine of the angle from the mid-plane. For a colliding beam accelerator in which counter rotating beams collide, a magnet design option is the 'two-in-one' $\cos\theta$ design, where the two sets of coils for the two beams are combined in a single iron yoke [3]. The $\cos\theta$ configuration is predominantly used for magnet in the 3 to 10 T range with Nb-Ti superconductors and up to 13 T with Nb₃Sn superconductors. Dipoles with the $\cos\theta$ configuration and Nb-Ti superconductors have been built for the following accelerators:

- Tevatron at Fermilab, Chicago, USA: 4.4 T at 4.6 K;
- HERA at DESY, Hamburg, Germany: 4.7 T at 4.6 K;
- RHIC at Brookhaven, New York, USA: 3.5 T at 4.6 K;
- SSC (project canceled in October 1993) at SSCL, Texas, USA: 6.6 T at 4.4 K;
- LHC (completion date 2007) at CERN, Geneva, Switzerland: 8.3 T at 1.9 K.

For very high-field magnets, i.e. for field higher than 10 T, two new designs have been proposed: the common coil design [4] and the block magnet design [5]. Both use the two-in-one configuration with Nb₃Sn superconductors.

1.3 Problem definition

In superconducting magnets the conductors are placed close to the bore in order to reach an high magnetic field in the region where the beam passes. The main consequence of this feature, compared to the resistive magnets where the conductors are distant and the iron yoke extends toward the beam tube, is that the shape and the quality of the magnetic field strongly depends on the position of the conductors. In a circular accelerator, in order to guarantee a beam stable during the operation, the magnetic field errors must be controlled at levels of the order of less than 10^{-4} of the main field. This means that the position of the conductors must be controlled with a precision greater than 0.1 mm. The geometry of the whole magnet assembly consequently gains primary relevance for the machine performance so that the tight tolerance respect is strictly mandatory from the assembly to the operational phase. The pre-operative life of a superconducting magnet like the LHC dipole goes indeed through several different events as road transports, cryostating, cryo-magnetic testing and long term storage that can consistently affect the shape accuracy.

The dipole shape susceptibility is due to three concurrent factors hereby explained. The first is the overall small rigidity due to the discontinuous internal structure made of varied components forced together by a relatively thin shell. The second is that the dipole slightly curved geometry, designed to closely follow the circular beam trajectory, is shaped in a press and fixed by means of a longitudinal welding; the final geometry is thus determined by the equilibrium between the forces exerted by the straight internal components and the two bent shells welded together. The third is the harshness of the thermal, magnetic and mechanical combined loads of both static and dynamic nature experienced by the dipole.

Other than to preserve the correct geometry up to the operative stage it is essential to guarantee its long-term stability. In operative conditions, in fact, the magnets are hosted in a vacuum vessel so that after the installation no access is possible any more to provide maintenance or to adjust the position with respect to the beam trajectory. Any further alignment can only be implemented through the cryostat (vacuum vessel) supports so that the knowledge of the cryo-dipole system behavior is fundamental.

The LHC challenge is made tougher by the large scale need of dipoles to fill the 70 % of the 27 km-long ring. To manage the series production of such a compound and pioneering item CERN has established a partnership with three leading mechanic industries. The whole production is equally divided among the firms to which CERN provides the know-how, the instruments and the feed-back necessary to take corrective actions on the manufacturing procedure.

1.4 Aim of the work and tools

The aim of this work is the study of the geometry of the main superconducting dipole for the Large Hadron Collider from the manufacturing process throughout the pre-operative stages to predict the respect of the tight tolerance, imposed by the beam dynamic, in both nominal and chancy working conditions. Expected and unexpected situations have been approached through the development of dedicate models and tests with the purpose of evaluating their impact on magnet geometry.

As the cold mass is a new and complex assembly, the investigatory part played a fundamental role in the research activity.

To carry out the dimensional inspections we use 3D laser trackers positioned around the cold mass. The complete picture of the magnet 3D shape, with an accuracy of few tenths of millimeter over 15 m is then obtained by the combination of the different laser tracker data.

To monitor the cold mass deformations in operating condition we use an optical device specifically developed at CERN in collaboration with a specialized external partner. The device, fulfilling very special requirements due to environmental conditions, is based on optical interferometry and allows us to detect displacement of hundredths of millimeters between two bodies with a temperature difference of 300 K.

In our study we used structural models of different complexity for different purposes. For example we used analytical models in conjunction with the cold mass geometry database to simulate the overall effect of individual geometry corrections or to discriminate elastic from inelastic measured deformations. By means of finite element models, instead, we investigated the effect of mechanic loads as induced by road transport, or the effect of electro-magnetic forces arising in working conditions.

As the assembly complexity prevents from deducing some of the main mechanical properties we set-up different dedicated tests and we evaluated the desired properties from the comparison with analytical or finite element models.

To summarize, the observations were carried out by mean of:

- customized interferometer;
- laser tracker;
- tilt-meters.

Whereas the simulations were based on:

- finite element method (ANSYSTM);
- analytical models;
- Montecarlo algorithm.

More in detail all the finite element models were personally developed from scratch except for the 2D one. The same applies to all the analytical models, developed using MATLABTM, a commercial software especially efficient in matrix handling. The Montecarlo simulations, the tools for the data analysis and the routines to interface the analytical model and the geometry database were also entirely personally developed using MATLABTM. Tests were carried out, whenever possible, in team with colleagues and metrology experts. Measurements of cold mass deformations in operating conditions by means of interferometer were personally taken and analyzed.

1.5 Contents of the thesis

Our study begins from the statistical analysis of the dipole geometry evolution across all the successive steps from the assembly to the operative phases. Two characteristic parameters have been chosen to easily control the shape variations; indeed we gave primary importance to the magnet extremity positions and to the horizontal curvature. On one hand, magnet extremities contain the multi-polar correctors to correct field imperfections and need to be placed within few tenths of millimeter around the beam orbit. On the other hand, the overall curvature is crucial to ensure the superconducting coil shape and the mechanical clearance for the bunch of particles that must travel at a safe distance from the vacuum chamber walls. Therefore our parameters are the extremity positions and the horizontal sag of the curved part.

The ratio between the magnet dimensions and the required tolerance causes the tolerance check himself to be a not trivial task to accomplish. The related custom measuring procedure has thus been simulated through Montecarlo based algorithm to estimate the best accuracy achievable in the dimensional inspection performed in the companies and at CERN.

The intrinsic mechanical qualities of the superconducting magnet design cause the magnet shape to be easily influenced by the measuring bench planarity. Dedicated tests have been carried out to evaluate the measuring bench requirements to grant reliable measurements.

To compensate the non homogeneous production a new alignment strategy has been proposed and the consequences have been simulated through the analytical structural model. The interaction between adjacent magnet connected through flexible bellows has been simulated and the effects on their alignment with respect to the beam orbit have been studied as a base for a sorting strategy.

The specifications to prevent structural damages during the road transport from the companies to CERN are based on the evaluation of the peak stresses consequent to dynamic load. Aware of the considerable magnet inertia and small rigidity that could limit the harmfulness of dynamic loads we studied the effect of inertial loads. We used the 3D finite element model of the cold mass inside the cryostat and we applied inertial loads of different intensity and along different directions

to simulate acceleration and deceleration arising during road transport, handling and installation. We considered also different transport restraints and cryostat/cold mass interfaces. The behavior of the constraint at the cold mass/cryostat interface has been investigated by mean of tests and simulations.

We carried out the statistical analysis on the shape parameters at the magnet reception at CERN, after the cryostating and after the cryo-magnetic test in order to monitor the geometrical stability. We could therefore identified the situations that affect more the cold mass shape.

Potential cold mass shape modifications induced by nominal and accidental operating modes are obviously of primary relevance. The cold mass shape and position inside the cryostat have been monitored during thermal cycles, current ramp cycles and resistive transitions.

The magnetic performance of a superconducting magnet like the dipole is strictly related to the coil cross-section layout. During the energization phase the coil is subjected to increasing Lorentz forces that not only deform the cable but even the whole magnet cross-section. To evaluate coil deformations we use a detailed bi-dimensional finite element model of the magnet cross section. Since the coil deformation during energization cannot be directly measured we compared the simulation results with the cross section diameter variation acquired with the interferometer. The effects of quench on cold mass geometry has been analyzed and interpreted, consequences on support integrity have been discussed.

1.6 Structure of the thesis

The thesis is divided into three parts. First part contains the introductory Chapter 2 to present some aspects of particle accelerators technology and lead into the thesis subject. Chapter 2 gives details on the LHC project and describes the mechanical design of its main bending dipole. Chapter 3 explains the different models used to analyze the mechanical behavior of the magnet.

The second part focuses on the issues related to the series production of the magnets. Chapter 4 analyses statistically the metrology of the produced dipoles. Chapter 5 is dedicated to the examination of the tolerance checking procedure implemented in the industries and at CERN.

Third part is dedicated to the pre-operative and operative phases. Chapter 6 reports the study of the interaction between the cold mass and the cryostat and the performance of different types of transport restraints. Chapter 7 describes the effect of operative modes on the overall geometry of the cold mass and of the cross-section. Chapter 8 is dedicated to the conclusions. Appendix A illustrates the implementation of the analytical model. Appendix B gives general directions on how to implement a 3D beam model based on finite element method. Appendix C contains details on the implementation of the pre-stress in the ANSYSTM 3D finite element model. Appendix D demonstrates the criterion for choosing a 2nd order polynomial

curve to fit the magnet shape to compute the horizontal sag variation. Appendix F contains details on the implementation of the screws in the Finite Element Model of the transport restraints. Appendix E clarifies the geometrical relation between the extremities and the central part of the cold mass. In Appendix G is reported the flow diagram of the numerical simulation used in Chapter 5.

Chapter 2

The Large Hadron Collider and its main dipole

2.1 The Large Hadron Collider

The Large Hadron Collider [3] is a circular accelerator under construction at CERN (European Laboratory for Particle Physics): the project has been approved by the CERN Council in December 1994 and it will be completed in 2007.

The machine will replace the LEP collider (Large Electron Positron collider), inside the 27 km underground circular tunnel in the Geneva area, and will provide proton-proton collisions with a center-of-mass energy of 14 TeV.

The particle beam will be pre-accelerated by three different machines (LINAC, PS and SPS) to 450 GeV and sent to the LHC. This phase is called the *injection*. The beam energy will be then increased up to the 7 TeV in the LHC itself. This phase is called the *acceleration*. The collisions will occur in four interaction points where four experiments (ALICE, CMS, LHC-b and ATLAS) are placed. This phase is called the *interaction*.

Inside the LHC, superconducting magnets aligned with a precision of a few tenth of millimeters are used to bend and focus the particle trajectories [6]. Namely:

- dipoles produce the main vertical magnetic field, perpendicular to the particle direction, used to deflect particle motions to circular trajectories;
- quadrupoles produce a field that is null in the center of the vacuum chamber and linearly dependent from the distance to the center, whose purpose is to focus the beam.

In the LHC tunnel, 1232 main dipoles (MB: main bending) and 386 main quadrupoles (MQ) will be installed.

2.2 The superconducting main dipole

A vertical magnetic field of 8.3 T is necessary to deflect a proton beam, accelerated to an energy of 7 TeV, along the circular trajectory of the 27 km-long LHC tunnel. This level of magnetic field requires the use of superconducting magnet technology. There are three large accelerators in operation based on superconducting magnets: the Tevatron (Fermilab, USA), the HERA (DESY, Germany) and the RHIC (Brookhaven, USA). They all make use of classical Nb-Ti superconductors cooled with liquid helium at a temperature slightly above 4.2 K, and their operational fields are 4.4 T for the Tevatron, 4.7 T for HERA and 3.5 T for RHIC. For the LHC it is mandatory to push the field significantly higher, still retaining the well-proven fabrication methods of cables and coils made of Nb-Ti superconductors. The only way of obtaining fields of 8.3 T is to cool the magnets at a temperature of 1.9 K. In fact, at this lower temperature, the critical field and current of the superconducting cables are considerably increased.

Below 2.17 K, helium takes the so-called superfluid state, with much lower viscosity and much greater heat transmission capacity than liquid helium. On the other hand, the enthalpy of all metallic parts and in particular of the superconducting cables is reduced by almost an order of magnitude between 4.2 K and 1.8 K, with a consequent faster temperature rise for a given deposit of energy. This feature calls for particular care in limiting conductor motion. It should be noted that the electro-magnetic forces on the conductor increase with B^2 and so does the stored electro-magnetic energy, calling for a much stronger force-retaining structure than in the previous projects.

The main dipole parameters are listed in Table 2.1, Fig. 2.1 shows the mechanical structure of a dipole (short prototype) whereas Fig. 2.2 the cross-section of the dipole hosted in the cryostat.

Proton-proton colliders require two separate beam channels with fields equal in strength but opposite in directions. For the LHC, the compact ‘two-in-one’ design is adopted, whereby the two beam channels (also called apertures) and their corresponding sets of coils are inserted in a unique structure 15 m long (see Fig. 2.1) and in a single cryostat (see Fig. 2.2). In this arrangement a significant space saving and a cost reduction of 30 % can be fulfilled with respect to two separate structures.

The dipole is composed by two superconducting coils which generate the magnetic field inside the two beam pipes. The coils are surrounded by a containment structure that consists of coil clamping elements, the collar, the iron yoke and the shrinking cylinder, which all contribute to producing the necessary azimuthal pre-compression of the coils and to prevent tensile stresses arising in the coils under the action of the electro-magnetic forces. In operation, the assembly inside the shrinking cylinder, the so-called *cold mass*, is kept at 1.9 K. The cold mass is installed inside a cryostat (see Fig. 2.2) whose main components are a radiation shield at 5 K, a thermal screen at 70 K, and the outer cylindrical wall of the vacuum vessel. All parts between the beam vacuum chamber walls and shrinking cylinder are immersed in

superfluid helium at atmospheric pressure and cooled by means of a heat-exchanger tube, in which two-phase low-pressure helium is circulated and acts as a heat sink.

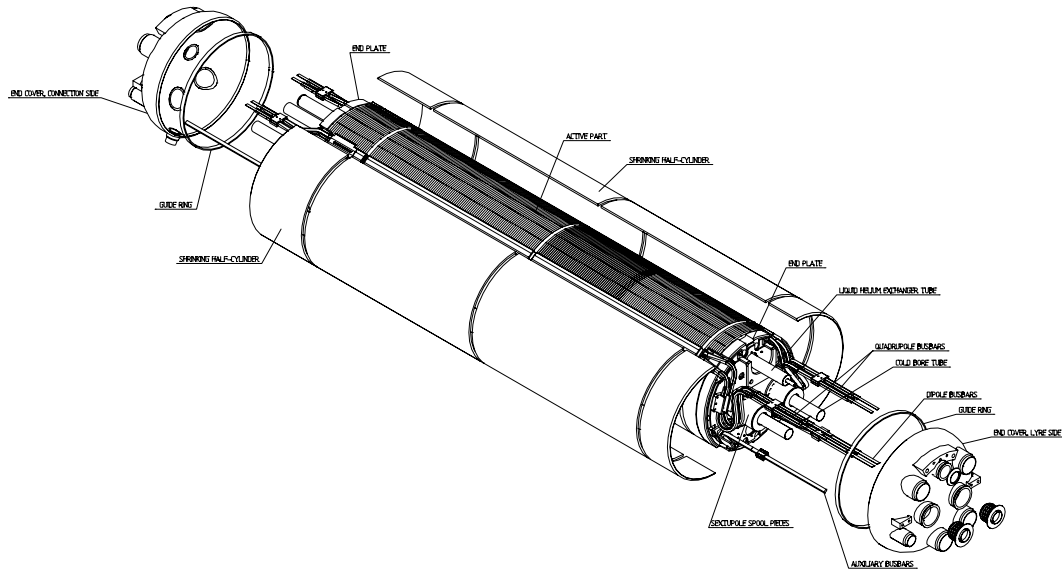


Figure 2.1: Mechanical structure of a short-prototype dipole cold mass.

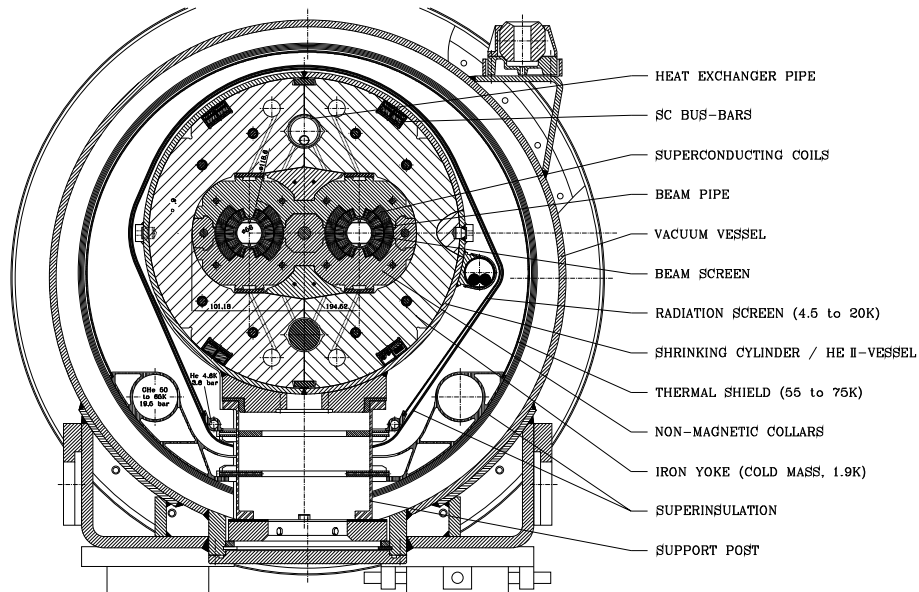


Figure 2.2: The cryo-dipole cross-section.

Table 2.1: Dipole parameters.

Parameter	Value	Units
Injection field (0.45 TeV beam energy)	0.54	[T]
Current at injection field	763	[A]
Nominal field(7 TeV beam energy)	8.33	[T]
Current at nominal field	11850	[A]
Inductance at nominal field	98.7	[mH]
Stored energy (both apertures) at nominal field	6.93	[MJ]
Ultimate field	9	[T]
Current at ultimate field	12840	[A]
Stored energy (both apertures) at ultimate field	8.11	[MJ]
Maximum quench limit of the cold mass (from short sample)	9.7	[T]
Operating temperature	1.9	[K]
Coil aperture at 293 K	56	[mm]
Bending radius at 1.9 K	2803.98	[m]
Magnetic length at 1.9 K at nominal field	14312	[mm]
Coil inner diameter	56	[mm]
Coil outer diameter (incl. insulation to ground)	120.5	[mm]
Coil length (incl. end pieces)	14467	[mm]
Thickness of perforated glass-epoxy	0.5	[mm]
Thickness of insulation to ground	0.75	[mm]
Distance between aperture axes	194.52	[mm]
Collar height	192	[mm]
Collar width	396	[mm]
Yoke outer diameter	550	[mm]
Shrinking cylinder outer diameter	570	[mm]
Length of active part (incl. end plates)	14603	[mm]
Overall length of cold mass	15180	[mm]
Mass of cold mass	27.5	[t]
Outer diameter of cryostat	914	[mm]
Inner diameter of cryostat	890	[mm]
Overall mass of cryo-dipole	31.5	[t]
Forces/coil quadrant at nominal field:		
$\sum F_x$	1.8	[MN/m]
$\sum F_y$	0.81	[MN/m]
Forces/coil quadrant at ultimate field:		
$\sum F_x$	2.1	[MN/m]
$\sum F_y$	0.94	[MN/m]
Axial force at each end at nominal field	0.50	[MN]

At room temperature the cold mass is bent to a 2812.360 m radius of curvature, with a horizontal sagitta of 9.14 mm in the center that at 1.9 K becomes 9.11 mm to match the beam paths. We start now describing in detail the main components of the cryo-dipole.

2.2.1 The cable

The transverse cross-section of the coils for the 56 mm aperture dipole magnet shows two layers of different cables of the Rutherford type (see Fig. 2.3), where strands composed by Nb-Ti filament in a copper matrix are twisted and compressed into a flat two-layers cable. The basic parameters of the two cables are given in Table 2.2. The cable used in the inner layer of the coil has 28 strands and the cable of the outer layer 36 strands. The Nb-Ti filament size is of $7\mu\text{m}$ for the inner layer strand and $6\mu\text{m}$ for the outer layer strand. Cables have a trapezoidal shape, with angles

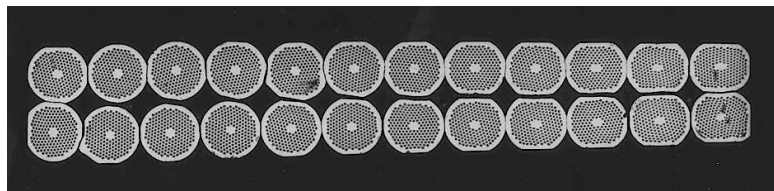


Figure 2.3: Cross-section of Rutherford type cable.

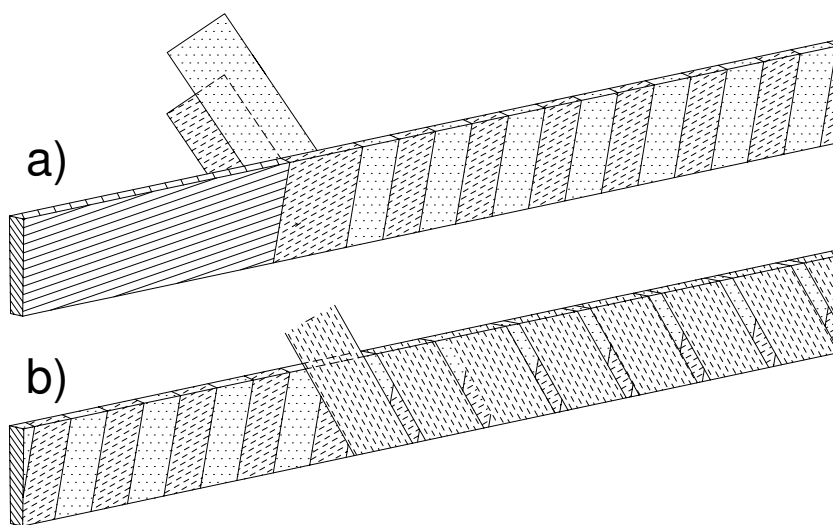


Figure 2.4: The cable insulation.

between bases and oblique sides of 1.25 degrees for the inner layer and 0.90 degrees for the outer layer. These angles, called "keystoning" angles, are used to better obtain the arc shape of the coil.

During operation, the primary sources of heat to the coils are the lost particles and the synchrotron radiation. An additional dynamic heat load results from losses during magnet ramping. This heat increases the superconductor temperature, which reduces the magnet operating margin. Particular care has therefore to be taken to provide a cable insulation which not only withstands the voltage between turns but is also sufficiently porous to let the superfluid helium carry away the heat. The insulation must also be robust, in order not to break during winding and curing.

Table 2.2: Strand and cable characteristics.

	Inner layer	Outer layer
Strand		
Strand diameter [mm]	1.065	0.825
Copper to superconductor ratio	1.6	1.9
Filament size [mm]	0.007	0.006
Number of filaments	8900	6500
RRR	≥ 150	≥ 150
Twist pitch (after cabling) [mm]	18	15
Critical current [A] 10 T, 1.9 K	≥ 515	
9 T, 1.9 K		≥ 380
Cable		
Number of strands	28	36
Cable dimension at 50 MPa		
thin edge [mm]	1.736	1.362
thick edge [mm]	2.064	1.598
width [mm]	15.1	15.1
Transposition pitch [mm]	115	100
Keystone angle (degree)	1.25	0.90
Critical current [A] 10 T, 1.9 K	≥ 13750	
9 T, 1.9 K		≥ 12960

The basic cable insulation, which must safely withstand a turn-to-turn test voltage of 75 V, is composed of two polyimide layers wrapped around the cable, with 50 % overlapping (see Fig. 2.4 a), and another adhesive polyimide tape wrapped onto the cable and spaced by 2 mm (see Fig. 2.4 b). The resulting gap makes the coil porous by setting up channels for superfluid helium, without affecting the mechanical support between turns.

After winding, the adhesive is cured by heating each coil layer in a curing mould, which at the same time gives the final shape and size to the coil.

2.2.2 The superconducting coil

A charged particle q moving with velocity v through a magnetic field B is acted by a force called the Lorentz force, given by

$$\vec{F} = q\vec{v} \wedge \vec{B} \quad (2.1)$$

which is perpendicular to the direction of the magnetic field and of the particle motion. The Lorentz force on beam particles keeps them in the desired orbits through the accelerator. The coil of a dipole is designed to generate in the vacuum pipe

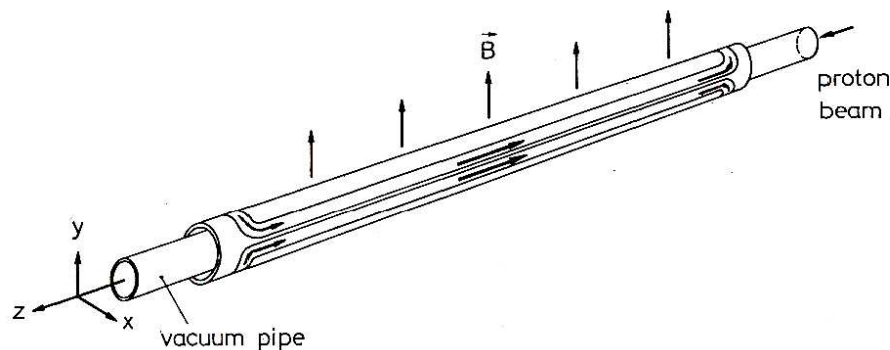


Figure 2.5: Schematic view of the superconducting coil.

a uniform vertical magnetic field, perpendicular to the proton beam, in order to steer the particles in a circular orbit. A schematic view of a superconducting coil is given in Fig. 2.5: the current conductors run parallel to the particle beam over the longest part of the magnet except for the parts on the extremities, so-called *coil heads*, where the conductors make their turn. The heads produce field perturbation; however their length is small compared to the length of the straight section and thus the effect is minimal: in the LHC dipole the heads are about half a meter long, while the total length of the coil is 14.5 m.

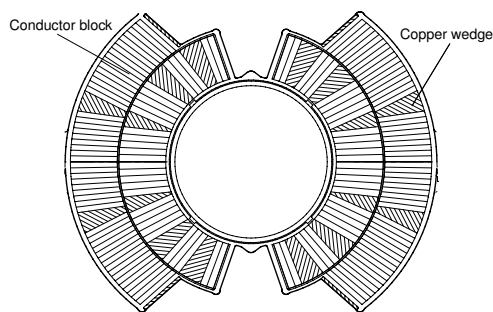


Figure 2.6: The superconducting coil cross-section in the LHC dipole.

The coil cross-section is shaped to make the best use of a superconducting cable and to produce a dipole field of the best possible homogeneity over the whole range of its operational excitation. The conductor distribution selected in the LHC dipole is shown in Fig. 2.6. Conductors are placed on two layers and distributed on six blocks for each quadrant.

Wedge-shaped copper spacers (*copper wedges*) are inserted between blocks of conductors to produce the desired field quality and to approximate a quasi-circular coil geometry, compensating for the insufficient keystoneing of the cables. In the next Section we describe how this kind of conductor distribution generates a dipole field.

2.2.3 The magnetic field

It can be demonstrated [7] that if we consider the arrangement of current distribution represented in Fig. 2.7, where the currents, perpendicular to the sheet, are distributed as a function of the azimuthal angle θ with respect to the x axis, i.e

$$I(\theta) = I_0 \cos \theta, \quad (2.2)$$

the field obtained in the area between the two distribution is a pure and homogeneous dipole.

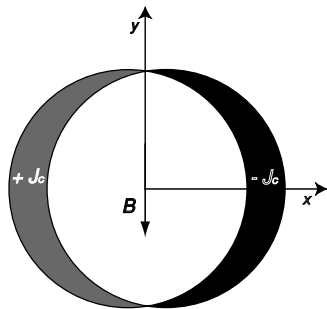


Figure 2.7: Generation of a pure dipole by a $\cos \theta$ current distribution.

Since we want to create inside the beam tube a dipole field as homogeneous as possible, the superconducting coil surrounding the tube should reproduce this current distribution, called $\cos \theta$ distribution. Such configuration is impossible to fabricate with a superconducting cable of constant cross-section as the Rutherford cable, but can be simulated with an arc geometry provided by the keystoneing of the cables and by the copper wedges.

Indeed, the magnetic field generated by the superconducting coil is not a pure dipole, since it is affected also by higher order multipoles (quadrupole, sextupole, etc.). In order to express analytically the magnetic field inside the beam pipe, we remind that in a empty space, free of any currents and magnetized materials, the magnetic field fulfills the following two Maxwell equations

$$\vec{\nabla} \cdot \vec{B} = 0, \vec{\nabla} \times \vec{B} = 0. \quad (2.3)$$

In the central part of the dipole the conductors are parallel to the beam pipe. Under these circumstances one can consider the magnetic field essentially as two dimensional. If we define a complex magnetic field by the equation

$$\vec{B} = B_y + iB_x, \quad (2.4)$$

the Eqs. (2.3) are identical with the Cauchy-Riemann conditions and \vec{B} can be expanded in a power series, obtaining

$$B_y(x, y) + iB_x(x, y) = B_1 \sum_{n=1}^{\infty} (b_n + ia_n) \left(\frac{x + iy}{R_{ref}} \right)^{n-1}, \quad (2.5)$$

where B_1 is the dipole field intensity and R_{ref} is the reference radius set to 17 mm for the LHC dipole. The coordinate system (O, x, y, z) is defined so that the z axis is parallel to the beam line and the y is parallel to the dipole field. O is set at the center of the coil aperture. The coefficients b_1, b_2, \dots, b_n are called the *normal multipole coefficients* and the coefficients a_1, a_2, \dots, a_n are called the *skew multipole coefficients*. The index $n = 1$ describes the dipolar field, $n = 2$ the quadrupolar field, $n = 3$ the sextupolar field, and so on.

We define the the normal (B_n) and skew (A_n) multipoles respectively as

$$B_2 = b_2 B_1, B_3 = b_3 B_1, \dots, B_n = b_n B_1 \quad (2.6)$$

and

$$A_2 = a_2 B_1, A_3 = a_3 B_1, \dots, A_n = a_n B_1. \quad (2.7)$$

A skew multipole A_n is given by a normal multipole B_n rotated by $\pi/(2m)$. A skew dipole, for instance, has an horizontal field. In Eq. (2.5), B_1 is in Tesla, and the dimensionless coefficients b_n and a_n are in so-called units, which are defined as 10^{-4} of the main field.

The multipolar components, describing the perturbations with respect to the ideal dipole field, can be classified in two groups. The odd normal multipoles b_1, b_3, b_5, \dots are called the *allowed multipoles*. They are generated by a current distribution which respects the dipole symmetry, i.e. even with respect to the x axis and odd with respect to the y axis. The even normal multipoles b_2, b_4, b_6, \dots and all the skew multipoles a_1, a_2, a_3, \dots are called the *unallowed multipoles*. They result in violation of the dipole symmetry: the even normal multipoles are due to asymmetries left-right and the skew multipoles to asymmetries top-bottom. In Table 2.3 we give the classification of the low order multipoles.

The allowed multipole can be tuned by changing the limiting angles of the two coil layers or the positions of the copper wedges. On the other hand, the minimization of the unallowed multipoles, which are determined by manufacturing errors, requires great precision in the construction of the magnet components.

Table 2.3: Multipole classification.

Multipole		
b_2	unallowed	left-right asymmetry
a_2	unallowed	top-bottom asymmetry
b_3	allowed	dipole symmetry
a_3	unallowed	top-bottom asymmetry
b_4	unallowed	left-right asymmetry
a_4	unallowed	top-bottom asymmetry
b_5	allowed	dipole symmetry
a_5	unallowed	top-bottom asymmetry
b_6	unallowed	left-right asymmetry
a_6	unallowed	top-bottom asymmetry
b_7	allowed	dipole symmetry
a_7	unallowed	top-bottom asymmetry

2.2.4 The collars

The high currents and field in a typical $\cos \theta$ dipole produce very large Lorentz forces on the conductors. Considering the dipole cross-section, the Lorentz forces have two main components: an azimuthal component, which tends to squeeze the coil towards the mid-plane, and a radial component, which tends to bend the coil outwards, with a maximum displacement at the coil mid-plane.

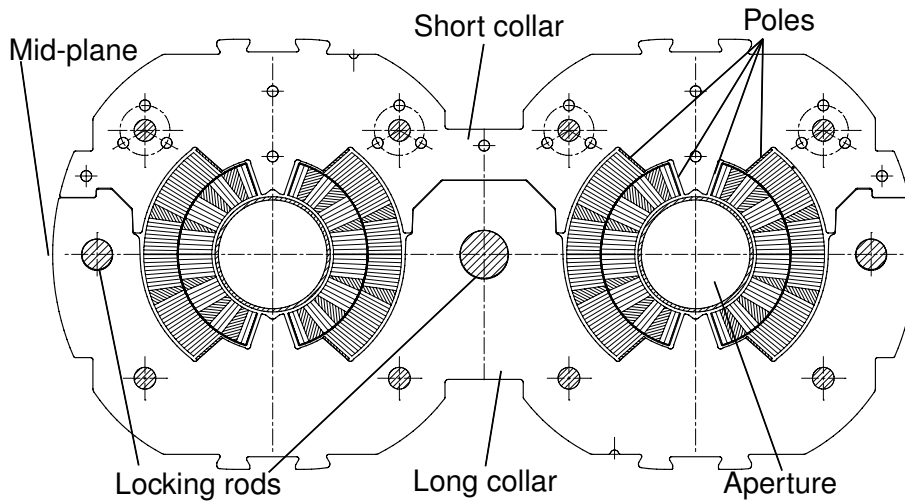


Figure 2.8: The collared coil.

These components may produce minute wire motions inside the coil. If the motions are purely elastic, no heat is dissipated and the coil remains superconducting.

However, if the motions are frictional, the associated heat dissipation may be sufficient to produce a resistive transition (quench). The motions must therefore be prevented as much as possible by providing a rigid support to the coil: the collars (see Fig. 2.8).

The collars confine radially the coil inside a rigid cavity hence counteracting the radial component of the Lorentz forces. Moreover, since the azimuthal component compresses the coil towards the mid-plane, at high field the coil turns close to the poles tend to move away from the collar poles (see Fig. 2.8). To prevent this phenomenon, the collars are assembled in order to produce an azimuthal pre-compression, called *pre-stress*, on the coils. The rule followed during assembly is to apply an azimuthal pre-stress to the collared coil so that the coil is still compressed by the pole at full magnet current. Therefore, the coil pre-stress applied at room temperature by the collar must be sufficient to compensate for:

- insulation creep following the collaring procedure;
- differential thermal shrinkage between collars and coil during cool-down;
- stress redistribution due to the azimuthal component of the Lorentz forces at high current.

In the LHC dipole it has been chosen an azimuthal pre-stress at ambient temperature after collaring of 75 ± 15 MPa, which falls down to about 30 ± 7 MPa after the cool-down. The collars are made of 3 mm thick high-strength stainless steel sheet. They are closed around the two coils by means of three locking rods (see Fig. 2.8). Collars sheets are superposed one to the other to create packs, assembled using little pins. Each layer is composed of two different parts, the so-called ‘long-collar’ and the ‘short-collar’. The long-collar contains the holes where to put the locking rods. The short one has indeed a pure filling function. Different layers of collars are assembled putting alternatively the long collars on the upper part and on the lower part of the magnet.

Collaring shims, made of fiberglass, are located at the poles between the coil and the collar (see Fig. 2.9). They represent an effective way of changing the pre-stress and the azimuthal coil length, acting in turn on the multipolar contents of the magnetic field.

In fact, by modifying the pole shim size, it is possible to change the space available for the coil inside the collar cavity, thus varying the azimuthal pre-stress exerted by the collar on the coil. This means that the pole shims allow to compensate the possible difference of coil dimension during production with respect to the nominal design obtaining at the end of the collaring the nominal pre-stress. Moreover they can be used also for fine tuning the field quality during the magnet production. In fact, if the pre-stress is varied, also the total azimuthal coil length, and consequently the field quality, is modified.

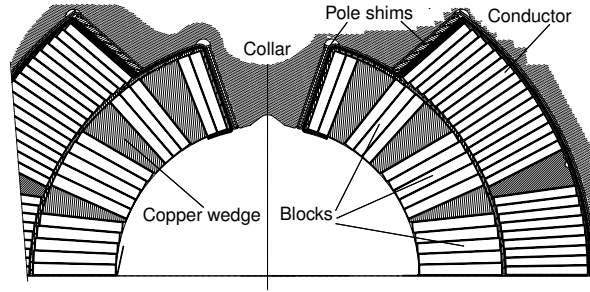


Figure 2.9: The pole shims.

2.2.5 The yoke and the shrinking cylinder

The ferromagnetic yoke (see Fig. 2.10) contributes to increase the magnetic field inside the aperture of about the 20 % and confines the field flux, so that very low field exits from the cold mass. Moreover, it represents an extra support for the collared coil against the radial component of the Lorentz forces. The yoke consists of two halves of low carbon steel laminations 5.8 mm thick. To ensure that the collars are in contact with the yoke at 1.9 K after the cool-down, the two halves are designed with a vertical gap of about a tenth of mm, which corresponds to the differential thermal shrinkage between the collars and the yoke. The yoke laminations are contained by

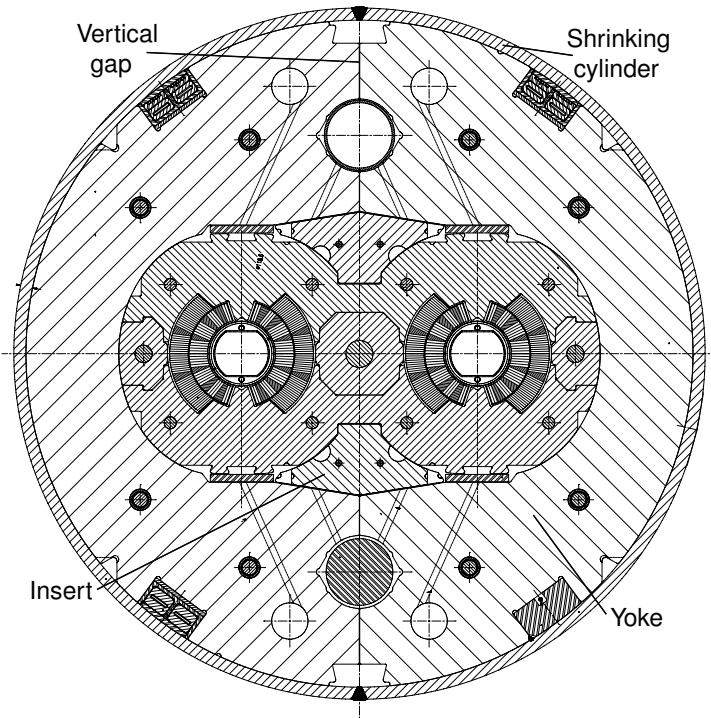


Figure 2.10: The cold mass cross-section.

the shrinking cylinder, which is composed of two half shells about 15 m long. The two half shells are welded with interference around the iron yoke. The interference generates a tensile stress of about 150 MPa in the cylinder. The force exerted by the shrinking cylinder on the two yoke halves closes the gap at ambient temperature and it is transmitted to the collar horizontally on the mid-plane and vertically via the ferromagnetic insert (see Fig. 2.10). The collared coil is slightly deformed by the force exerted by the yoke and the cylinder, and a small increase of the coil azimuthal pre-stress (about 6 MPa) occurs.

After the cool-down, the deformation of the collared coil induced by the yoke disappears because of the differential thermal contraction between collars and yoke, leaving only a contact on the mid-plane which ensures a radial support to the collared coil during the excitation to the nominal field.

With respect to the single aperture design, the two-in-one geometry features a magnetic cross-talk between the two apertures [8]. In fact, the system consisting of two identical dipole coils, charged in opposite direction and with surrounding yoke, does not exhibit full symmetry with respect the vertical axes. Hence even normal field harmonics occur. Nevertheless, they can be optimized by the ferromagnetic insert, which has a significant influence on the low order even harmonics.

2.2.6 The cold mass and the cryostat

The dipole cold mass is roughly 27.5 t weight and about 15 m long. It is placed on three support posts each consisting of a low thermal conductivity composite tubular column. Inserted inside the vacuum vessel it forms the so-called dipole cryomagnet or cryo-dipole (see Fig. 2.2). The dipole cryostat runs at three temperature levels, 1.9 K for the cold mass, and at 4.5 - 20 K and 55 - 75 K for the two intermediate heat intercept levels. The two thermal shields are installed to minimize heat inleaks to the cold mass at 1.9 K. The radiation screen uses multilayer superinsulation enclosing the cold mass. The outer thermal shield, which intercepts the largest fraction of incoming heat at 55 - 75 K, consists of a self-supporting aluminum screen covered with multilayer superinsulation. A helium-gas-cooled aluminum pipe forms part of the screen, which is divided into several segments to decrease movements during cool-down and warm-up. The vacuum vessel contains insulation vacuum at a pressure below 10^{-6} mbar and it is made of steel. It is itself supported at three points, coincident with the support posts. Three alignment targets are mounted on the vacuum vessel to allow fine positioning in the tunnel. One target is at the longitudinal location of the first support, the other two at the third support. These outside references to the cold mass are established mechanically and verified on the magnet measurement bench with respect to the magnetic axis. A retractable sliding sleeve with flexible bellow elements encloses the interconnect region between two cryomagnets, ensuring the continuity of the insulation vacuum; the radiative insulation and thermal shield are also continued across the interconnection region.

2.2.7 The composite support posts

The cold mass supporting system inside the cryostat represents a major issue to meet the alignment requirements of the LHC machine lattice. The aligning procedure is in fact performed on the cryostat so that the stability of the cold mass position with respect to the cryostat must be guaranteed for an average lifetime of 20 years. In order to minimize the vertical sagitta of the cold mass and the heat transfer between the cold mass at 1.9 K and the cryostat at 300 K the supporting system design is characterized by three composite fiber cylindrical supports: a central and two laterals at 2 meters from the cold mass ends. During the 20 years operating life in a cryogenic environment, each support is subjected to a vertical load of around 90 kN, plus parasitic loads due to stick-slip effects on the sliding interface, to the 1.4 % inclination of the tunnel and to the mechanical and electrical interconnections between magnets. The material, chosen for the small thermal conductivity/stiffness ratio, is the composite ‘G-10’, made of graphite fiber reinforced with epoxy (GFRE). In Table 2.4 we compare different structural support materials in terms of conductivity/allowable stress ratio k/σ .

Table 2.4: Figure of merit for structural support materials.

k/σ [WmK/Pa] 10^{-8}			
material	4 K	80 K	300 K
304 ss	0.042	1.8	3.7
6061 T6 Al	2.8	36	57
G-10	0.008	0.057	0.19
brass	1.3	21	46
copper	345	566	523

Each support, as shown in Fig. 2.11, is composed of a main thin-walled column 4 mm thick with a stainless steel reinforcing collar at the top. The collar is bolted to a stainless steel pad welded on the cold mass whereas the column base interfaces a simple support on the cryostat to allow sliding due to the cold mass thermal contraction. A key on each interface guides the sliding direction: longitudinal for the lateral supports and transversal, to allow homothetic shrinkage, for the central one. To reduce the heat conduction to the cold mass, two intermediate heat extractors at 7.5 K and at 57.5 K are installed along the composite column. The heat intercepts are 10 mm-thick aluminum plates externally glued to the column and connected to the cryogenic line. They also have the function of support for the thermal shield and radiation screen structures inside the cryostat allowing their different thermal contractions with respect to the cold mass.

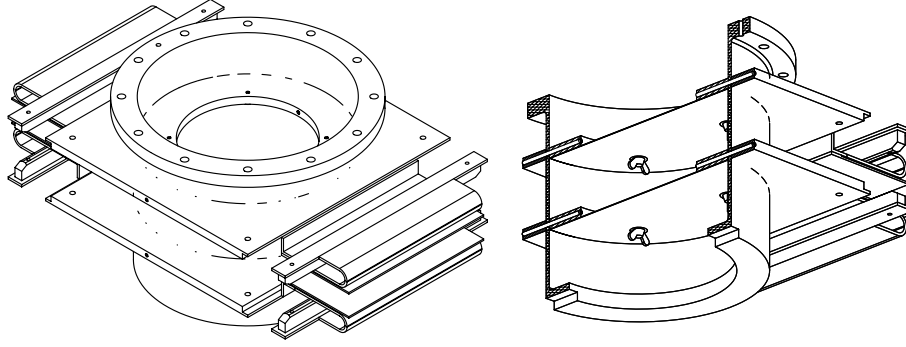


Figure 2.11: The composite supporting post for the dipole cold mass.

2.2.8 Magnet extremities

In the coil ends the the block of cables follow a 3D curve to form a U shape in both the horizontal and the transversal plane. In the horizontal plane it is needed to close the coil track and in the transversal plane it is needed to leave the space for the beam tube as shown in Fig. 2.5. The coil shape in the ends provides thus an unwanted 3D magnetic field that is decreased by mean of non-electromagnetic material replacing the iron yoke. The resultant electromagnetic forces acting on the coil in the longitudinal direction are partly transmitted to the collars, the yoke and the shrinking cylinder by friction and the remaining part is directly transmitted to the thick end plates (Fig. 2.1). Other than to enclose the superconducting coil and the packed laminations, the end plates are designed to host the small multipolar magnets (sextupoles and octupoles/decapoles) needed to compensate the dipolar field imperfections. The relative position between multipolar correctors and the end plate is precisely set via the adjustable support shown in Fig. 2.15 to meet the alignment requirements before the end cover sealing.

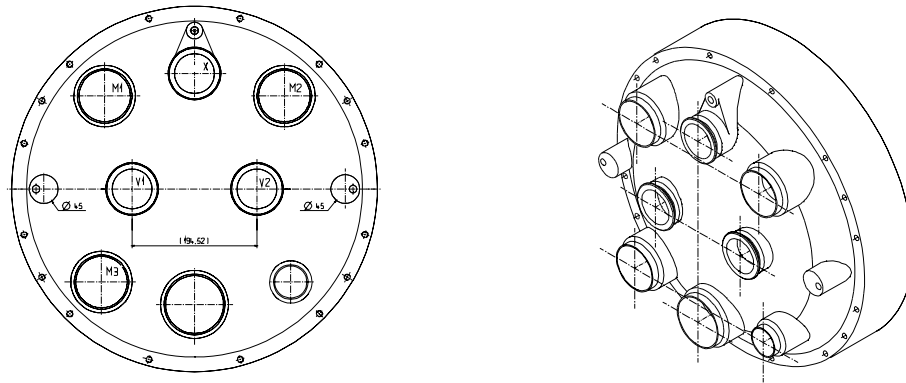


Figure 2.12: The cold mass end cover.

The end covers close the extremities of the cold mass (Fig 2.12), they are welded to the shrinking cylinder to complete the Helium vessel. They nevertheless must

leave passages for the beam tubes, a heat exchanger tube and two pipes containing the main and the auxiliary electrical connections. The cover on the connection side of the magnet leaves also a passage for a pipe leading to a pressure relief valve located in the junction space between the magnet units.

The 1700 interconnections between magnets represent thus a crucial part of the LHC lattice since they must ensure the continuity of the vacuum enclosures, the beam pipe image current, the cryogenic circuits, the electrical power supply and the thermal insulation. The bellows interconnecting each one of these lines must also compensate for the thermal expansion/contraction of the magnets (around 46 mm) and for their potential transverse misalignment.

2.3 Cold mass geometry

In order to maximize the mechanical clearance for the circulating beam with the minimum coil size the cold mass is bent in the horizontal plane to follow the theoretical beam orbit. To guide the particles over a circular trajectory, each one of the 1232 magnet must provide a curvature of:

$$\frac{2\pi}{1232} = 5.099988 \cdot 10^{-3}, \quad (2.8)$$

radians, corresponding to a magnetic length of the dipolar field of 14343 mm. This is therefore the central part of the magnet containing the coil that is bent to closely follow the beam orbit. The remaining parts consist of two 408.5 mm-long straight prolongations containing the short multi-polar magnets needed to focus the beam. The theoretical axis shapes in the horizontal plane are given in Fig. 2.13; in the vertical plane the axis are straight lines belonging to the LHC ring plane (Fig. 2.14). Since the geometry of the whole magnet reflects the bore tube axis shapes, the manufacturing tolerances are given with respect to the tube axes. The geometric requirements are driven by magnetic considerations i.e. to ensure mechanical clearance and corrector magnet precise positions for the beam optic and mechanical i.e. to ensure the integrity of the interconnections between magnets. The tolerance values for the main components are given in detail below.

2.3.1 Tolerance on the shape

As the tube axis should be within ± 1 mm around the theoretical beam path, the tolerance range is shaped as an arc of torus with a major radius of 2812360 mm and a minor radius of 1 mm in the bent part whereas as cylinder of 0.3 mm radius in the straight parts [9]. The theoretical geometry of both the tubes, projected on the horizontal plane, is shown in Fig. 2.13. The ideal axis projection on a vertical plane is a straight line; the flexion due to cold mass self weight is expected to be 0.3 mm as shown in Fig. 2.14. The overall magnet length must be 15158 ± 2.2 mm.

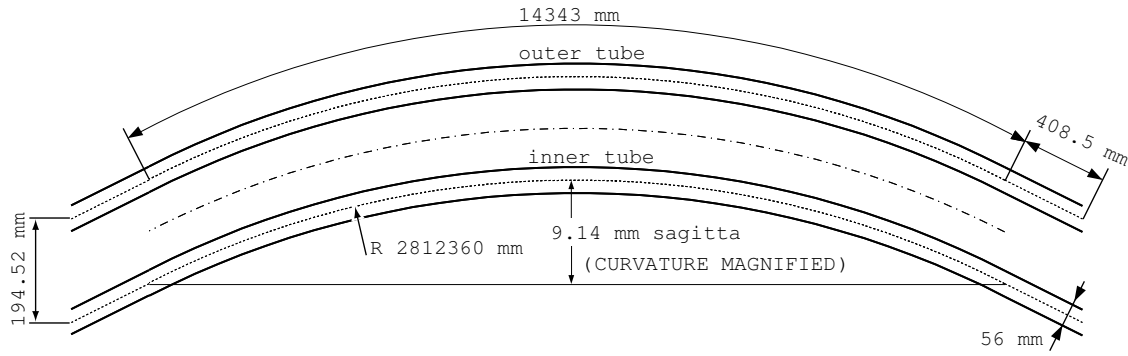


Figure 2.13: The tube axes shape in the horizontal plane.

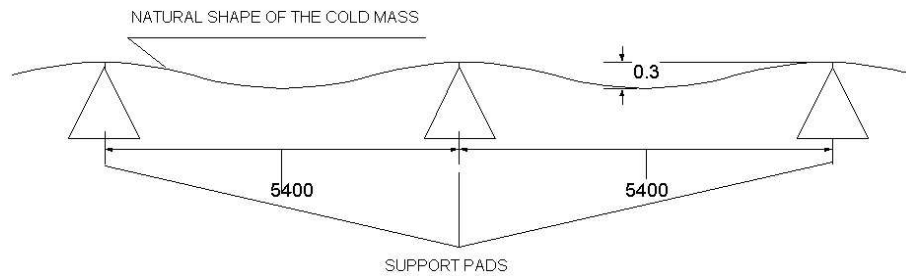


Figure 2.14: The tube axis shape in the vertical plane.

2.3.2 Tolerance on the interconnecting components

The interconnections between magnets can withstand transverse displacements up to 6 mm [10] but the radial tolerance is set at 0.6 mm for the cold bore tube extremity positions and at 0.75 mm for the end cover positions whereas the tilt must not exceed respectively 5 mrad and 1 mrad. These values were chosen by taking into account the further misalignments potentially introduced by the successive assembly steps and the fatigue life of the interconnections since, during the LHC operating life, they will be subject to cyclic loads.

Other important interconnecting components are the feet pads welded on the cold mass to allow the interfacing with the composite support posts. Their position is related to the vertical sagitta of the cold mass and consequently to the respect of the shape tolerance in the vertical plane. Of the three feet pads, the central one should be positioned at the cold mass mid-length and the laterals at 5.4 m from it within ± 1 mm. The three pads interfacing surface must be 294 ± 0.5 mm from the theoretical horizontal plane containing the tube axes.

2.3.3 Tolerance on the multi-polar correctors

To correct the unavoidable harmonic components of the main field, due to manufacturing tolerance, persistent currents and iron saturation, multi polar correctors

Component	Value		Units
Tube axis	1		[mm]
Overall length	± 2.2		[mm]
End cover pos.	± 0.75		[mm]
End cover tilt	± 1		[mrad]
End flange pos.	± 0.6		[mm]
End flange tilt	± 5		[mrad]
Support pads	± 1		[mm]
Correctors	± 0.3 (avg)	0.5 (std)	[mm]

are placed in each magnet extremities. The position of the sextupole and combined decapole octupole magnets must be centered on the beam trajectory with an high accuracy in order to prevent the so-called multipole feed-down effect [11]. The radial misalignment between the magnetic center of the multipolar fields and the beam orbit cannot exceed a systematic value of ± 0.3 mm with a dispersion of 0.5 mm at 1σ .

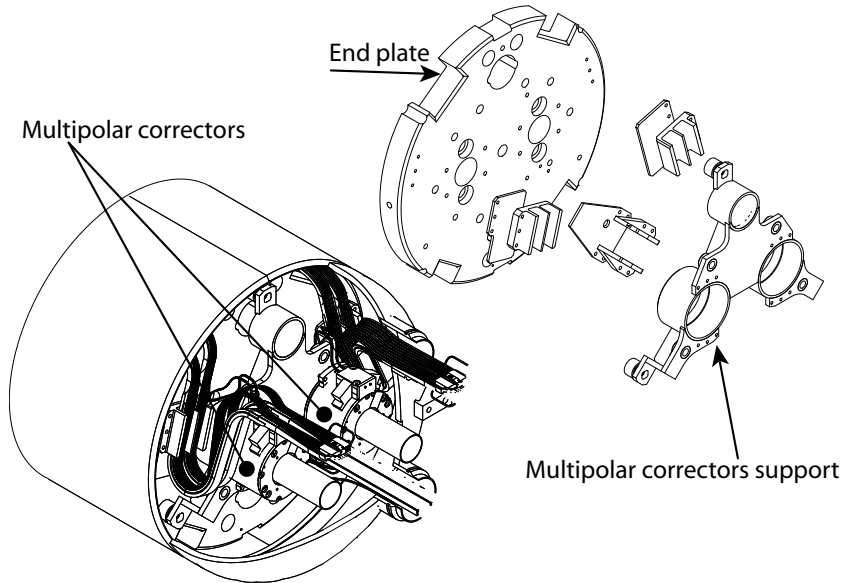


Figure 2.15: The multipolar correctors and the adjustable support.

Chapter 3

The superconducting dipole models

3.1 Introduction

To evaluate the final performance of such a complex and innovative machine as the LHC will be, it is mandatory to use predictive models in order to simulate all the different aspects involved in the project. A wide range of softwares have been thus developed to simulate events from the installation procedures to the interactions between bunches of million particles spinning along the 27 km ring.

A mechanical model of the dipole is needed to accomplish several tasks as: to check the structural qualities of the assembly, to identify situations potentially dangerous for the magnet integrity and to predict permanent or temporary shape modification induced by external forces or by internal thermodynamic or electromagnetic phenomena.

3.2 The analytical model

In spite of the accuracy, that strongly depends on the necessary simplifications, an analytical model is a fast and solid tool that can provide a foretaste of the phenomena's nature and that can be used for on-line analyses and optimization algorithms as well as a base to develop more complex models based, for example, on finite element method.

As first approximation the dipole cold mass can be studied as a slim and homogeneous elastic beam. In fact, the 15 m-long, 0.5 m-diameter cylindrical shape suggests us considering the pure bending as the cause of axis deflections and the limited cross-talk between deformations in the vertical and horizontal planes allows us to implement a 2D model for each plane. Furthermore we do not take into account the slight horizontal curvature of the cold mass so that our model is a straight beam. To describe the structural behavior of the heterogeneous and discontinuous

cold mass internal structure we can use an homogeneous material characterized by equivalent mechanical properties. In the field of small deformations we can also approximate the stress-strain curve with a straight line typical of elastic materials. Under these assumptions the deflections of the cold mass in the vertical and in the horizontal plane can be derived accordingly to the pure bending theory for an homogeneous and continuous slim beam.

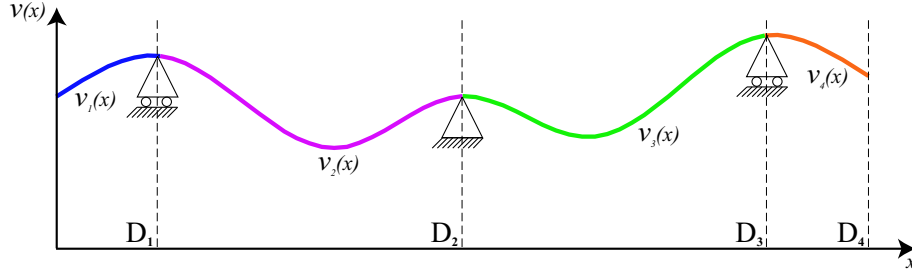


Figure 3.1: The 2D slim beam model. See Appendix A for details.

As the cold mass is supported in three points we can consider it as a system four beams rigidly connected to each other as shown in Fig. 3.1. We can apply concentrated and/or distributed loads to each beam and, thanks to the linearity of the system, granted by the hypothesis of small displacements and deformations, the final deformation of each beam will be the sum of the deformations induced by the different loads. The deformation of the complete system is then obtained by imposing the equilibrium to rotation in the three interface sections between the beams, as done for the first time by Emile Clapeyron in 1857 ('three moments equation'). In this way the analytical expression of the system is represented by a matrix of polynomial coefficients that can be easily solved directly (i.e. apply loads and constraints to obtain deformations) or inversely (i.e. impose deformations and obtain applied loads and constraints). Matrix coefficients, given explicitly in Appendix A along with a more detailed description of the model, are function of boundary conditions (loads and constraints) and mechanical properties:

- cold mass density
- cold mass flexural rigidity (EI)
- distance between supports
- vertical offset between supports
- forces applied at the extremities
- distributed forces
- moments applied at the extremities

- moments applied at the support locations

Once that we have the deflection function $v_i(x)$ for the i^{th} beam in the form:

$$v_i(x) = a_i x^4 + b_i x^3 + c_i x^2 + d_i x + e_i \quad (3.1)$$

valid for x in the domain of the i^{th} beam: \mathbf{D}_i , the matrix notation allows us to write:

$$v_i(x) = \begin{bmatrix} a_i & b_i & c_i & d_i & e_i \end{bmatrix} \begin{bmatrix} x^4 \\ x^3 \\ x^2 \\ x^1 \\ x^0 \end{bmatrix} \quad (3.2)$$

that can be rewritten as:

$$v_i(x) = [M_i] \{x\}, x \in \mathbf{D}_i \quad (3.3)$$

The deflection function for the complete system of four beams is then:

$$v(x) = \begin{cases} [M_1] \{x\} & , x \in \mathbf{D}_1 \\ [M_2] \{x\} & , x \in \mathbf{D}_2 \\ [M_3] \{x\} & , x \in \mathbf{D}_3 \\ [M_4] \{x\} & , x \in \mathbf{D}_4 \end{cases} \quad (3.4)$$

As soon as we consider the domain \mathbf{D}_i composed of a finite number of points n_i along the i^{th} beam length, the general coordinate $x \in \mathbf{D}_i$ becomes a $1 \times n_i$ row array \mathbf{x}_i and the former 5×1 column array $\{x\}, x \in \mathbf{D}_i$ becomes a $5 \times n_i$ matrix: X_i . In this way we can rewrite Eq. 3.4 as:

$$\mathbf{v}(\bar{\mathbf{x}}) = \begin{bmatrix} M_1 & M_2 & M_3 & M_4 \end{bmatrix} \begin{bmatrix} X_1 & \bar{0}_2 & \bar{0}_3 & \bar{0}_4 \\ \bar{0}_1 & X_2 & \bar{0}_3 & \bar{0}_4 \\ \bar{0}_1 & \bar{0}_2 & X_3 & \bar{0}_4 \\ \bar{0}_1 & \bar{0}_2 & \bar{0}_3 & X_4 \end{bmatrix} \quad (3.5)$$

where: $\bar{\mathbf{x}} = \begin{bmatrix} \mathbf{x}_1 & \mathbf{x}_2 & \mathbf{x}_3 & \mathbf{x}_4 \end{bmatrix}$, $\bar{0}_i$ are $5 \times n_i$ null matrices and \mathbf{v} represents the cold mass deflection evaluated in a finite number of points $\bar{\mathbf{x}}$. The main advantage of the analytical model is that it can be evaluated in the form of Eq. 3.5 and thus easily implemented in numerical simulations and optimization algorithms.

We present now a typical application of the analytical model in the form of Eq. 3.5, that is: the evaluation of one or more parameters among the boundary conditions and mechanical properties listed in the beginning of this paragraph. For example the evaluation of the flexural rigidity and support positions of a cold mass

whose deflection in the vertical plane, induced by gravity and measured in n points, is the curve $(\bar{\mathbf{x}}, \bar{\mathbf{z}})$. This is accomplished through the least square fit of the model on the measured data with EI and the longitudinal and vertical support positions as free parameters. The searched values are the ones that minimizes the sum of the square offsets between model and data, ε :

$$\varepsilon = \sum_{k=1}^n [z_k - v(x_k)]^2 \quad (3.6)$$

Using matrix notation it can be written as:

$$\varepsilon = [\bar{\mathbf{z}} - \mathbf{v}(\bar{\mathbf{x}})][\bar{\mathbf{z}} - \mathbf{v}(\bar{\mathbf{x}})]^T \quad (3.7)$$

If now we decompose the measured data accordingly to the four longitudinal domains \mathbf{D} :

$$\bar{\mathbf{x}} = \begin{bmatrix} \mathbf{x}_1 & \mathbf{x}_2 & \mathbf{x}_3 & \mathbf{x}_4 \end{bmatrix}, \bar{\mathbf{z}} = \begin{bmatrix} \mathbf{z}_1 & \mathbf{z}_2 & \mathbf{z}_3 & \mathbf{z}_4 \end{bmatrix} \quad (3.8)$$

and we call:

$$[M_i^*] = \begin{bmatrix} 1 & -M_i \end{bmatrix}, X_i^* = \begin{bmatrix} \mathbf{z}_i \\ X_i \end{bmatrix} \quad (3.9)$$

Eq. 3.7 becomes:

$$\varepsilon = \begin{bmatrix} M_1^* & M_2^* & M_3^* & M_4^* \end{bmatrix} \begin{bmatrix} X_1^* & \bar{0}_2 & \bar{0}_3 & \bar{0}_4 \\ \bar{0}_1 & X_2^* & \bar{0}_3 & \bar{0}_4 \\ \bar{0}_1 & \bar{0}_2 & X_3^* & \bar{0}_4 \\ \bar{0}_1 & \bar{0}_2 & \bar{0}_3 & X_4^* \end{bmatrix} \begin{bmatrix} X_1^* & \bar{0}_2 & \bar{0}_3 & \bar{0}_4 \\ \bar{0}_1 & X_2^* & \bar{0}_3 & \bar{0}_4 \\ \bar{0}_1 & \bar{0}_2 & X_3^* & \bar{0}_4 \\ \bar{0}_1 & \bar{0}_2 & \bar{0}_3 & X_4^* \end{bmatrix}^T \begin{bmatrix} M_1^* \\ M_2^* \\ M_3^* \\ M_4^* \end{bmatrix} \quad (3.10)$$

where, this time, $\bar{0}_i$ are $6 \times n_i$ null matrices.

Eq. 3.10 represents the function to minimize in order to find the searched support positions and flexural rigidity values and, also in this case, the matrix form is very convenient to implement the minimum search algorithm.

This procedure can be used to find all the parameters listed at the beginning of the chapter; the only two necessary conditions are: the number of parameters searched be less than the number of measured points and the parameters be independent to each other.

3.3 The 3D finite element model

The main limits of the analytical model are the planarity, the straightness and the absence of the three composite feet which support the dipole inside the cryostat. The need to model the supports comes from the fact that they represent the only connection to the cryostat and that their rigidity is far smaller compared to cold

mass and to cryostat. Furthermore, to allow the magnet thermal contractions, the supports are allowed to slide on the cryostat with a non-negligible friction that makes the system strongly non-linear.

The finite element model (shown in Fig. 3.2) has been implemented using the commercial software ANSYSTM. The model is composed by the components that contribute to the structural behavior:

- the collar
- the yoke
- the shrinking cylinder
- the end cover
- the composite support posts
- the support pads
- the cryostat
- the transport restraints

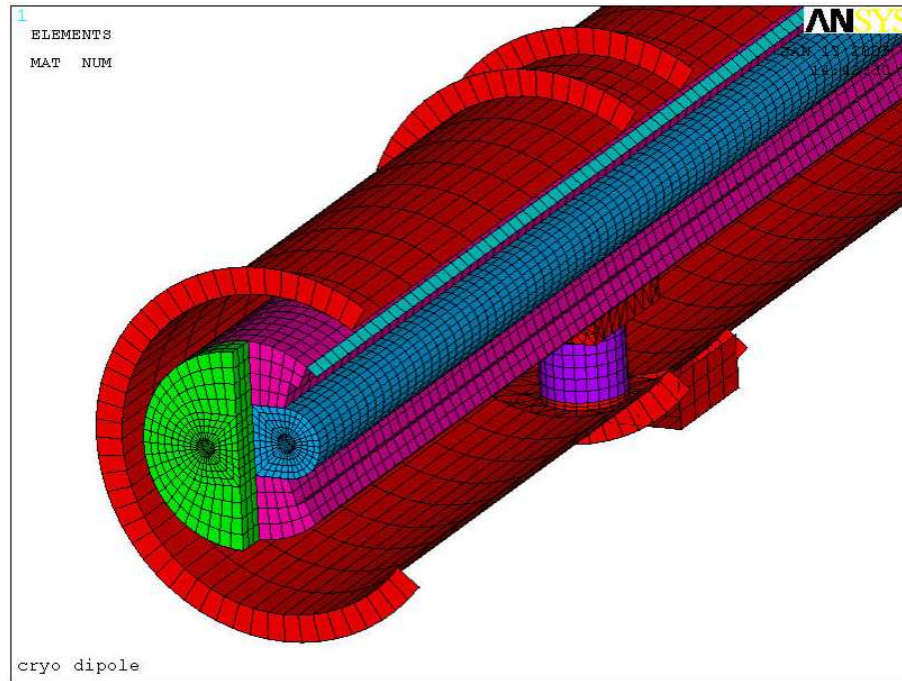


Figure 3.2: A cut of the cryo-dipole finite element model.

The main simplifications in the model concern the inner part, made of packed laminations of steel for the collar and iron for the yoke. The collar and the yoke, in

fact, although modeled with individual material properties are implemented using element BRICK45 [12] without any longitudinal or radial discontinuity. To take into account the effect of the yoke and collar longitudinal discontinuity on the dipole mechanical behavior, we computed an equivalent longitudinal Young's modulus to meet the experimental flexural rigidity of $180 \text{ MPa}\cdot\text{m}^4$ [13] and an equivalent tangential stiffness to meet the experimental rigidity to torsion of around $0.4 \text{ GPa}\cdot\text{m}^4$ [14]. To disentangle radial stresses and longitudinal deformation we assigned a very small value to the related Poisson's ratios.

The shrinking cylinder is modeled using SHELL63 [12]. All material properties are isotropic except for the fictitious thermal contraction used to simulate the azimuthal pre-stress as explained in Appendix C.

The support posts are thin-walled column implemented through element SHELL63. In modeling the material we considered different values of Young's modulus in the range from 15 to 22 GPa, following production changes. To take into account the anisotropy due to the glass fiber orientations, we assumed a 3.2 GPa tangential elasticity with a Poisson's ratio of 0.3 to meet the experimental rigidity to guided and cantilever bending [15]. In the connection between SHELL and BRICK elements at the top and at the bottom of the supports, the rotational degree of freedom of the SHELL is not transmitted to the BRICK. The equilibrium to rotation is nevertheless guaranteed by the moment generated by the normal forces on the top and bottom edges of the cylinder.

The support pads connect the support posts to the shrinking cylinder. Modeled through BRICK45 they have fully isotropic materials properties. The pad volume is entirely meshed through pyramidal shaped elements to allow interfacing the mapped surface of the shrinking cylinder to the circular top edge of the support post (visible in Fig. 3.3).

The end covers were roughly modeled to allow the implementation of the transport restraints connecting the cold mass to the cryostat. They come as a thick circular cap of BRICK45 whose material has an equivalent density to match the end cover real weight.

The cryostat has been modeled without relevant simplifications using element SHELL63 and a fully isotropic material.

In the cryo-dipole model slice represented in Fig. 3.3 one can see the cryostat, the GFRE composite support with the support pad on the top, the yoke and the collar; the shrinking cylinder cannot be distinguished because of a visualization issue.

To check mesh density correctness we parametrized the element sizes. In the yoke, the collar, the shrinking cylinder, the end covers and the cryostat both the radial and longitudinal sizes can be varied independently. In the support posts, the vertical and circumferential sizes can be also varied independently from the rest of the model. We chose two possible sizes, one roughly twice bigger than the other, in linear dimensions (Fig. 3.2 shows the finest mesh). As the solution, in terms of nodal displacements, is independent from the chosen size we use the coarser model

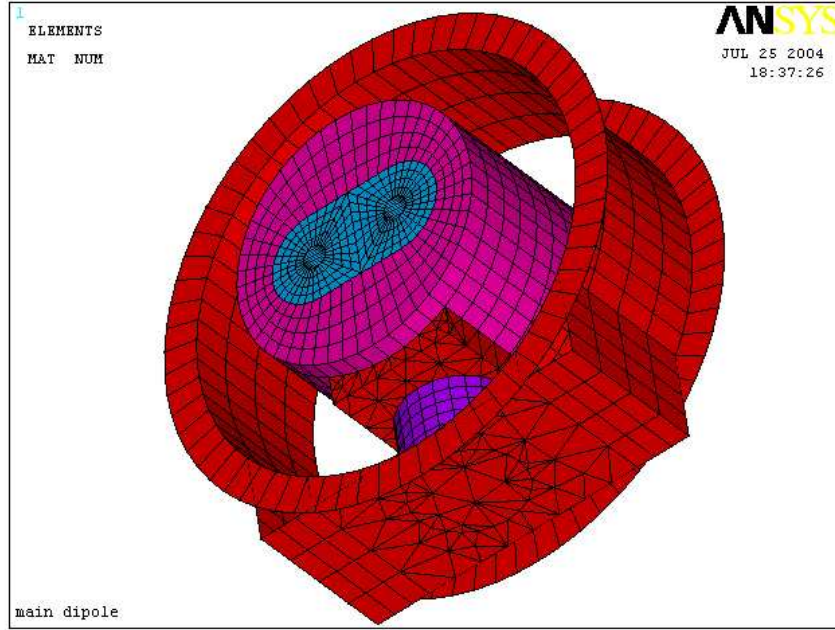


Figure 3.3: A slice of the cryo-dipole finite element model.

Table 3.1: Degrees of freedom (DOF's) and wave front maximum size for different mesh densities.

Mesh	DOF	Wavefront
Fine	$6 \cdot 10^6$	16000
Coarse	$1.2 \cdot 10^6$	7000

in all the analysis concerning the cold mass, support posts or cryostat deformations. When we need to estimate the stresses we increase the mesh density only in the region of interest. Transport restraints are modeled with a fixed size mesh density, particularly fine in proximity of the many holes where the stress concentration is higher (Chapter 6.3.2).

In Table 3.1 we report the number of degrees of freedom and the wavefront size for the coarsest and the finest possible mesh of the cryo-dipole model without end restraints.

The principal model features and material properties are listed in Tables 3.2. Orthotropic properties refer to the cold mass referential whose X and Y axes lie in the plane containing the LHC ring, the X-axis radially directed toward the center of curvature, the Y-axis tangentially directed from Connection end to Non-Connection end and the Z-axis accordingly to the cartesian convention.

It must be pointed out that the properties listed in Table 3.2 are a mix of real

Table 3.2: Young’s modulus, Poisson’s ratio and tangential elasticity of materials implemented in the cryo-dipole finite element model.

Component	Young’s [Pa]			Poisson’s		
	E_x	E_y	E_z	ν_{xy}	ν_{yz}	ν_{zx}
Sh. cylinder		$2 \cdot 10^{11}$			0.3	
Collar	$2 \cdot 10^9$	$6.93 \cdot 10^{11}$	$2 \cdot 10^{11}$	0.01	0.01	0.3
Yoke	$1.9 \cdot 10^9$	$6.27 \cdot 10^{11}$	$1.9 \cdot 10^{11}$	0.01	0.01	0.3
Supp. posts		$23 \cdot 10^9$			0.25	
Transp. rest.		$1.9 \cdot 10^{11}$			0.3	

Component	Tangential [Pa]		
	G_{xy}	G_{yz}	G_{zx}
Sh. cylinder		$7.69 \cdot 10^{10}$	
Collar	$2.7 \cdot 10^{10}$	$2.7 \cdot 10^{10}$	$7.69 \cdot 10^{10}$
Yoke	$2.7 \cdot 10^{10}$	$2.7 \cdot 10^{10}$	$8.1 \cdot 10^{10}$
Supp. posts		$6.8 \cdot 10^9$	
Transp. rest.		$7.3 \cdot 10^{10}$	

and fictitious properties. Their validity is therefore restricted to some specific areas of interest and their values can change accordingly to the phenomenon to study. For example, to model the 150 MPa azimuthal pre-stress in the shrinking cylinder, we worked out equivalent thermal properties as explained in Appendix C.

3.4 The 2D finite element model

For the computation of the cross section deformations in the operative stages, we used an existing 2D FEM model developed at CERN with the aim to analyze the effect of the assembly procedure, of the thermal contractions and of Lorentz forces on the coil pre-stress. An extensive description of the model is given in [16], [17] and [18], hereby we will simply outline its main features to allow the analysis comprehension.

The nominal cross section of the dipole cold mass is depicted in Fig. 2.10. The computational complexity of such a section is primarily due to two features. The first is the absence of any welding between the different components constituting the section; that leads to the necessity of modeling contact surfaces. The second is the behavior of the blocks of conductors that feature a large mechanical hysteresis, a non linear stress-strain relation and difficulties in defining a thermal contraction factor [19], [20], [21], [22]. All these features have been implemented in the finite element model of the dipole cross section that is suitable for both magnetic and mechanical analysis. The magnet length over diameter ratio of around 30 allows

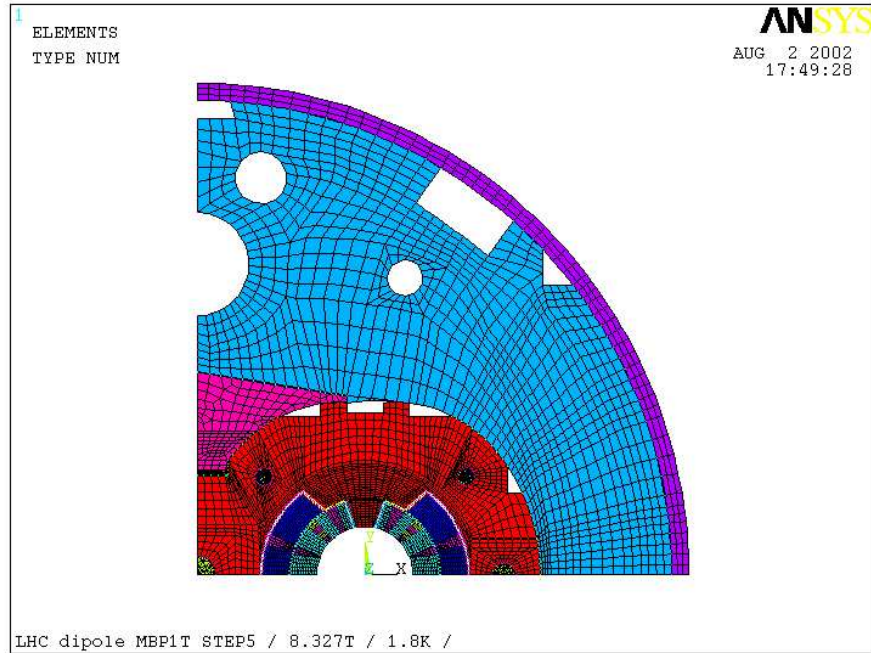


Figure 3.4: The finite element model of the cold mass cross-section.

one to consider a plane stress state and to reduce the analysis to two dimensions. Moreover, thanks to the evident fourfold symmetry of the cross section, only a quarter of that needs modeling (see Fig. 3.4). To analyze coil deformations during the assembly procedure, the finite element model of the dipole has been implemented in ANSYSTM, mainly using element PLANE42 [12]. Magnet cross section has been subdivided into homogeneous regions with specific values of Young's modulus and Poisson's ratio and thermal contraction coefficients. A model in which the two main components, i.e. the copper wedges and the superconducting blocks are well distinct describes the coil. The superconducting blocks are considered homogeneous. Their properties are based on experimental measurements of cables stacks (see [16] for more details).

Contact between surfaces of different components has been described using element CONTACT52 [12]. Internal stresses in the assembled structure are implemented through interferences of these elements.

To estimate the mechanic effect of Lorentz forces on superconducting cables a magneto static model has been firstly adopted. The dipole length allows neglecting the magnetic effect of the ends, consequently only the cross section is considered. Each area of that, including the aperture, has been meshed using the element suitable for electromagnetic analysis: PLANE13 [12]. From the magnetic point of view, different components as the coils, the collar and the aperture are characterized by different values of magnetic permeability. The model input is the current density

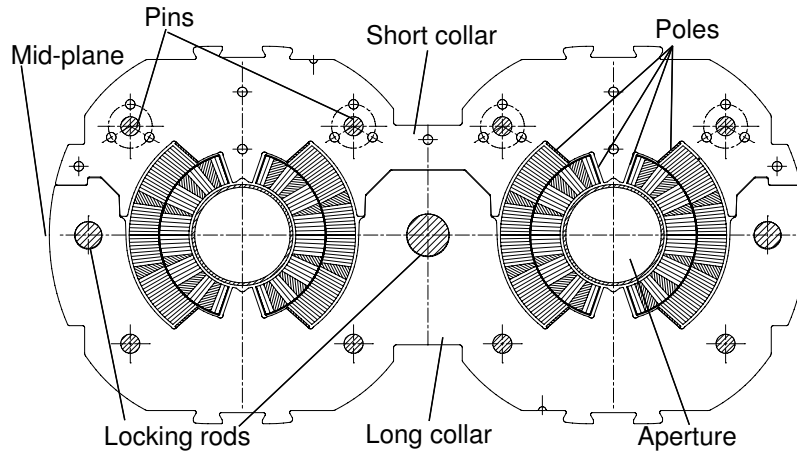


Figure 3.5: Collars and coils cross section. Short and long collars are put alternatively up and down.

in the coils whereas the model result is the electromagnetic force acting on each node of the coils. Then, to get coil deformations, that result is used as mechanical load, along with the thermal shrinking induced by the cool down, for the structural model.

Part II

QUALITY CONTROL OF DIPOLE GEOMETRY

Chapter 4

Phenomenology of dipole shape geometrical susceptibility

4.1 Introduction

The intrinsic challenge of the LHC dipole cold mass production is the respect of the tight geometrical tolerances (few tenths of millimeter over a 15 m-length) needed by beam dynamics. The most critical process is represented by the bending of the magnet cylindrical structure in the horizontal plane. The curved shape imposed by the welding press, must indeed be preserved throughout the rest of assembly, transport and testing circumstances (from now on: pre-operative stages) until the positioning in to the tunnel and the beginning of the operative stages. A wrong curvature, in fact, systematically reduces the mechanical clearance for the circulating particles and provokes a misalignment of the multi-polar correctors hosted in the dipole extremities with detrimental effects on beam stability.

In this chapter we analyze the geometry of 2/3 of the entire production from the early assembly stage to the final storage before the installation in to the tunnel.

We first describe the two geometric parameters that we defined to characterize cold mass shape and the stages at which geometry checks are performed.

We then focus on the curvature obtained in the industry and we follow and discuss the evolution across the successive steps.

We analyze the vertical shape and we show how we removed the spurious effect of slightly different boundary conditions using the analytical model.

In the last part of the chapter we study the unexpected vertical shape of the produced magnet and we propose a possible explanation.

It must be pointed out that since the different studies presented in this chapter have been carried out at different times, the number of cold masses in the different statistical bases can vary considerably.

4.2 Characteristic parameters of cold mass shape

Cold mass shape is measured through a multi-station procedure implemented using laser tracker technology, as described in Chapter 5.2.1. The measured shape is then stored in the geometry database in terms of deviations from the theoretical geometry, given in 2.3 and shown in Fig. 4.1. With respect to Fig. 4.1 we will call ‘horizontal plane’, ‘vertical plane’ and ‘transversal plane’ the (X,Y), (Y,Z) and (X,Z) plane, respectively; ‘horizontal shape’ and ‘vertical shape’ the projections of the 3D axis measurement on the horizontal and on the vertical plane.

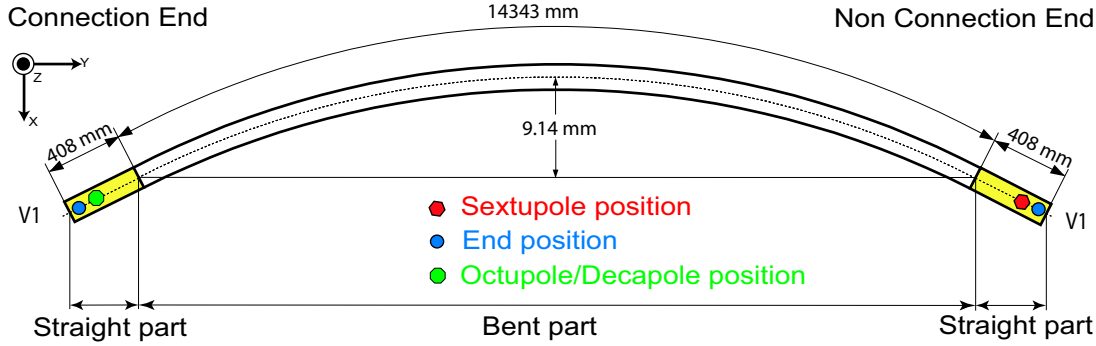


Figure 4.1: Theoretical geometry of the cold bore tube in assembling condition. Horizontal plane (curvature strongly magnified).

To simplify the analysis we defined two parameters that reflect the fundamental geometrical properties of each cold mass, they are:

- the sag in the horizontal plane (from now on: Sag), as an index of horizontal curvature;
- the position of cold mass extremities in the transversal plane (from now on: Ends), as an index of multipolar corrector alignments.

To monitor the shape error evolution across the pre-operative stages, we extract these two parameters from geometric measurements performed at the following steps:

- *After Welding* ('Working Package ITP15'): after the bending and the shrinking cylinder welding;
- *After Manufacturing* ('Working Package ITP20'): before transport to CERN;
- *Arrival at CERN* ('Working Package WP01'): after transport to CERN;
- *After Cryostating* ('Working Package WP03'): after insertion in the cryostat;
- *After Cold Test* ('Working Package WP08'): after magnetic tests and first thermal cycle (300K-1.9K-300K).

4.3 Errors on Sag

Each one of the two apertures hosted in an LHC dipole cold mass, must fulfill the imposed tolerances; although the two apertures are mechanically coupled, we consider them separately. The Sag associated to the ideal curvature is, at room temperature, 9.14mm. Non-nominal curvatures give an error on the Sag that is negative for undersized curvatures and positive for over-sized ones (see Table 4.1, where ρ is the curvature radius).

Table 4.1: Convention for Sag error sign.

$\rho_{\text{measured}} < \rho_{\text{nominal}}$	$\Delta\text{Sag} < 0$
$\rho_{\text{measured}} > \rho_{\text{nominal}}$	$\Delta\text{Sag} > 0$
Tolerance range: $\Delta\text{Sag} = \pm 2 \text{ mm}$	

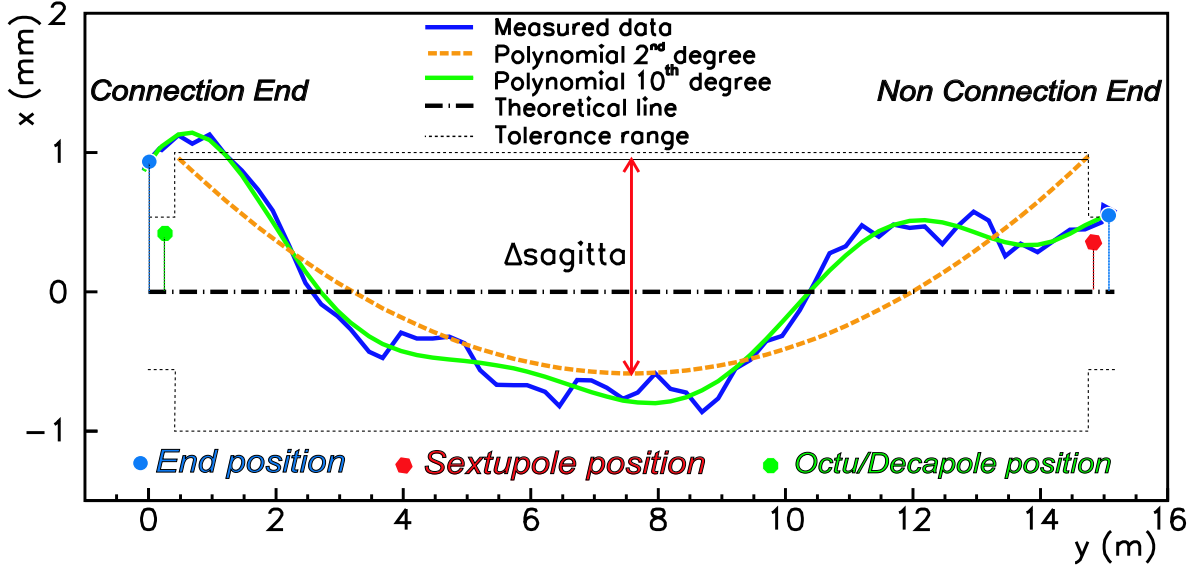


Figure 4.2: Typical measurement outcome. Interpolating polynomials and relevant points for analysis are plotted along with the tolerance range.

The Sag error is obtained from the measured shape projection on the horizontal plane. In Fig. 4.2 we show, as example, the horizontal shape of a cold mass as measured just after the assembly in the industry. The abscissa axis (dashed-dotted line) matches the curvilinear co-ordinate along the nominal shape, the black solid line represents the measured cold mass geometry deviations from the nominal whereas the thin dotted lines envelop the tolerance range: $\pm 1 \text{ mm}$ in the curved part and $\pm 0.6 \text{ mm}$ in the two straight extremities. As we demonstrate in Appendix D, in

this linearized 2D space a cold mass with a over-sized curvature is represented by a parabolic curve with up-ward convexity; down-ward when the curvature is under-sized. Hence the cold mass Sag error corresponds to the sag of the parabolic curve (2^{nd} order polynomial) that fits the horizontal shape errors in the curved part. In Fig. 4.2 the dashed line is the 2^{nd} order polynomial fit of the curved part; it can be seen that the cold mass axis is too curve and the corresponding Sag error ‘ ΔSag ’ is around 1.5 mm.

The solid clear line is the 10^{th} order polynomial fit that we use to minimize the noise associated to the measurement procedure and to pack in an analytic formula the amount of treated data. The polynomial order is the lowest that fits the population within $\pm 0.3\text{ mm}$ [23]. Note that in the acquisition software the distance is always computed in the (X,Z) plane orthogonal to the Y axis (see Fig. 4.1) and thus slightly differs from the 3D euclidean distance.

In Fig. 4.3 we give the Sag error trend along the production per firm. In each graph the solid line is the moving average computed over 30 cold masses and the dashed lines add the corresponding standard deviation at 1σ . The cold mass serial number range over which the average and standard deviation are computed can be read on the X-axis.

Among the three productions we can highlight some similarities as for example the accuracy of the early items (thanks to ‘re-shaping’, a corrective procedure explained later in this chapter) as well as of the last ones. The moving average is quite far from the $\pm 2\text{ mm}$ tolerance during the whole production of all the three firms; the combined effect (dashed lines) of the systematic and of the random component of the error, at 1σ , exceeds the limits only in one case (Firm 3).

We report now some individual features of each production.

Firm 1 (Fig. 4.3, top graph) corrected the systematic negative error (cold mass not curved enough) of the first half of the production with a positive error in the second half, achieving a very small overall average error although surrounded by a spread wider than the other producers. Numerical values are given in Table 4.2.

Firm 2 (Fig. 4.3, middle graph) produced cold mass generally under-curved but with a better reproducibility with respect to the other firms. The latest production is very well centered around the nominal value but the overall result is cold masses in average under curved (Table 4.2).

Firm 3 cold masses feature a curvature that is good in the first and in the last part of the production but generally over-sized in the middle part (Fig. 4.3, bottom graph); hence the final average is still positive as reported in Table 4.2.

The re-shaping procedure was introduced at the beginning of the series production. It was designed to correct the curvature of cold masses severely out of tolerance without disassembling the structure. Three different kinds of behavior can be found among the magnets of the early production. Two of them are typical of those magnets that, being already out of tolerance right after the welding of the shrinking cylinder, have undergone the re-shaping procedure. In these cases the error on Sag,

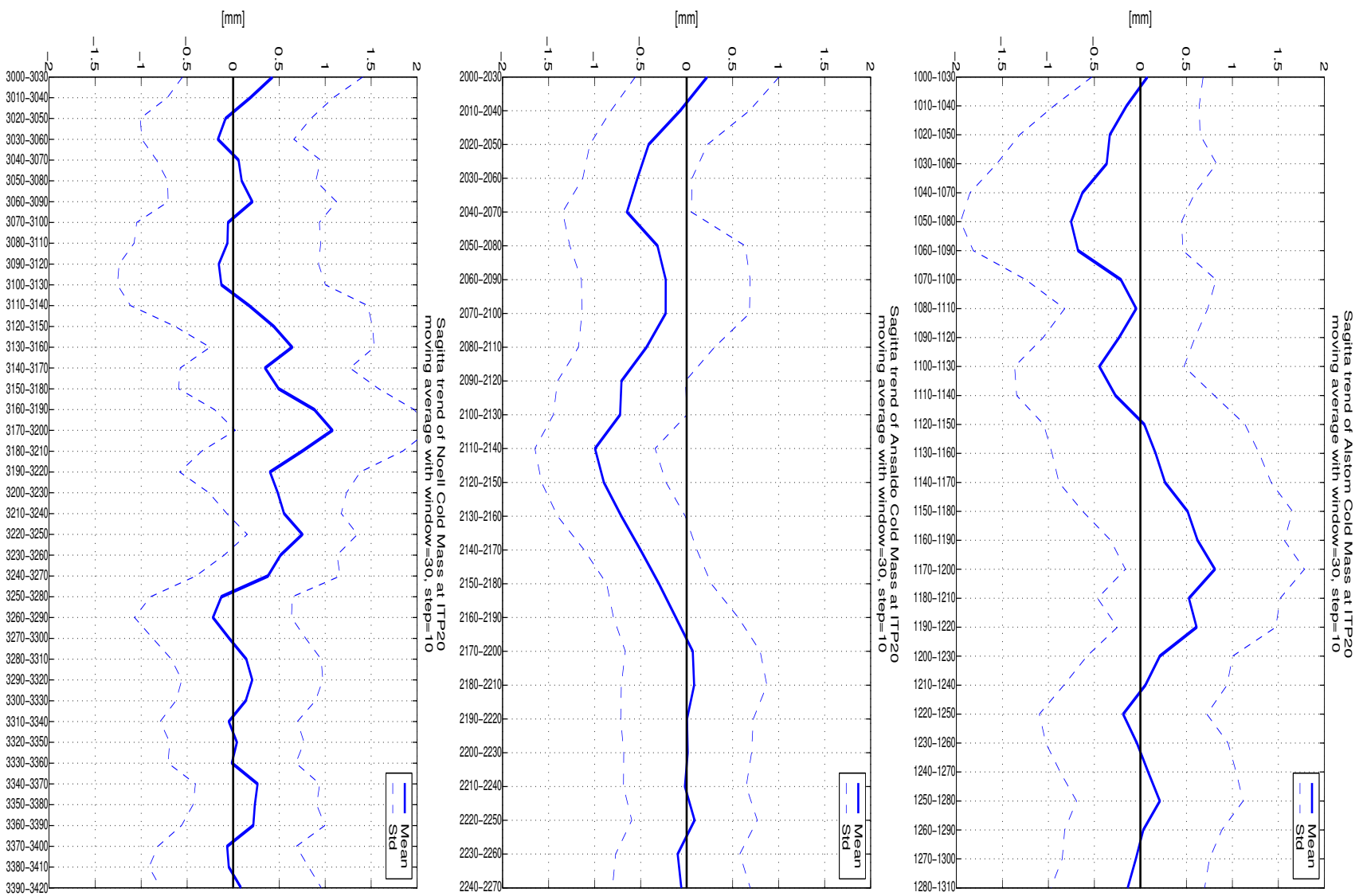


Figure 4.3: Sag error trend along the production of each firm. Average and standard deviation are computed on samples of 30 cold mass per time. X-axis reports cold mass serial numbers.

Table 4.2: Sag errors of cold mass after manufacturing (ITP20 stage)

Firm	Mean [mm]	Std [mm]	# of CM
1	-0.002	1.04	291
2	-0.292	0.79	251
3	0.233	0.93	415

minimized by the re-shaping, tends to increase again toward the ‘After Welding’ value either completely (Fig. 4.4, top) or partially (Fig. 4.4, bottom). This kind of shape degeneration usually does not affect the non-reshaped magnets that feature a less susceptible geometry and represent the third kind of behavior (Fig. 4.4, middle).

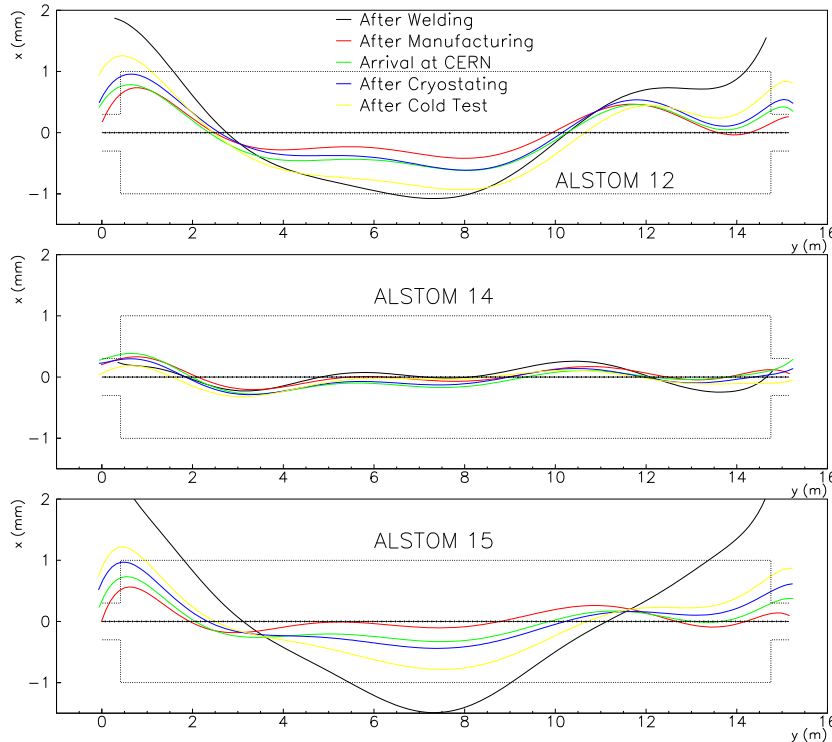


Figure 4.4: The three typical cold mass shape evolutions observed in the early production. The thin dotted lines envelop the early tolerance range (± 0.3 mm in the extremities)

Looking more in detail at the top graph (relative to cold mass 1012) we can see the large negative error on the Sag after the welding procedure (the black solid line) indicating the magnet be too curved with respect to the specifications. This error, conveniently recovered after the re-shaping procedure (red line), comes partially up during transport to CERN (green line), is not affected by the cryostating procedure

(blue line) and regains almost completely the original value after the cold test (yellow line). The progressive degeneration of the shape after the re-shaping procedure clearly affects also the extremities that, because of the tighter tolerances (dotted line), undergo displacements already critical during the transport to CERN. A very similar behavior can be seen in the bottom graph where the evolution of another re-shaped magnet (cold mass 1015) is presented. The only significant difference is the return to the pre-reshaping state that after the cold tests is still partial. As before, the shape degeneration is more critical in the extremities. The third typical behavior, mainly featured by non-reshaped dipoles and visible in the central part of Fig. 4.4 (cold mass 1014), is characterized by very small shape variations that always remain well within the tolerances and, consequently, do not lead to critical circumstances.

We can compare now the systematic Sag change of a sub-sample of reshaped and non-reshaped magnets of the early production which were measured at every pre-operative step: from just after the first bending ('After Welding', ITP15) up to the pre-installation storage ('After Cold Test', WP08). In the right plot of

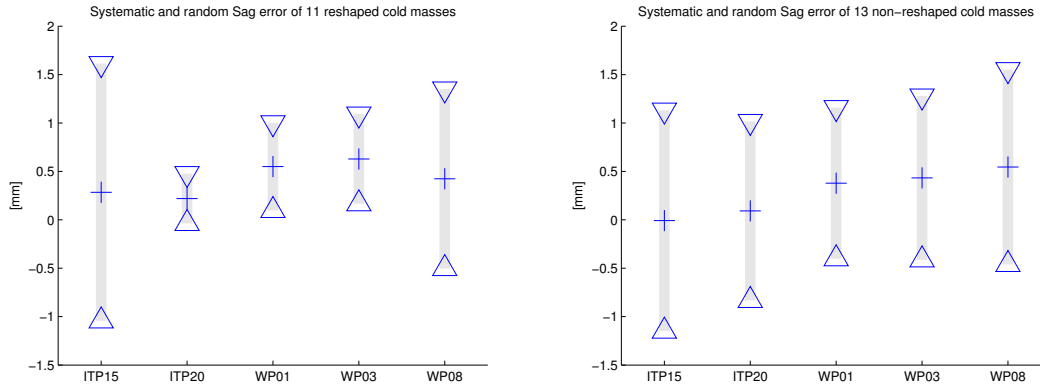


Figure 4.5: Sag change across pre-operative stages for the first 11 reshaped cold masses (left plot) and for the first 13 non-reshaped cold masses (right plot).

Fig. 4.5 we show the evolution of the Sag error for the 11 re-shaped cold masses, the marker represents the mean value and the bands the distribution at 1σ . It can be noticed that the wide spread of Sag errors in the 'After Welding'(ITP15) stage squeezes considerably in the 'After Manufacturing' (ITP20) stage that is when the cold masses are ready for the shipping to CERN and have undergone the second bending (re-shaping) to enter the tolerance range. The distribution spread in the successive measurements becomes then bigger and bigger up to reach, in the 'After Cold Test'(WP08) stage, values close to 'After Welding'. Sag trend for the 13 non-reshaped magnets, given in the right plot of Fig. 4.5, is characterized by a more constant spread around systematically increasing values.

Our interpretation is that the bending procedure gives cold masses in average

too curved and that the re-shaping corrective action is only short-term effective and not stable enough to withstand the successive pre-operative stages.

The Sag error distribution for all the cold masses up to now produced and tested is given in Fig. 4.6. The sample is composed by 880 cold masses and the two distributions refer to ‘After Manufacturing’ and ‘After Cold Test’ stages. The final Sag distribution, centered around a positive value testifies a systematic increase of the cold mass curvature throughout the pre-operative stages.

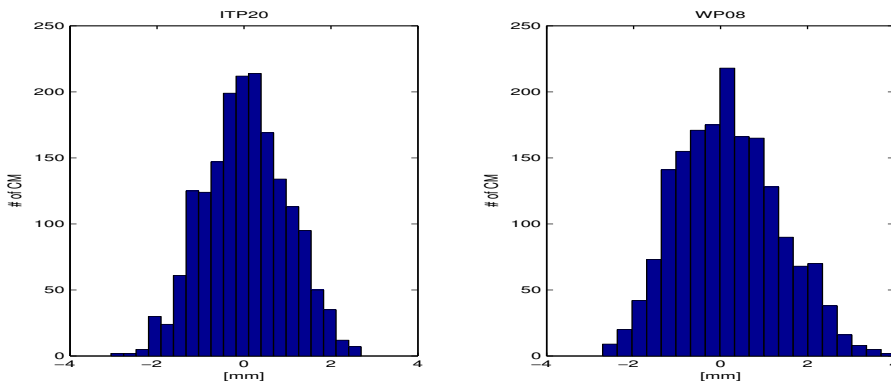


Figure 4.6: Distribution of Sag error after the manufacturing and after the cold tests for all the magnets produced and tested up to November 2005 (880 cold masses, 1760 Sags).

4.4 Cold mass End positions

Cold mass Ends are represented by the flanges welded at each tube extremities. Each cold mass has, therefore, four ends that must fulfill the imposed tolerance to guarantee the alignment of the multi-polar corrector magnets. Operatively, we extract the End positions from the 10th order polynomial curve, that fits the tube axis in vertical and horizontal plane, as shown in Fig. 4.2.

The evolution of the distribution of cold mass End positions in the transversal plane is shown in Fig. 4.7. The sample is composed by all the magnets measured at every stage from ‘After Manufacturing’ to ‘After Cold Test’ (34 cold masses, 136 Ends). Each graph refers to one of the four pre-operative stages: ‘After Manufacturing’ (ITP20), ‘Arrival at CERN’ (WP01), ‘After Cryostating’ (WP03) and ‘After Cold Test’ (WP08). End positions, given with respect to the nominal value, refer to both apertures and both sides. The surrounding histograms show the distribution in the vertical and horizontal planes; for each histogram the mean and the standard deviation at 1σ are respectively given by the point marker position and by the red bar width on the corresponding axis.

It can be noticed that at the ITP20 stage the Ends are well centered on the nominal position with a modest dispersion in both lateral (X) and vertical (Z) di-

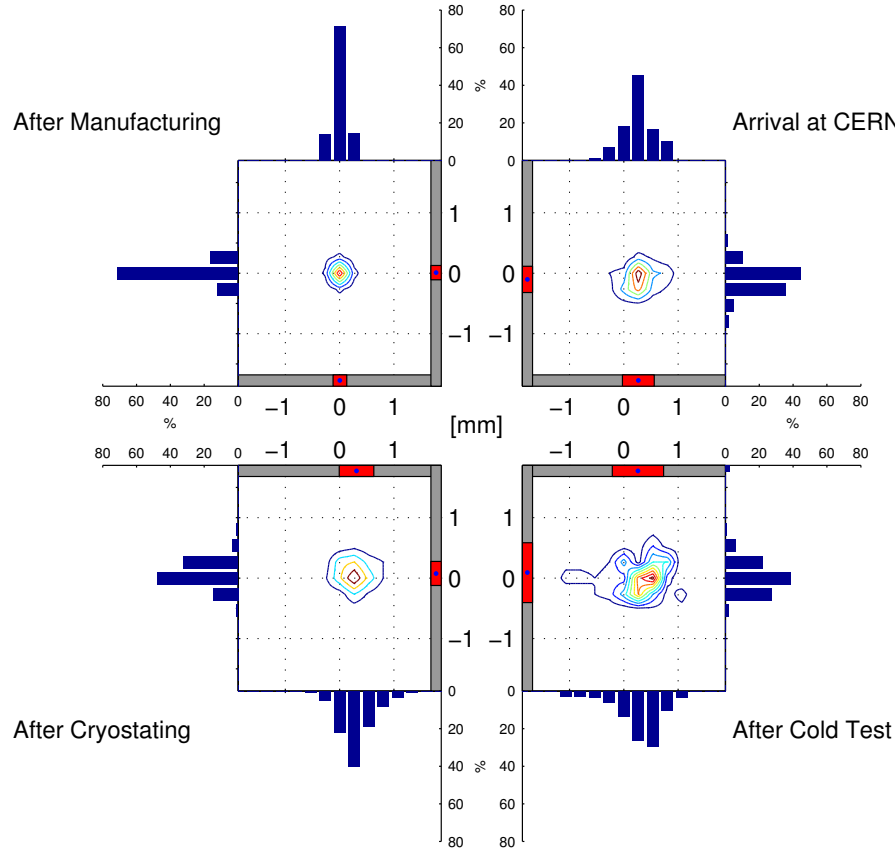


Figure 4.7: Distribution of End positions in the transversal plane at four pre-operative stages: ‘After Manufacturing’, ‘Arrival at CERN’, ‘After Cryostating’ and ‘After Cold Test’; 34 cold masses, 136 Ends.

rections. At the arrival to CERN the spread increases and is centered around a positive horizontal shift (i.e.: toward the center of curvature) and a slightly negative vertical shift (i.e.: toward the ground). After the cryostating the position condenses vertically around a positive value and diffuses horizontally around a greater positive offset. The final average position (After Cold Test) is close to nominal in vertical direction but misplaced of about 0.8 mm, with a dispersion two times bigger than the first step, in horizontal direction.

The analysis of the individual cold mass shape evolutions through the pre-operative stages revealed that, in some cases, the successive geometry checks on the same magnet can be characterized by different boundary conditions. An example is given in the top graph of Fig. 4.8. The green curve represents the cold mass axis shape in the vertical plane as measured in the industry before shipping to CERN (‘After Manufacturing’, ITP20), the red curve is the shape measured at CERN (‘After Cold Test’, WP08) and the crosses show the support locations. The three supports should have, in principle, the same vertical position in both the mea-

surements and the curves should locally overlap. In this case, instead, the central support at CERN is lower than in the industry whereas the two laterals are higher so that the two measurements cannot be directly compared. To correct the effect of the different boundary conditions we used the analytical model to identify and subtract the elastic deformation induced by the support misalignments. The result of the correction in the case presented is shown in the bottom graph of Fig. 4.8. We implemented the correction on all the cold mass geometries stored in the database and the corresponding normalized extremity positions are given in Fig. 4.9. The error trend throughout the stages clearly reflects the Sag variation. Right after the manufacturing the Ends are, in fact, well positioned but then the displacements progressively increase and after the cold tests the average has reached the tolerance limit.

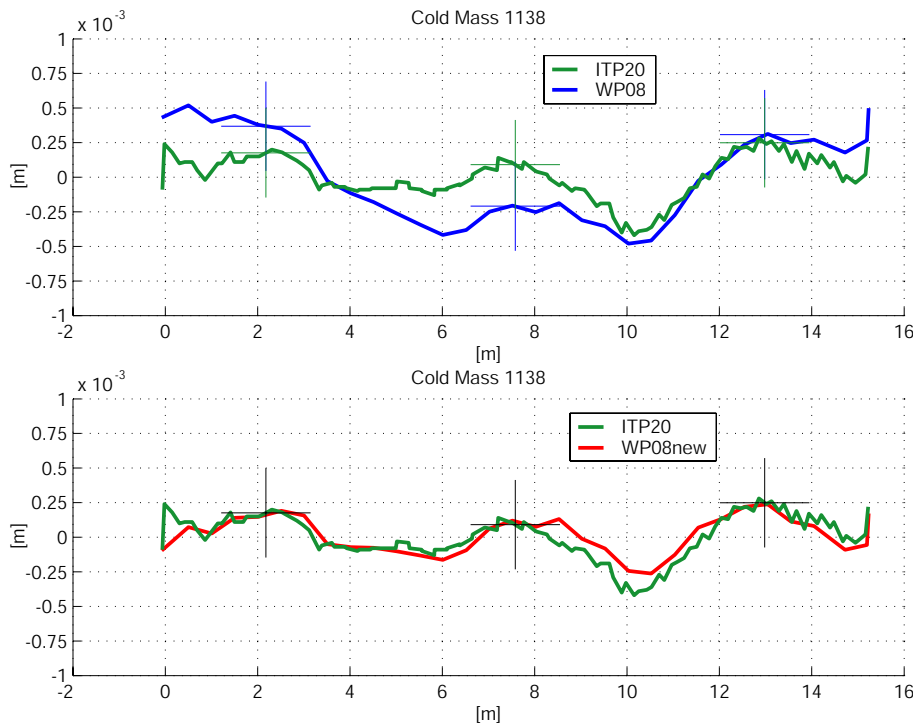


Figure 4.8: Vertical shape of cold mass 1138 as measured in the industry (ITP20) and at CERN (WP08). In the top graph WP08 data are the ones stored in the database, in the bottom graph they are corrected imposing the same vertical position of the supports.

We give the positions of the Ends for all the cold masses up to now produced and tested, in Fig. 4.9. The sample is composed by 880 cold masses that is 3520 Ends. The two distributions refer to ‘After Manufacturing’ and ‘After Cold Test’ stages. The final horizontal End positions, centered around a positive value, reflect the systematic increase of the cold mass curvature through the pre-operative stages.

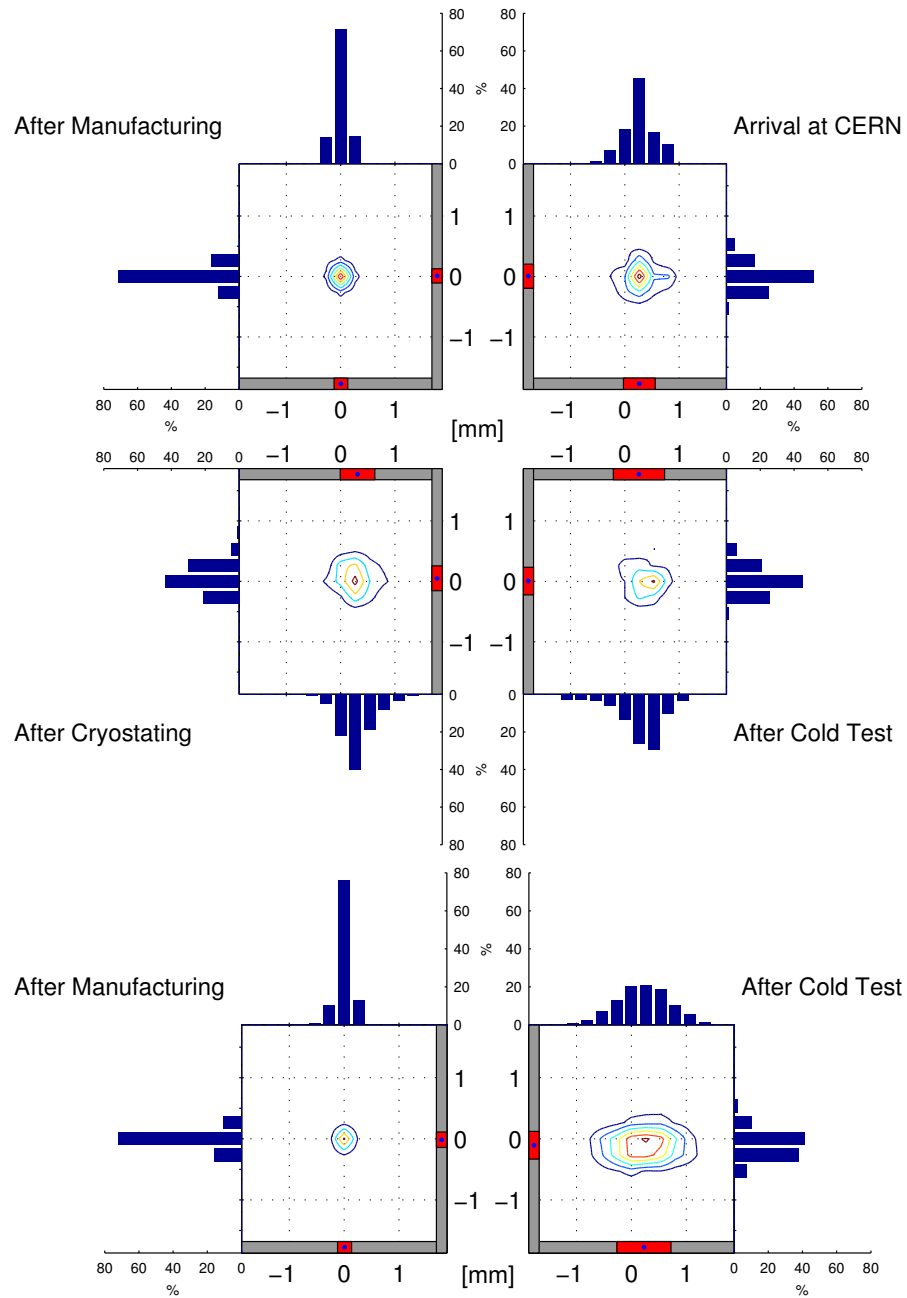


Figure 4.9: Distribution of normalized End positions in the transversal plane at four pre-operative stages (34 cold masses, 136 Ends) and just after the manufacturing and after the cold test (880 cold masses, 3520 Ends).

The vertical position, purged from the effect of elastic deformations, is in average close to the nominal and testifies a greater mechanical stability of the cold mass vertical shape, not affected by the bending treatment and stabilized by the gravity field acting on the considerable magnet mass.

4.5 Curvature correction

The shape degradation experienced by all the cold masses in the pre-operative stages can however be corrected before the installation in to the tunnel. The corrective procedure, implemented at CERN, consists in the modification of the faulty shape via the blocking of the central support in an appropriate position [24]. The drawback of this effective procedure is the time needed for the fine adjustment, customized for each magnet, to find the optimum support post position. As the three producing firms show three distinct degrees of change in shape, a possible alternative is based on the definition of a support post position unique for all the magnets produced by the same firm. To check the effectiveness of such a procedure we simulated the new correction on each produced magnet and we evaluated the effect in terms of extremity positions. Operatively we proceeded as follows: using the analytical model we computed, for each magnet, the optimum position of the central support post; then we averaged the value within the magnets produced by the same firm and we finally adjusted the magnets by this position ‘Per Firm’. If, after the correction, at least one of the correctors of each magnet exceeded the nominal position by more than 0.87 mm [23], the magnet was individually corrected in the optimum position.

In Fig. 4.10 we show the different effect of the two corrections for one of the magnets. The green curve represents the cold mass shape in the horizontal plane as measured in the industry before the shipping to CERN (‘After Manufacturing’, ITP20) whereas the blue curve is the shape measured at CERN (‘After Cold Test’, WP08). The curvature change is evident and the corresponding extremity displacement is close to 1 mm. In the top graph we simulate the correction (WP08 new) using the optimum support position: the original curvature and the extremity positions are completely recovered. In the bottom graph we simulate the correction achieved by imposing a support position that is the average of all the optimum positions for the magnets produced by the same firm. In this case the recover toward original is only partial.

We simulated the different corrections to all the magnets in the database measured at least at the first and at the last pre-operative stages. We can evaluate the results in terms of flange displacements between these two stages (‘After Manufacturing’ and ‘After Cold Test’) looking at the histograms of Fig. 4.11. From left to right we show the distribution of horizontal displacements without correction (observed), with the ‘Per Magnet’ and with the ‘Per Firm’ correction (simulated). The observed displacements are systematically positive with a broad dispersion, after the correction ‘Per Magnet’ the displacements are negligibly dispersed around the zero,

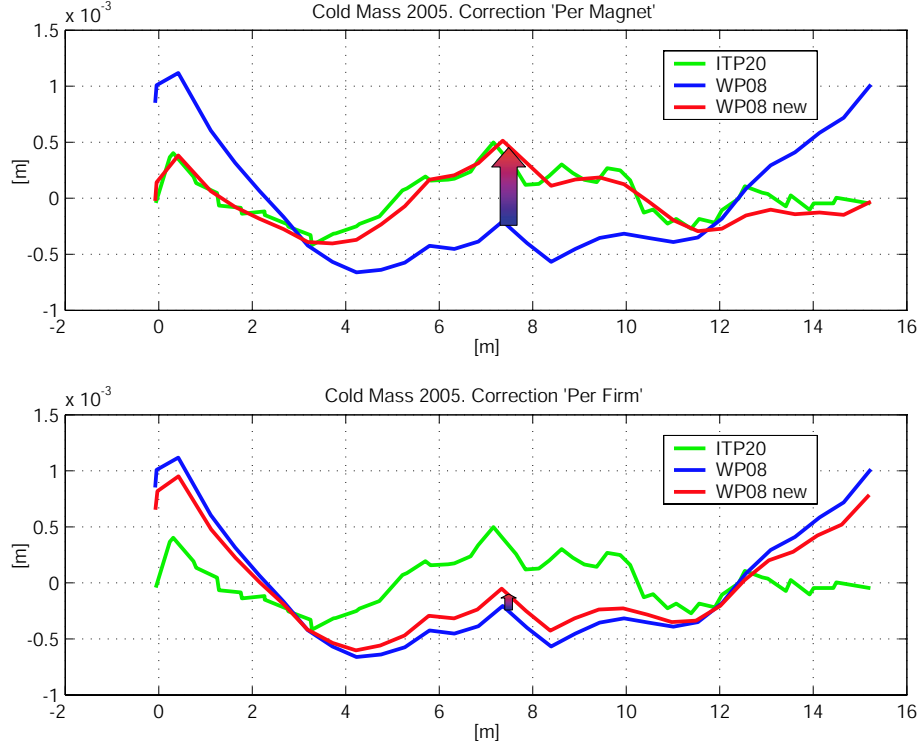


Figure 4.10: Effect of 'Per Magnet' (top graph) and 'Per Firm' (bottom graph) shape correction on the same magnet. The arrow shows the central support shift

After the 'Per Firm' correction the systematic positive displacement is zero and the surrounding spread is truncated at ± 0.87 mm.

The corresponding numerical results are reported in Table 4.3 in terms of average and standard deviation at 1σ . It can be noticed that the value averaged over all the magnets is very close to zero with both the old 'Per Magnet' and the new 'Per Firm' correction whereas the dispersion associated to the new correction is close to the original without correction. As the tolerances on the multipolar correctors are set at 0.3 mm on the systematic and at 0.5 mm (at 1σ) on the random component [11], the margin for the future production in case of no corrective action is very narrow. Therefore, as the new correction reduces considerably the average and, to a lesser

Table 4.3: Effect on extremity positions of different kinds of shape correction.

Corrective action	Mean [mm]	Std [mm]
None	0.2217	0.486
Per Magnet	0.0003	0.081
Per Firm	0.0007	0.380

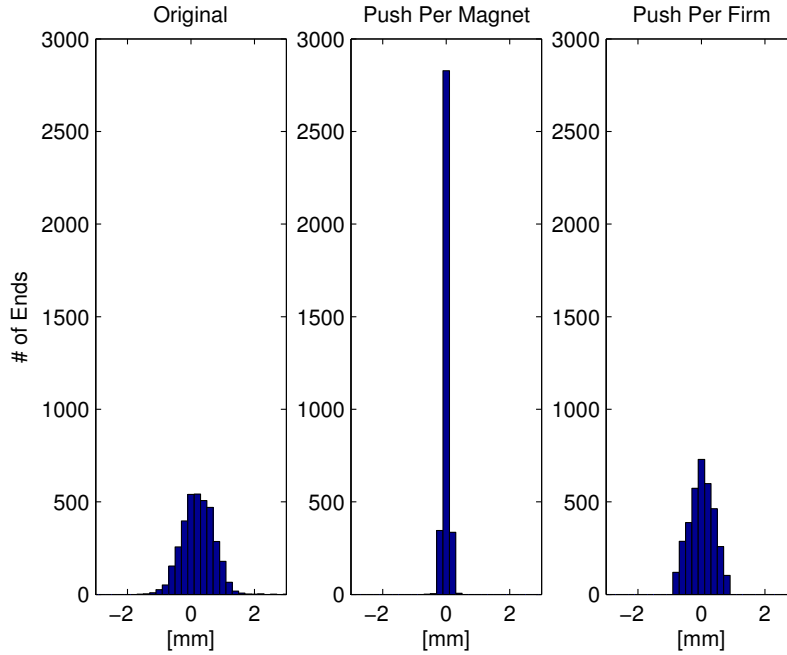


Figure 4.11: Distribution of End horizontal displacements from ITP20 to WP08 with no correction (left), ‘Per Magnet’ correction (center) and ‘Per Firm’ correction (right).

extent, the dispersion, the tolerance respect is much better guaranteed also for the forthcoming production.

4.6 Cold mass shape in vertical plane.

As explained in Chapter 2.3.1 the projection of the theoretical cold mass axis on a vertical plane is represented by a straight line. In the hypothesis of negligible cross-talk between vertical and horizontal plane, the effective vertical shape is determined by the gravity, acting on the magnet 30 t mass, by the structure flexural rigidity and by the support longitudinal and vertical positions. When placed on three supports the maximum sagitta should be around 0.3 mm with a slight dispersion due to the natural flexural rigidity spread in the population of the produced magnets. In spite of that, most of the magnets up to now measured showed a remarkably greater flexion in the vertical plane that can result in a harmful reduction of the mechanical clearance needed by the circulating beams. To understand this phenomena we carefully analyzed the magnet shapes from the assembly phase to their reception at CERN as explained in the next paragraphs.

4.6.1 Measured flexions.

The unexpected cold mass flexion is appreciable in Fig. 4.12 where the vertical shape of magnet 2022, measured at different stages, is plotted. The vertical sagitta, that we simply consider as the valley to peak vertical distance, almost reaches the noteworthy value of 1 mm that is almost three times bigger than what expected. This value would correspond to a flexural rigidity of around 50 MPa m^4 that is three times less than the one of the shrinking cylinder itself that is, by design, the back bone of the whole structure. To verify the systematic nature of this feature we analyzed

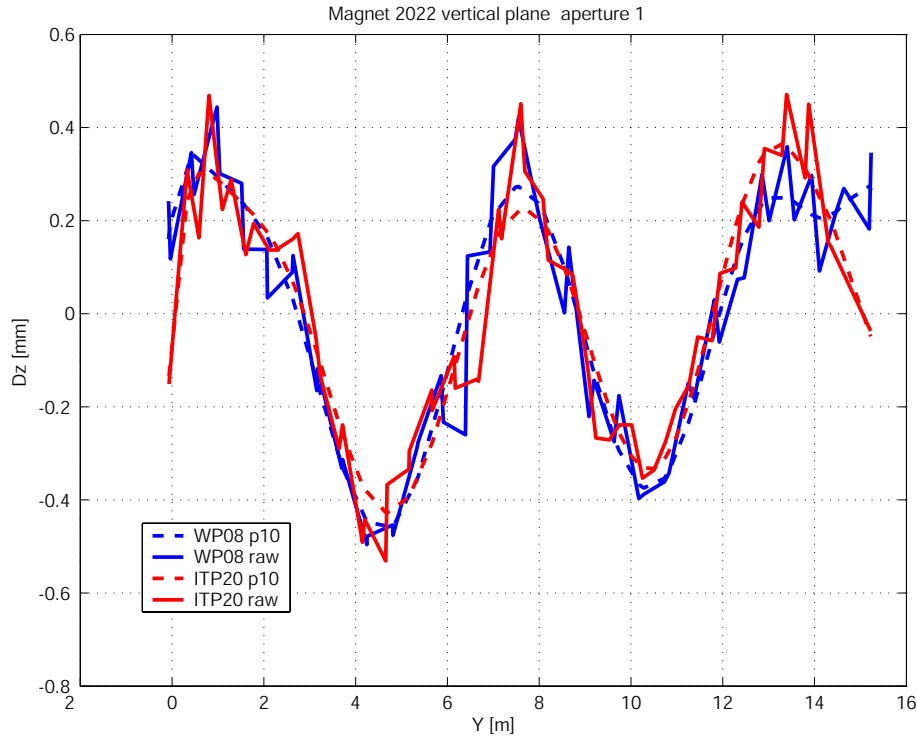


Figure 4.12: Vertical shape of magnet 2022 as measured right after the manufacturing (ITP20) and at the last pre-operative stage (WP08). Both raw data (solid lines) and 10^{th} degree polynomial interpolation (dashed lines) are plotted.

the current cold mass production by computing, for each available measurement, the distance between the maximum and the minimum vertical coordinate in each one of the two valleys between the supports (valley to peak vertical distance). To smooth out the measurement noise we performed this operation on the 10^{th} degree interpolating polynomial as we did in other analyses (see Paragraph 4.2) and, by mean of the cold mass analytical model (see Paragraph 3.2), we pre-processed all the data in order to filter out the effect of vertically misaligned supports. In Table 4.4 we give the results concerning the measurements taken in the industries and at CERN corresponding, respectively, to the work packages ITP20 and WP08. Hereby we

Table 4.4: Peak to peak analysis of measurements on two and on three supports. Number of magnets per sample is given in parentheses.

	ITP20 (540)		WP08(106)	
[mm]	Mean	Std	Mean	Std
CC	0.501	0.153	0.513	0.149
NC	0.580	0.146	0.564	0.146
TOT	0.541	0.155	0.539	0.149
	ITP20 (106)		WP08(106)	
[mm]	Mean	Std	Mean	Std
CC	0.501	0.154	0.513	0.149
NC	0.581	0.148	0.564	0.146
TOT	0.541	0.156	0.539	0.149

provide the statistical values of the gap size for the two valleys separately ('CC' and 'NC') and together ('TOT'). In the upper part we give the values for all the magnets whereas in the bottom part we consider a subset of 106 magnets that, at the time of our study, were measured at both stages.

The reported values show that the vertical sagitta is systematically set around 0.54 mm with a modest dispersion. Furthermore the statistical parameters remain constant for different magnet populations. It can also be noticed that the cold mass part between the connection side and the central foot presents a sagitta 15 % smaller than the other part as a consequence of the non-symmetric distribution of weights along the cold mass length.

At this point we considered worthwhile to check for the presence of a systematic vertical shape fault in the entire magnet production. As we can only measure magnet shape deformed by gravity, we had to subtract the effect of gravity and find out the 'original' shape as explained in next section.

4.6.2 Intrinsic shape and gravity effect

Operatively we studied a group of magnets for which one of the measurements was taken on a bench with only two supports instead of the nominal three so that, by comparing the measurements on two and on three supports, we were able to identify the gravity effect and to subtract it from the measurement. For each magnet we took the average between the two apertures and we fitted the analytical model on it. By doing this for the two and three supports cases we obtained two values of the flexural rigidity and two sets of residuals distributed along the axis. The two rigidities should ideally match, the residuals should match as well and give us the original magnet shape.

In the magnet model the deflection induced by gravity depends on the following parameters:

- cold mass density
- cold mass length
- cold mass flexural rigidity (EI)
- support longitudinal positions
- support vertical positions

In the best fit procedure, we fixed the density and length of the cold mass and we left as independent variables the support vertical and longitudinal positions along with the flexural rigidity. Indeed for the two and the three support cases we had 5 and 7 variables, respectively. The analysis result are given in Table 4.5.

Table 4.5: Values of flexural rigidity EI computed from measurements of cold mass on two and on three supports

3 Supp.	EI [MPa m ⁴]	Z _{s1} [m]	Z _{s2} [m]	Z _{s3} [m]	Y _{s1} [m]	Y _{s2} [m]	Y _{s3} [m]
Mean	133	1.84E-4	8.25E-5	1.81E-4	2.44	7.60	12.76
Std	26	7.65E-5	1.31E-4	8.59E-5	0.13	0.21	0.22
2 Supp.	EI [MPa m ⁴]	Z _{s1} [m]	Z _{s2} [m]	Y _{s1} [m]	Y _{s1} [m]		
Mean	141	7.28E-4	7.21E-4	3.69	11.47		
Std	16	1.19E-4	0.98E-4	0.09	0.12		

It can be noticed that the agreement between the flexural rigidity EI values on three and two supports is well within the related dispersions but both of the values are smaller than the expected 180 MPa m⁴. The vertical support positions Z_{sx} of few tenths of millimeter are in both the cases realistic; the spread of the horizontal support positions Y_{sx} is compatible with the temporary supports used in the industries whose size can vary between 10 and 40 cm. It must be noticed that in the three supports case the mean values of the lateral supports do not match exactly the expected values of 2.18 and 12.98 m; this can be however explained by the trim of the extremities in the best fit procedure required for practical reasons.

Generally, in each magnet, the computed flexural rigidities are slightly smaller for the three than for the two supports case and the average discrepancy is 4±1%. This can be related to the effect of shear between laminations that we didn't take into account considering the high length over diameter ratio of the cold mass. Such a ratio is smaller when the cold mass is on three supports rather than on two so that the effect of the shear, is bigger in the first than in the second case.

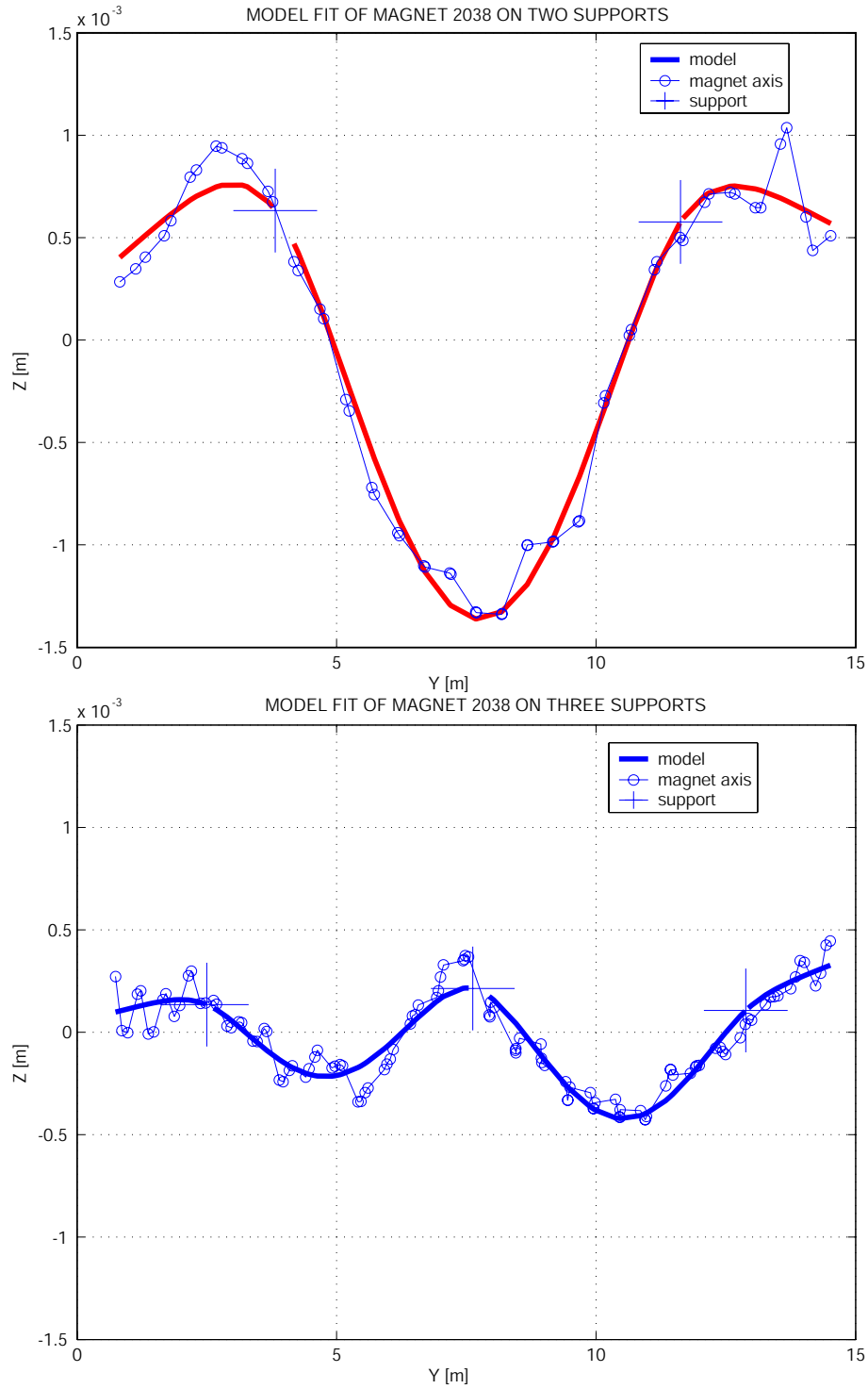


Figure 4.13: Result of best fit of magnet 2038 vertical deflection on two supports (top graph) and on three supports (bottom graph).

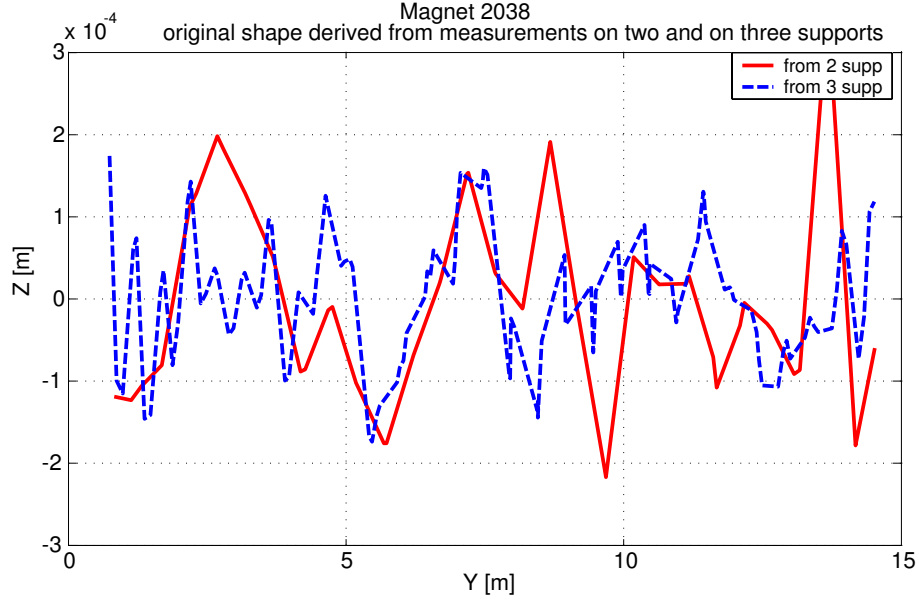


Figure 4.14: Original axis shape of magnet 2038 derived from measurement on two and on three supports (solid and dashed line, respectively).

Currently we are investigating, by means of a specific model, if the shear effect could also be responsible for the discrepancy between data and the expected EI value of 180 MPa m^4 . In Fig. 4.13 we show the graphical result of the best fit procedure for the same magnet on two and on three supports. The original shapes extracted from the measurements on two and on three supports are shown in Fig. 4.14. The two curves match well within the measuring error and generally the fit on two supports is more accurate because the deflection induced by gravity is much bigger than the intrinsic shape imperfections and measuring errors. In this case, and in the others analyzed, both the curves show a modest spread around the Y-axis thus neglecting the presence of systematic faults in the vertical shape of the produced cold mass.

4.7 Summary

In this Chapter we presented the analysis of the geometry of nearly one thousand cold mass produced, delivered to CERN and tested. We defined two main geometrical parameters, the Sag and the End positions, and we monitored their evolution across the pre-operative stages of each magnet. The production, shared by three different producer, results qualitatively and quantitatively quite homogeneous. We observed, in fact, a good quality of cold mass geometry right after the manufacturing although followed by a systematic curvature change in the successive stages. At the last pre-operative stage, the geometric instability results in a wide range of curvatures set around a value bigger than nominal but still within the limits.

The horizontal position of the Ends reflects, at every stage, the curvature increase and at the last pre-operative stage the mean value is close to the limits.

To observe the End positions in the vertical plane we had first to correct the geometry database data. We used indeed the cold mass analytical model to filter out the effect of different boundary conditions between successive measurements of the same cold mass. The analysis of the corrected geometries proved that cold mass geometry is more stable in the vertical plane than in the horizontal so that the accuracy obtained in the industry is still present after the last stage.

After the final pre-operative stage, the horizontal geometry of the cold mass can be corrected by laterally shifting and fixing the central support in a new position. Since defining the support shift individually for each magnet is a resource-demanding procedure, we evaluated the efficiency of an alternative approach. We simulated the effect of the original ‘Per Magnet’ and of the alternative ‘Per Firm’ correction in which the central support position is common to all the magnets produced by the same firm. We compared then the effect of the different corrections and of no correction at all and we proved that the alternative correction cancels the systematic component of the curvature change and grants enough margin on the random for the rest of the production.

The quality of the cold mass vertical shape is strictly correlated to the maximum vertical deflection between the supports induced by the gravity. The values measured in the cold masses up to now produced generally exceed the expected 0.3mm up to reach values three times higher that can produce detrimental effect on machine performance. To see if such a feature was related to a systematic fault of cold mass geometries we proceeded to disentangle the deflection induced by gravity from the intrinsic shape imperfections. On one hand the analysis of the vertical shape purged from the effect of gravity ensured the absence of systematic faults in the cold mass geometry; on the other hand the deflection induced by gravity resulted bigger than what expected corresponding to a flexural rigidity 20% smaller than the nominal value.

Chapter 5

Geometrical issues on dipole production

5.1 Introduction

This chapter concerns two crucial measuring procedures to verify the quality of magnet production. They are indeed the verification of the geometric axis and of the main field orientation; the aim of the study is to evaluate their maximum achievable accuracy.

First we focus on the complex measuring procedure implemented to check the respect of the geometric tolerance: we evaluate its intrinsic accuracy, by mean of numerical simulation, and we compare it with the operative accuracy of the actual procedure. Then we test the influence of a measuring bench with non perfectly aligned supports, on the accuracy of the main field direction measurement.

5.2 Accuracy of geometric tolerance checking procedure

5.2.1 Measuring procedure

As the cold mass series production is performed in parallel by three different mechanic industries, a careful procedure was defined to check in-situ the compliance of the geometrical tolerance. The requirement for high precision and portability pushed toward the employment of laser trackers and probes (from now on: moles) sliding along the apertures [25]. Each tube axis is measured by pulling a mole, equipped with a reflector, inside the tube along its whole length. In this way the 3D path of the mole, measured by mean of the laser tracker, provides the tube axis shape. It is straightforward that, to measure both the tubes, the laser tracker must be placed in two different locations: each one in front of the tube to measure. Furthermore,

as the laser tracker accuracy is proportional to the closeness of the point to measure (see Table 5.1), each tube shape is acquired from two opposite locations: at Connection and at Non-Connection extremities, as shown in Fig. 5.1. From now on we will refer to this kind of measurement, in which the 3D shape of the cold mass is acquired from different locations, as to a ‘multi-station’ measurement.

Table 5.1: Accuracy of the LTD500 LEICA laser tracker.

Angle resolution	0.14“
Distance resolution	1.26 μm
Reproducibility of a coordinate*	± 5 ppm ($\mu\text{m}/\text{m}$)
Absolute accuracy of a coordinate for non-moving target (static)*	± 5 ppm ($\mu\text{m}/\text{m}$)

*The accuracy shown above is stated as a 2σ value.

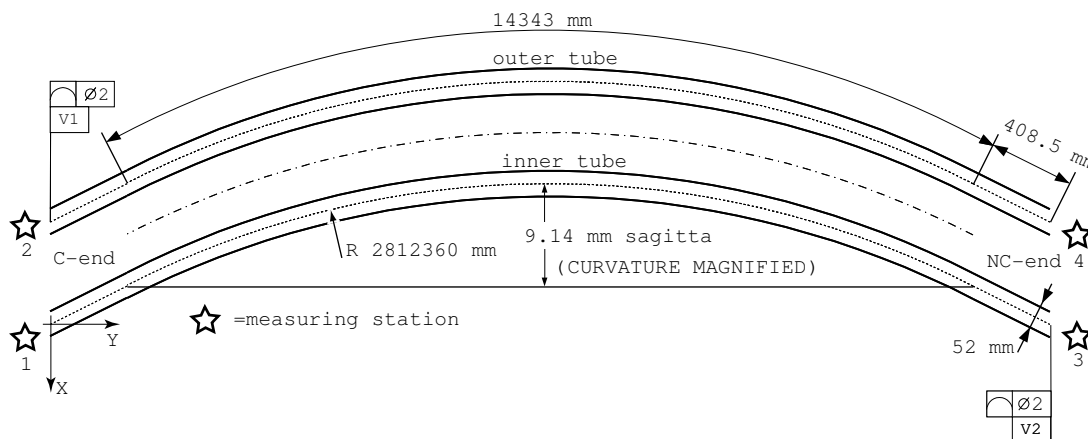


Figure 5.1: Theoretical geometry of the cold mass in assembly condition in the horizontal plane. The four stations for the laser tracker around the dipole are also shown.

Cold mass tolerances are given with respect to the theoretical beam trajectories (also called geometric axes). In each cold mass the two beams trajectories are identified through a least square fit on the measured tube axes. To refer the axis measurements, taken from different stations, to the theoretical beam trajectory it is necessary to follow two main steps:

- the transformation of all measurements performed in the local reference system of each station into a common coordinate system that we define ‘operative’ (or global);

- the transformation from the operative coordinate system to the one built on the beam trajectory that we define ‘theoretical’.

To transform the measurements from different stations into the operative referential a set of fixed points common to all the stations is conveniently defined. This set of points, called ‘network’, is made of 8 to 10 points surrounding the magnet as shown in Fig. 5.2. Actually the network is a set of points needed to operate a coordinate transformation in the 3D space from the local referential of each measuring station to a common referential. In theory, to define the coefficients of the roto-translation matrix for such a coordinate transformation, only three common points need to be considered. However in the real case, affected by the measuring error, network points measured from different stations do not match exactly and the only way to compare them is through a least square fit. Thus, the number of points used is higher than the theoretical three to grant the necessary redundancy for the least square algorithm. The algorithm that performs the coordinate transformation every time that the laser tracker is placed in a new station, is called ‘bundle’. This function, embedded in the laser tracker acquisition software, fits the network points measured by different stations and, through an iterative process, sets the operative reference system with respect to the referential of each station. Data coming from

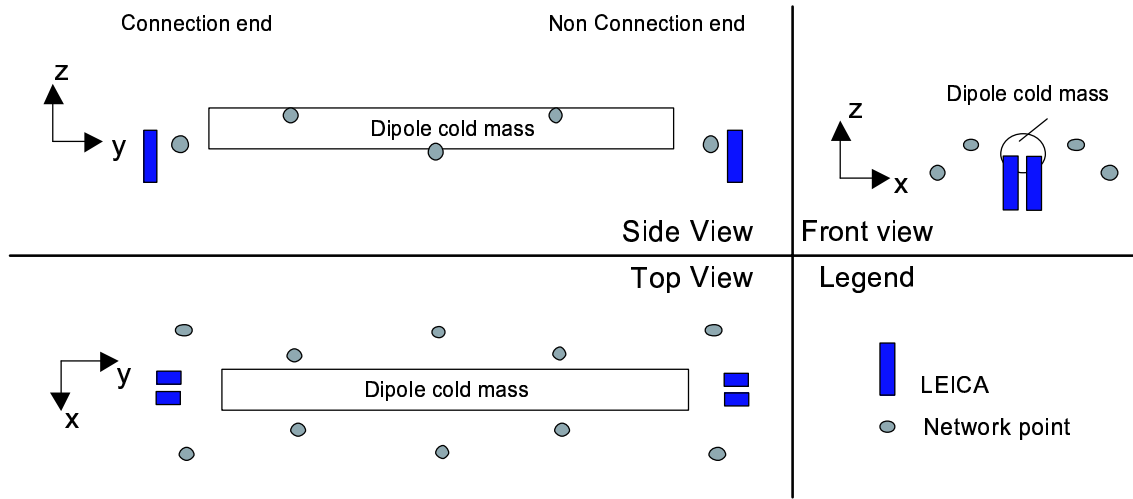


Figure 5.2: Network points and laser tracker positions around the cold mass.

a typical multi-station measuring session are presented in Fig. 5.3. Each dipole is characterized by two axes: the inner and the outer tube axis. For each axis the data taken from two opposite stations are converted to the same coordinate system and then merged. The difference in the vertical and in the horizontal plane between the measured axes and the theoretical ones (see Chapter 4.2) are computed and plotted versus the dipole length as shown in Fig. 5.3. In this particular case we can see that in the horizontal plane the two tubes (i.e. the cold mass) are too bent (as explained in 4.3). Magnet extremities are, in fact, closer to the center of curvature, situated in

the positive X region, than the central part. In the horizontal plane is clearly visible the effect of gravity that induces a sagitta of some tenths of millimeter between the three supports nominally located at: 2.18 m 7.58 m and 12.98 m from Connection end.

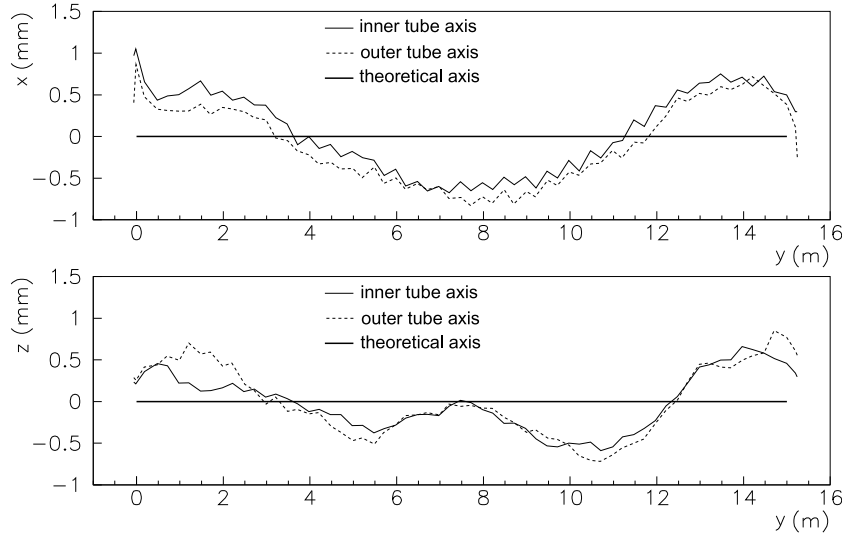


Figure 5.3: Horizontal (upper graph) and vertical (lower graph) profiles of the dipole axes with respect to the theoretical shape.

5.2.2 Saw-tooth effect

Looking at the profiles in Fig. 5.3, an evident saw-tooth pattern can be noticed in both vertical and horizontal planes for both the tubes. If, for each tube, data acquired from Connection and from Non-Connection ends are plotted separately this effect disappears, as shown in Fig. 5.4 where only the inner tube is taken into account. In that plot the original saw-tooth effect is replaced by an in-plane roto-translation between the curves obtained from the two opposite stations. This assumption can be verified by considering the difference between the curves shown in Fig. 5.4 for both the horizontal and the vertical plane. The evident linear trend ensures us, thanks to the particular geometry of the dipole (as explained in Appendix D), that the discrepancy between the curves can be traced back to a mismatch between the common reference systems (that should in principle overlap) evaluated by the two opposite stations.

Next section presents a statistical analysis of the up to now experienced saw-tooth effect in terms of rotation and translation between the reference systems evaluated by opposite stations.

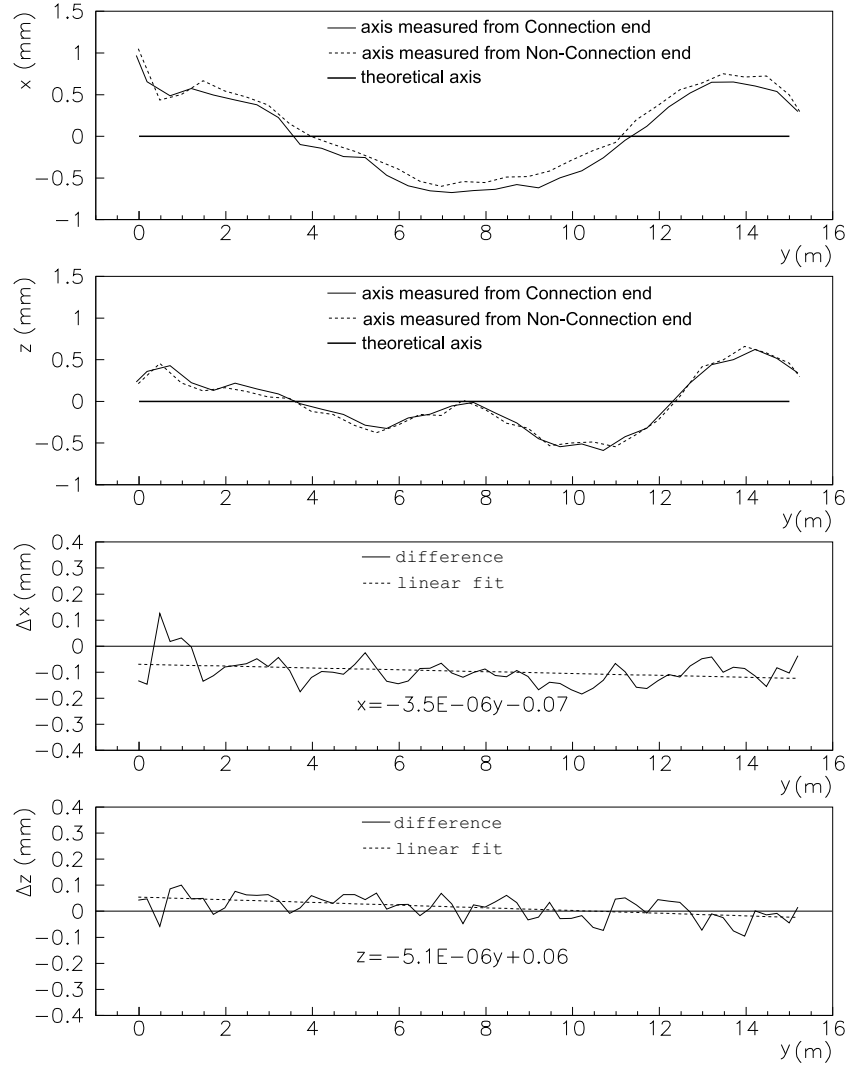


Figure 5.4: From top to bottom: Horizontal (1^{st}) and vertical (2^{nd}) profiles of the dipole inner tube axis as measured from Connection and Non-Connection ends, horizontal (3^{rd}) and vertical (4^{th}) difference between measurements from Connection and Non-Connection ends.

5.2.3 Parameters for analysis and experimental results

A statistical analysis of the saw-tooth effect has been carried out on the vertical and the horizontal plane separately; from now on we will refer to the horizontal plane since it resulted the most critical. We analyzed some measuring sessions carried out by different operators on different magnets. We evaluated the difference between the axis of the same tube measured from opposite station in terms of two parameters: the shift q and the rotation p . Operatively this two parameters correspond to the polynomial coefficients of the line, shown in Fig. 5.4, that fits the axis difference.

Whereas the magnet type should not influence the saw-tooth effect, the operator carefulness could deeply affect it by choosing, for example, the proper network arrangement or by ensuring the tracker steadiness during the measurement. Among the operators we refer to, the team number 3 set two auxiliary stations beside magnet flanks to increase the network points redundancy needed by the bundle algorithm. Nevertheless, as it can be deduced from the results of the analysis shown in Table 5.2, the accuracy improvement is not noticeable. The table reports the characteristic parameters p and q averaged over inner and outer tube in the horizontal plane for each magnet; the saw-tooth height h , averaged over the dipole length, is also reported in order to have a more tangible idea of the analysis results. In spite of the little amount of total measurements performed by each operator, that could represent a limit for the statistical value of the analysis, some important considerations can eventually be done, as reported in the next section, through the comparison with the numerical simulation. A preliminary important issue coming from the analysis of the reference system roto-translations and saw-tooth heights is the absence of coarse errors done by the three operators during the measurements and the substantial equivalence of the three measuring procedures.

Table 5.2: Statistical values of rotation and shift between opposite stations and saw-tooth height. Values are given in rad for p and in mm for q and h .

Operator	# of meas.		Mean	Std
1	10	p	$-3.2 \cdot 10^{-6}$	$1.8 \cdot 10^{-5}$
		q	-0.04	0.24
		h	0.114	0.067
2	14	p	$8.1 \cdot 10^{-7}$	$6.0 \cdot 10^{-6}$
		q	-0.09	0.10
		h	0.094	0.045
3	14	p	$-2.9 \cdot 10^{-6}$	$9.0 \cdot 10^{-6}$
		q	0.04	0.12
		h	0.079	0.033

5.2.4 Numerical simulation and experimental result comparison

To estimate the best accuracy achievable in a multi-station measurement session we implemented a Montecarlo based numerical simulation. For every session step (i.e. network points or axis points acquisition) the measurement of each single point has been simulated by a random extraction from a normal distribution centered on the theoretical position of the point itself.

It must be pointed out that the cartesian coordinates of the measured point are worked out from spherical polar coordinates; the laser tracker measures, in fact, the point distance with an interferometer and the spherical angles ,vertical and horizontal, by mean of angular encoders embedded in the head. Hence, the resulting accuracy on the cartesian coordinate is very high in the longitudinal direction (Y) and linearly dependent on the distance in the transversal plane (directions X and Z).

Following the measuring system specifications, given in Table 5.1, the *rms* of each distribution in the transversal plane has been computed as a linear function of the distance between the laser tracker and the point itself [26] whereas the distance error has been considered negligible.

In this way we were able to reproduce the propagation, through the whole measuring procedure, of the error introduced by the laser tracker accuracy. We found that the largest loss of accuracy is due to the definition of the common reference system that is not directly measured (and thus affected by the bare laser tracker accuracy) but it is worked out from the network points measured by opposite stations (and thus affected by a combination of the related errors). After one hundred iterations the simulation provided the statistical discrepancy between the axis profiles obtained by two opposite stations as a function of machine accuracy and network point dispositions. The graphical simulation outcome is given in Fig. 5.5. The central plot shows the theoretical tube axis of one tube and the network points as if they would be measured from two opposite stations. The red and blue stars show the position of Station 1 and Station 2, respectively. Axis and network points are represented by blue squares when measured from Station 1 and by red crosses from Station 2. By looking at the four magnifying boxes around the central plot, it can be noticed that the points seen from Station 1 are affected by the bare laser tracker accuracy. The related dispersion is, in fact, very small in the longitudinal direction and proportional to the distance in the transverse direction with an *rms* of 0.0025 mm/m. The points seen from Station 2 show, instead, a wide dispersion in the transversal direction that is a combination of the error affecting the network points measurements from both the sides and that does not depend from the relative location of the point with respect to the station.

The numerical simulation results in terms of rotation p and shift q , summarized in the left part of Table 5.3, show that a finite roto-translation between the curves is intrinsic in the ideal procedure itself but the related saw-tooth effect h is smaller

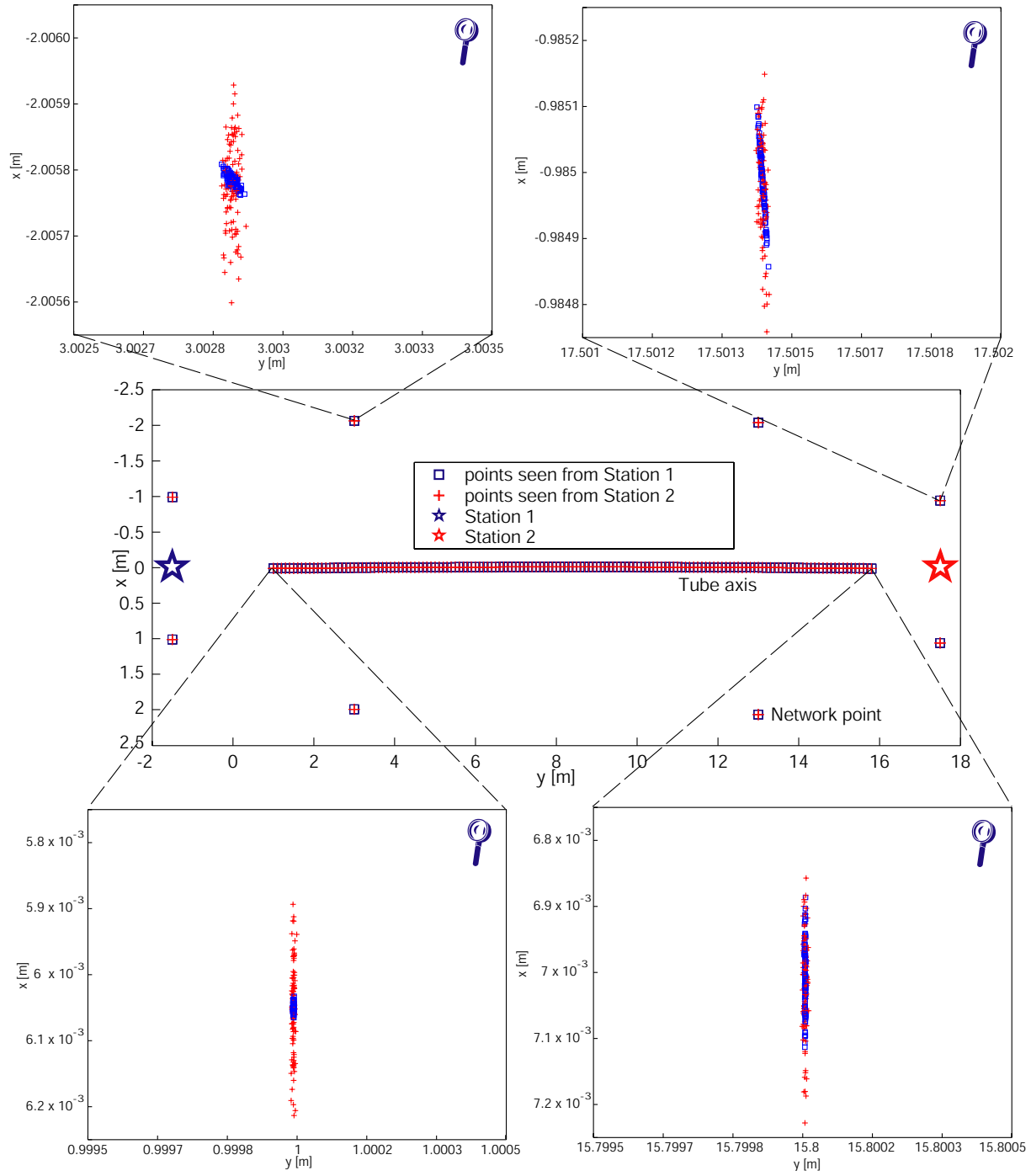


Figure 5.5: Graphical output produced by numerical simulation.

with respect to the experimental one given in Table 5.2, both in terms of average and standard deviation.

Before going on through the comparison with the experimental data, it must be pointed out that, our discriminating parameter is not the average but the standard deviation. In fact the experimental average represents a statistical bias that, because of the random nature of the error, is supposed to go to zero over a large ($\sim \infty$) number of samples ($\langle x_\infty \rangle = 0$). In presence of few (n) measurements, as in this case, it is sufficient that the related average $\langle x_n \rangle$ satisfies the condition $\| \langle x_n \rangle - \langle x_\infty \rangle \| \leq \frac{3\sigma}{\sqrt{n}}$, where n is the number of the considered cases and 3σ is three times the standard deviation of the measurements to ensure a 98.8 % confidence level. Hence this condition is satisfied for all the three sets of measurements, the asymptotic value of the average is zero and the relevant quantity is the standard deviation.

By looking separately at the components p and q that cause the saw-tooth it can be seen a different contribution of the shift between simulation and measurements. Such a specific discrepancy must be due to a phenomenon arising during the measurements and causing a virtual shift without rotations of the reference systems. A potential explanation can be given by a movement in the horizontal plane of the laser tracker head between the network and the axis measurement. This kind of shift can be provoked by the stabilization of the tracker base in contact with the ground during the first part of the measurement on a new station i.e. during the network point measurements as was detected by the measurement team number 2 [27]. To confirm this hypothesis, we introduced in the simulation a distribution of laser tracker head shifts in horizontal directions between the network and the axis measurement. By assuming a normal distribution of these movements with mean 0 mm and sigma 0.1 mm (corresponding by lever effect to a base-ground accommodation of 0.03 mm), simulation results shown in Table 5.3 are in good agreement with the experimental values of Table 5.2 and it can be noticed that, according to the hypothesis, rotations are not affected by this small laser tracker displacement.

Table 5.3: Results of the numerical simulation after 100 iterations. Values in the right table include ground accommodation. Values are in rad for p and in mm for q and h .

Steady			Not Steady		
	Mean	Std		Mean	Std
p	$-2.98 \cdot 10^{-7}$	$4.59 \cdot 10^{-6}$	p	$-2.36 \cdot 10^{-7}$	$3.97 \cdot 10^{-6}$
q	0.004	0.04	q	-0.015	0.16
h	0.065	0.01	h	0.125	0.095

From the comparison between numerical simulation and experimental data, it can be stated that the current procedure to measure the geometrical tolerances of

the dipole series production is carried out with a high carefulness that pushes the final accuracy close to the intrinsic limits of the procedure itself. The detected saw-tooth effect, is a balanced combination of virtual rotations and translations between the common reference system as seen by different stations. Whereas the first effect is intrinsic in the procedure because strictly related to laser tracker accuracy and network point dispositions, the second can be minimized by checking the mechanical stabilization of the laser tracker in each station. In absence of any corrective action to the procedure our suggestion is to consider valid measurements with the current accuracy level that in terms of saw-tooth average height is around 0.1 mm.

5.3 Influence of test bench planarity on field orientation measurement

The series production (assigned to three European firms) requires to check, in every magnet, the respect of the tolerance imposed on the main field angle with respect to the magnet mean plane. The impossibility to measure the mean plane and the field orientations on the same measuring bench led us to define a procedure suitable for the standard assembly process. Here we describe the test that allowed us to estimate the maximum error associated to the procedure. We also provide a value of cold mass torsional stiffness derived from test measurements.

5.3.1 The main field angle

The direction of the magnetic field produced by each one of the 1232 superconducting dipoles to bend the beam along the 27 Km-long circular trajectory, is an important parameter to ensure the LHC expected performance. The dipolar field direction must be orthogonal with respect to the beam orbit plane within ± 1 mrad [28]. On one hand the beam orbit plane is identified as the one that fits best the two aperture axes in the least square sense; it is called indeed the *rms* plane (or: geometric plane) and its orientation is available only after a complete geometric measurement [9]. On the other hand, the main field orientation is obtained from the standard field quality measurement implemented in the industries on test benches that, for practical reasons, are not suitable for standard geometric measurements. In order to reliably refer the main field orientation to the geometric plane, it is therefore crucial to estimate the potential variation of the plane orientation between the two measurements. The proposed procedure is to estimate the geometric plane orientation on the test bench for the magnetic measurements, through the orientation of the end covers (i.e. the cold mass extremities). To verify that this simple procedure is not undermined by a longitudinal twist induced by the test bench support poor planarity, a dedicated test was carried out. The test also gave us the opportunity to estimate the magnet stiffness to torsion through the comparison with an analytic

model.

5.3.2 Poorly planar bench influence test

The test aims to estimate the error associated to the evaluation of the geometric plane direction through the end cover orientations when the test bench supports are not exactly planar. The test is conceptually divided into four parts:

- simulation of a test bench with misaligned supports,
- evaluation of the geometric plane orientation through a complete axis measurement (reference value),
- evaluation of the geometric plane orientation through the end cover orientations (estimated value),
- comparison between reference and estimated values.

To limit the amount of resources needed and the interference with the complex logistic of the magnet testing and cryostating facility, we decided to replace the complete axis measurement by the measurement of the local mid-plane orientation at the longitudinal location of the three supports. All the test have been done on a cold mass assembly with the three standard steel pads (two lateral pads, each one positioned at 2.18m from the closest end and a central one 7.58m far from both ends).

Support misalignments have been simulated by placing 3mm, 2mm and 1mm shims between the bench supports and the cold mass pads lateral edge as shown in Fig. 5.6. Several different shims have been placed in different configurations in order to reproduce the worst possible misalignments, by far bigger than what is expected in the real test benches. In Fig. 5.6, for example, the test configuration is ‘OIO’ meaning that the shims, whose default thickness is 3mm, are placed under the ‘In’ edge of the central support and under the ‘Out’ edge of the other two pads. ‘In’ means closer to the center of cold mass curvature and ‘Out’ farther from it; looking at cold mass from Connection Side the center of curvature is on the right.

The geometric plane evaluation based on the end cover orientation was carried out by mean of two gauging unit (jig), as the ones to be used in the industries. Each one of them measures the orientation of the end cover with respect to gravity. The instrument, shown in Fig. 5.7, consists in a flat aluminum ‘C’ shape to be mounted on the end covers taking advantage of the holes (*dc9*, *dc11*) used for geometric measurements. The two branches of the ‘C’ are positioned downward; on the top a digital inclinometer is fixed and connected to a digital volt meter. The inclinometer itself and the not perfect symmetry of the support produce a systematic offset, with respect to gravity, that affects each single measurement. In order to cancel this effect two angle evaluations are performed by measuring twice the

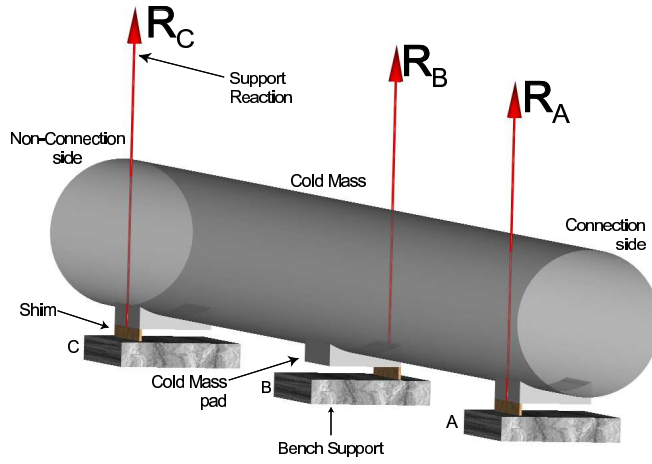


Figure 5.6: Set Up layout and reaction forces in supports. The support configuration shown is ‘OIO’: 3mm shims under the three cold mass supports

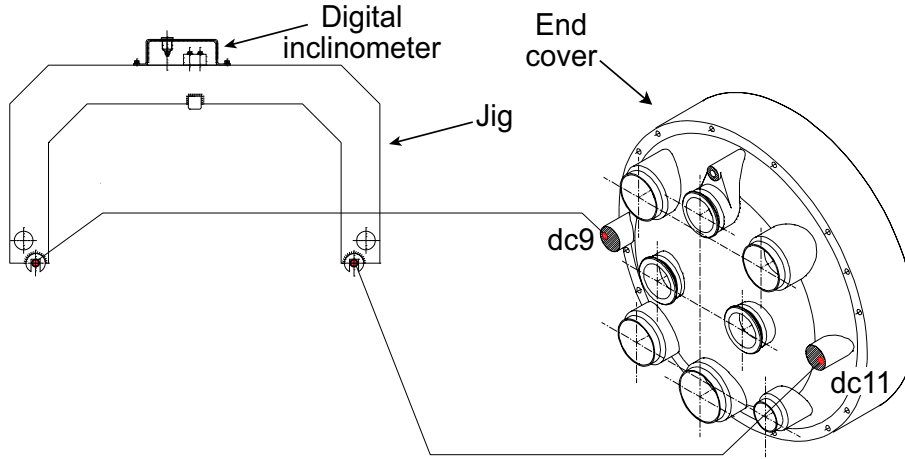


Figure 5.7: Front view of jig and details for installation on end cover.

same end cover, rotating the instrument of 180 degrees along the vertical axis. The two measurements (opposite in sign because of the reference system rotation) are affected by the same offset so that their half-difference gives the real orientation with respect to gravity whereas their half-sum gives the offset. By analyzing the dispersion of the offset value over all the measurements we got a reliable estimation of the instrument reproducibility that resulted in 0.05 mrad at 1σ . The geometric plane direction w.r.t. gravity (α_{ends}) is given by the average of the two end cover orientations.

The geometric plane evaluation based on the cold mass complete geometry did not rely on a standard dipole geometry measurement. As already explained, we measured the orientation of three cold mass sections matching the support locations (A, B and C in Fig. 5.6). We used three digital inclinometers placed on the top

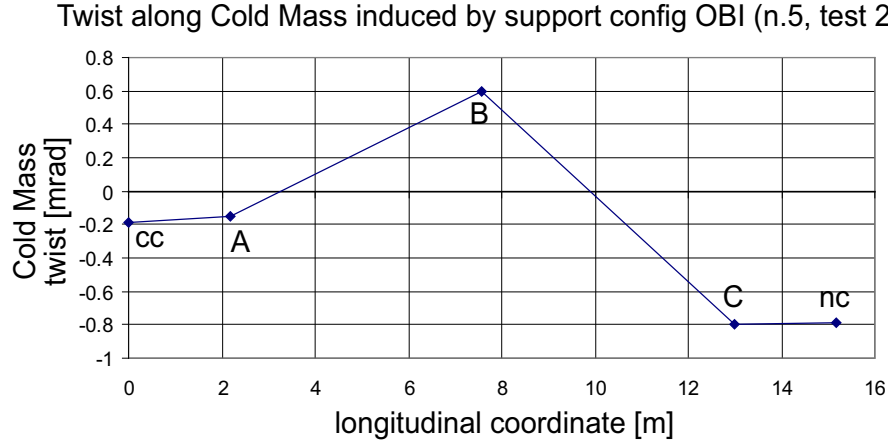


Figure 5.8: Twist along cold mass in the hypothesis of linear torsional behavior.

of the cold mass on horizontal bases solid with the shrinking cylinder. Also these instruments are affected by an intrinsic offset so that we operated as we did for the jig. Two types of inclinometers are used: ‘Type I’ and ‘Type II’ with a sensitivity of 0.01 and 0.05 mrad, respectively. In the second test, to overcome the digital inclinometer failure we used a level (air bubble type) with a sensitivity of 0.05 mrad and a working range limited to ± 0.8 mrad. To obtain the geometric plane direction w.r.t. gravity from the three measured sections we made the hypothesis of elastic linear response of the cold mass structure to torsion. In other words we assumed that the cold mass longitudinal twist induced by the rotation of two sections varies linearly between the two sections as visible in Fig. 5.8. Under this assumption the geometric plane orientation (α_{body}) is given by the average of the three section tilts (A, B and C in Fig. 5.8).

We carried out two measurement campaigns using two different kinds of bench supports. In the first test we used the standard cold mass supports used for CERN geometrical measurements. In the second we replaced the standard supports with more rigid ones in order to minimize their influence on the results.

5.3.3 Results

For each simulated misaligned configuration of the bench supports, we measured magnet twist in five sections along its length: at both the extremities (sections ‘CC’ and ‘NC’) by mean of the jig and at the support locations (sections A, B and C) using the inclinometers. The geometric plane angle was computed from the orientations of the three central sections and compared to its estimation given by the extremity average orientations. In Table 5.4 we give, for each configurations, the angles measured by the jigs at Connection side (jig CC) and at Non-Connection side (jig NC), the three angles measured in the three sections (A, B and C) along the cold mass, the geometric plane angle computed from the three sections (α_{body})

and the one computed from the end cover orientations (α_{ends}). The 3 letters in the ‘Code’ column gives the shim locations under the support A,B and C, respectively. Letters stand for None, In, Out and Both. In/Out mean the pad edge closer/farther w.r.t to the center of cold mass curvature. The subscripts indicate a shim thickness different from the default 3 mm. The values measured during the first tests are reported in the top part of Table 5.4. The poor reproducibility of the initial ‘flat’ position (‘NNN’) that we used as reference, was due to the bench supports who did not provide a sufficient stable and rigid surface. In spite of this feature, that we fixed in the second test (bottom part of the table), one can observe a small influence of the cold mass curvature as well as of its vertical flexion between the supports. The first is testified by the similarity of the twist induced by support configurations that are anti-symmetric with respect to the longitudinal cold mass axis, as ‘OIO’ and ‘IOI’. The second is testified by the similarity of the twist induced by support configurations that differ only in the shim thicknesses as for example ‘NIN’ and ‘NI₂N’.

It must be pointed out that the support rigidities do not influence the effectiveness of the test but complicates the estimation of the torsional stiffness because of the consequent indetermination of support reactions.

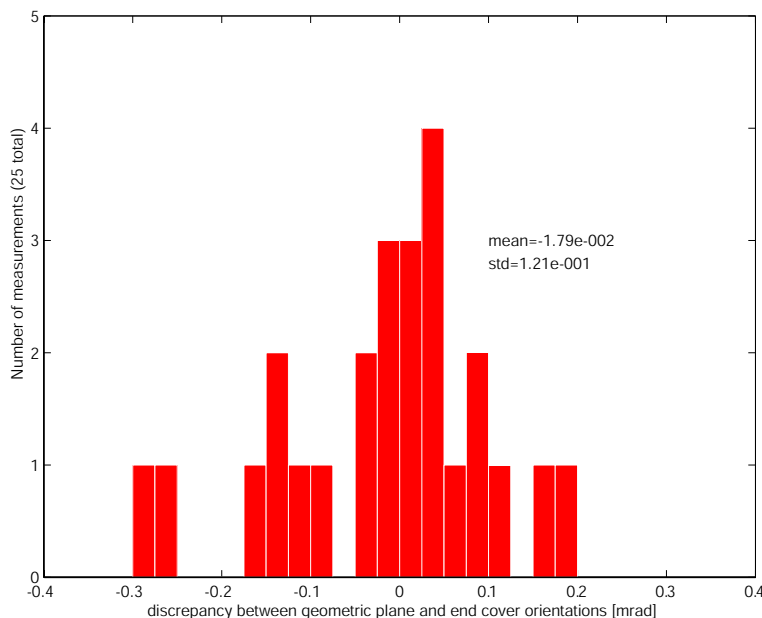


Figure 5.9: Distribution of errors associated to the geometrical plane evaluation based on end cover orientations.

The main test result is a statistical distribution, over all the possible support misalignments, of the error introduced by computing the geometric plane orientation through the magnet extremities. Using the jigs specifically developed to be used in the industries without affecting the standard set of geometric and mag-

Table 5.4: Data from test 1 (top) and 2 (bottom). See text for details.

Num.	Code	jig CC	Incl.II-A	Incl.I-B	Incl.II-C	jig NC	α_{body}	α_{ends}
0	NNN	0.00	0.00	0.00	0.00	0.00	0	0
1	NIN	1.55	1.40	1.66	1.25	1.43	1.20	1.12
2	OIO	-6.30	-6.25	-6.13	-6.25	-6.41	-6.19	-6.35
3	NNN	-0.15	-0.25	-0.24	-0.15	-0.27	-0.22	-0.21
4	NON	-1.56	-1.55	-1.83	-1.50	-1.55	-1.68	-1.55
5	IOI	6.53	6.20	6.06	6.20	6.33	6.13	6.43
6	NI ₂ N	1.12	1.10	1.35	1.00	1.12	1.49	1.49
7	NIO ₂	0.66	0.55	0.66	0.15	0.20	0.50	0.43
8	NI ₂ O ₂	0.00	0.10	0.05	-0.60	-0.60	-0.10	-0.30
9	O ₂ NO ₂	-6.98	-6.90	-6.84	-7.00	-7.04	-6.89	-7.01
10	O ₂ NN	-1.68	-1.70	-1.39	-1.20	-1.26	-1.42	-1.47
11	NO ₂ N	-1.18	-1.25	-1.52	-1.20	-1.29	-1.37	-1.23
12	NOI ₂	-0.78	-1.05	-1.24	-0.80	-0.88	-1.08	-0.83
13	NO ₂ I ₂	-0.22	-0.25	-0.34	0.05	0.07	-0.22	-0.07
14	I ₂ NI ₂	7.02	6.80	6.76	6.80	6.88	6.78	6.95
15	I ₂ NN	2.10	2.00	1.60	1.25	1.12	1.61	1.61
16	NNN	-0.09	-0.10	-0.12	-0.15	-0.14	-0.12	-0.11

Num.	Code	jig CC	Incl.I-A	Level-B	Incl.II-C	jig NC	α_{body}	α_{ends}
0	NNN	0.00	0.00	0.00	0.00	0.00	0	0
1	IBO	-0.92	-0.88	-0.40	0.00	0.01	-0.42	-0.45
2	IBI	-11.20	-11.21	-	-10.70	-11.23	-	-
3	OBI	-0.36	-0.32	-	-1.00	-0.94	-	-
4	OBO	10.06	10.09	-	9.85	10.15	-	-
5	OBI	-0.19	-0.15	0.60	-0.80	-0.79	-0.54	-0.43
6	ONI	0.38	0.46	-0.10	-0.30	-0.23	-0.01	0.07
7	ONO	10.35	10.42	-	10.05	10.44	-	-
8	INO	-0.46	-0.36	0.20	0.40	0.60	0.11	0.07
9	INN	-1.42	-1.33	-	-0.65	-0.68	-	-
10	NNN	-0.07	-0.04	0.00	-0.10	-0.07	-0.04	-0.07
11	NNI	-0.58	-0.57	-	-1.00	-1.05	-	-
12	NNN	-0.04	-0.02	-0.05	0.00	-0.02	-0.03	-0.03
13	NIN	-1.96	-1.99	-	-1.85	-1.93	-	-
14	NNN	-0.01	0.00	-0.10	0.00	-0.01	-0.05	-0.01
15	NON	0.86	0.82	-	0.70	0.84	-	-
16	NNN	0.00	-0.02	-	-0.05	-0.55	-	-
17	I ₂ NN	-1.39	-1.30	-	-0.70	-0.67	-	-
18	I ₁ NN	-1.29	-1.25	-	-0.70	-0.65	-	-
19	NNI ₂	-0.52	-0.50	-	-0.95	-0.94	-	-
20	NI ₁ N	-1.12	-1.30	-	-1.05	-1.08	-	-
21	NI ₂ N	-1.47	-1.49	-	-1.30	-1.42	-	-
22	NO ₂ N	0.67	0.65	-	0.60	0.67	-	-
23	NO ₁ N	0.55	0.53	0.80	0.45	0.53	0.63	0.54
24	NNI ₁	-0.46	-0.40	-0.80	-0.80	-0.89	-0.7	-0.67

netic measurements, we could estimate the plane orientation with an accuracy of $\pm 0.25 \text{ mrad}$ at 95 % confidence level. The error distribution is reported in the histogram of Fig. 5.9 and it must be pointed out that the largest errors are induced by exaggerated support misalignments, not allowed in the industries.

5.3.4 Evaluation of the cold mass torsional rigidity

Cold mass behavior to torsion can be considered, in first approximation, as the one resulting from two coaxial torsion bars loaded in parallel: one represents the external shrinking cylinder, the other represents the internal pack of iron yoke and steel collar laminations surrounding the superconducting Coil. The main unknown is the contribution of the internal part in which the lack of longitudinal continuity between laminations makes inconvenient an analytic approach.

Among the several test case measured the ones in which the system is statically determined can be used to estimate the cold mass stiffness to torsion. Such cases have no more than one shim per pad and are longitudinally anti-symmetric as cases number 2 and 5 of test 1 (Table 5.4).

With reference to case number 2 of test 1, shown in Fig. 5.6, we can assume that for symmetry reasons reactions $\|\mathbf{R}_A\|$ and $\|\mathbf{R}_C\|$ can be considered equal; if we then impose the equilibrium to rotation along a longitudinal axis we find that $\|\mathbf{R}_B\|$ must be equal to $\|\mathbf{R}_A\| + \|\mathbf{R}_C\|$. The implicit simplification is the neglecting of cold mass horizontal curvature and vertical deflection that could slightly change the reaction distributions.

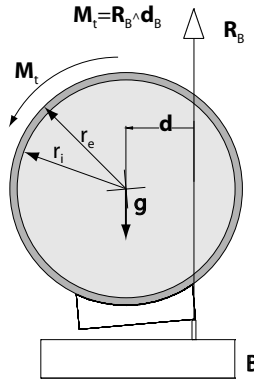


Figure 5.10: Magnet and support section by a transversal plane containing \mathbf{R}_B .

We then considered as the loading torque the vertical reaction of the constraint applied at a distance d from the center of mass as shown in Fig. 5.10. By measuring the rotation between two consecutive section we can deduce the global torsional stiffness from the equilibrium to rotation:

$$GI_p = \frac{M_t l}{\theta} \quad (5.1)$$

where: the global torsional stiffness GI_p is the product of the polar moment of inertia I_p of the circular section, times the global tangential stiffness G . The applied torque M_t is given by $R_b \cdot d$, θ is the measured relative angle and l is the distance between the sections. Once obtained the global torsional stiffness we can subtract the contribution of the shrinking cylinder (external cylinder) to find the stiffness of the internal part. We consider, in fact, the total torque be shared by the internal and the external cylinder so that $M_t = M_e + M_i$, hence:

$$M_t = \frac{G_e I_{pe} \theta}{l} + \frac{G_i I_{pi} \theta}{l} \quad (5.2)$$

where $I_{pe} = \frac{r_e^4 - r_i^4}{2} \pi$ and $I_{pi} = \frac{r_i^4}{2} \pi$ are the polar moments of inertia and G_e and G_i the tangential elasticity of the external and internal cylinder, respectively. Since the torsion θ and the distance l are the same for the two cylinders we can write:

$$G_i = \frac{GI_p - G_e I_{pe}}{I_{pi}} \quad (5.3)$$

and thus define an equivalent non-isotropic but continuous material to model the torsional behavior of the dipole internal structure made by packed laminations of iron and steel.

However it must be pointed out that the test was not specifically intended for the evaluation of cold mass torsional stiffness so that we had only two useful cases to observe: number 2 and 5 of test 1 (Table 5.4). From these cases, we got a total of 4 relative torsions between consecutive cold mass sections condensed in a range from 0.12 to 0.14 mrad. The corresponding torsional rigidity, given by equation 5.1 is enclosed between 0.355 and 0.438 GPa m⁴. As already mentioned, this simple model does not take into account the cold mass curvature and the flexion due to its self weight. Through the comparison with a 3D finite element model we found that the curvature influence is negligible whereas the flexion, related to the specific support configuration, increases the equivalent torsional rigidity by 6 % so that the corrected values are 0.334 and 0.410 GPa m⁴. These values can be compared to the torsional rigidity of the shrinking cylinder itself that is 0.106 GPa m⁴ and to the one of a continuous homogenous cylinder with the same cold mass dimensions that is 0.797 GPa m⁴. Equation 5.3 gives us the tangential elasticity of an equivalent homogenous material to model the behavior to torsion of the packed iron and steel laminations: 24 GPa versus a steel value of 77 GPa.

5.4 Summary

Magnet shape and the precise geometrical specifications make the tolerance checks themselves a challenge that must be approached using laser trackers and multi-station measurements. In spite of the smart approach to improve the measurement

accuracies a noisy saw-toothed signal is, to some extent, always present. To find potential noise sources the measuring procedure and the measuring instrument features have been investigated in detail. The statistical analysis of three set of measurements taken by different operators pointed out the critical definition of a unique reference system in each multi-station measurement so far carried out. To estimate the best accuracy achievable in a multi-station measurement, a Montecarlo based numerical simulation has been implemented. The simulation goal was to reproduce the propagation of the error introduced by the laser tracker accuracy through-out the whole procedure. The partial agreement between simulation and measurements pointed out the presence of an additional source of error not rooted in the ideal measuring procedure. A potential cause was identified in small laser tracker displacements due to the interaction with the ground as already experienced by some operators during measurements. The implementation of this feature in the simulation thus provided a full agreement with the experimental data.

The suggested corrective action is the check of tracker stability in every station before the measurement. In this way it is possible to minimize the saw-tooth effect down to the intrinsic limit of the multi-station procedure determined by machine precision and network point dispositions.

The second topic presented in this chapter was the accuracy related to evaluation of the main field direction. We described a procedure to relate the main field direction, measured on the magnetic test bench, to the geometric plane, measured on the geometric test bench. The procedure relies on the measurement of cold mass extremities on both the benches by mean of two specifically developed tilt-meters: the basic concept is, in fact, to evaluate the geometric plane direction through the extremity orientations. As the procedure accuracy could be undermined by a twist of the cold mass due to the misalignment of the supports in the test benches, we tested the procedure on a bench with strongly misaligned supports. The test results indicate that the geometric plane can be identified through the end cover orientations with an accuracy that is ± 0.25 mrad at 95 % confidence level. Facing a tolerance range of ± 1 mrad on the angle between the main field and the geometric plane directions, the procedure can be considered suitable. We can thus give a overview of the procedure steps to be implemented in the industries:

- 1) installation of cold mass on the magnetic test bench
- 2) measurement of the main field direction with respect to gravity performed with the standard tool for the magnetic measurements,
- 3) measurement, without displacing the cold mass, of extremity orientations with respect to gravity using the jigs specifically developed at CERN and provided to the industries,
- 4) installation of cold mass on the geometric test bench,

- 5) measurement of the geometric plane direction with respect to gravity performed with the standard tool for the geometric measurements,
- 6) measurement, without displacing the cold mass, of extremity orientations with respect to gravity using the jigs,
- 7) evaluation of main field direction with respect to geometric plane through the extremity orientations.

A secondary outcome of this study is a first approximation evaluation of the cold mass torsional stiffness; it is, in fact, based on only four observations. The estimated mean value is 0.372 GPa m^4 that corresponds to 3.5 times the torsional stiffness of the steel shrinking cylinder itself and to 0.48 times the value of a solid cold mass made of steel. The corresponding value of the tangential elasticity of an equivalent material to model the torsional behavior of the collar and yoke packed laminations is 24 GPa .

Part III

ANALYSIS OF PRE-OPERATIVE AND OPERATIVE PHASES

Chapter 6

Geometrical susceptibility in pre-operative stages.

6.1 Introduction

In this chapter we investigate the circumstances that can affect the cold mass geometry between the manufacturing and the operative phases. Of primary importance is to understand how to be hosted in the cryostat can influence cold mass geometry. We describe therefore the experience we made to understand the behavior of the sliding interface between the cryostat and the cold mass. In the second part we analyze the performance of different types of transport restraints designed to minimize the cryostat/cold mass relative displacements during transport and handling.

6.2 Mechanical interference between the dipole and the cryostat.

During thermal cycles the contraction of the cold mass will induce a change of shape in each dipole and an interference between the extremities of two adjacent dipoles. Should these phenomena induce an uncontrolled modification of the dipole shape, we will have to face two detrimental consequences: the aperture available for the LHC beam will be reduced and the transverse position of the multipolar correctors will be shifted away from the closed orbit. Since it will be rather difficult to observe this in operative conditions, we studied the effect of external forces applied to the dipole ends. The effect of these forces on cold mass geometry is substantially determined by the behavior of the cold mass/cryostat sliding interfaces. They represent the constraints on the cold mass/cryostat relative displacement and are designed to allow cold mass homothetic shrinkage. The interface features a non linear behavior, related to the coulombian friction between the Fe430 PTFE coated base and the GFRE support column. Laboratory test evaluated a static friction coefficient of

0.08 [29] but it has never been verified in an assembled cryo-dipole. Hence we worked out a dedicated test in a pre-series cryo-dipole to observe the cold mass response to mechanical loads when installed in the cryostat. The test was performed at room temperature and the results compared to FEM simulations.

6.2.1 Test set-up

The mechanical interference between dipole ends induced by thermal cycles is reproduced in the test as a transverse load applied on the dipole end covers. The load is applied in the horizontal plane perpendicularly to dipole axis and is generated by mean of an hydraulic actuator fixed to the cryostat. In the schematic cryo-dipole top view of Fig. 6.1 we show the applied force location and the cold mass degrees of freedom allowed by support interfaces. The cold mass extremity displacement with respect to the cryostat is monitored by an interferometric device ('SOFO' see Chapter 7.2 for details). Axis deformations are measured with 3D laser tracker before, during and after the application of the loads. The laser tracker, used in conjunction with a special reflector traveling in one of the magnet apertures, provides the whole axis tri-dimensional shape. We used the complete axis profile for detailed comparison with the finite element model reproducing the cold mass subjected to the same loads and constraints.

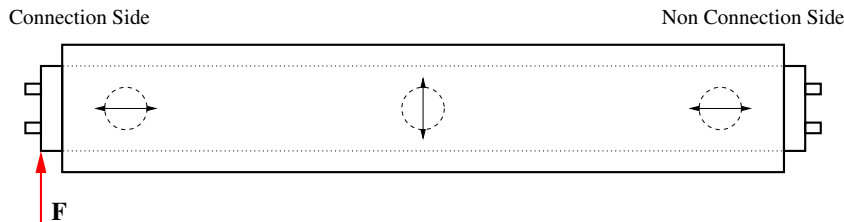


Figure 6.1: Cryo-dipole top view. Applied force and allowed sliding directions in the cold mass/cryostat interfaces are shown.

6.2.2 Test result

During the first load cycle, to confirm the cryostat steadiness assumption and, if necessary, to correct the measurements, the laser tracker was used in conjunction with centesimal comparators and interferometric device providing the cryostat distances from external fixed points and from the cold mass. The described set-up is shown in Fig 6.2. By mean of the actuator we applied and removed an increasing load up to reach a 2mm horizontal displacement with respect to the cryostat, as measured by the interferometer.

In the plot of Fig. 6.3 we give the displacement of cold mass extremity with respect to the cryostat, measured by the interferometric device visible in Fig. 6.2,

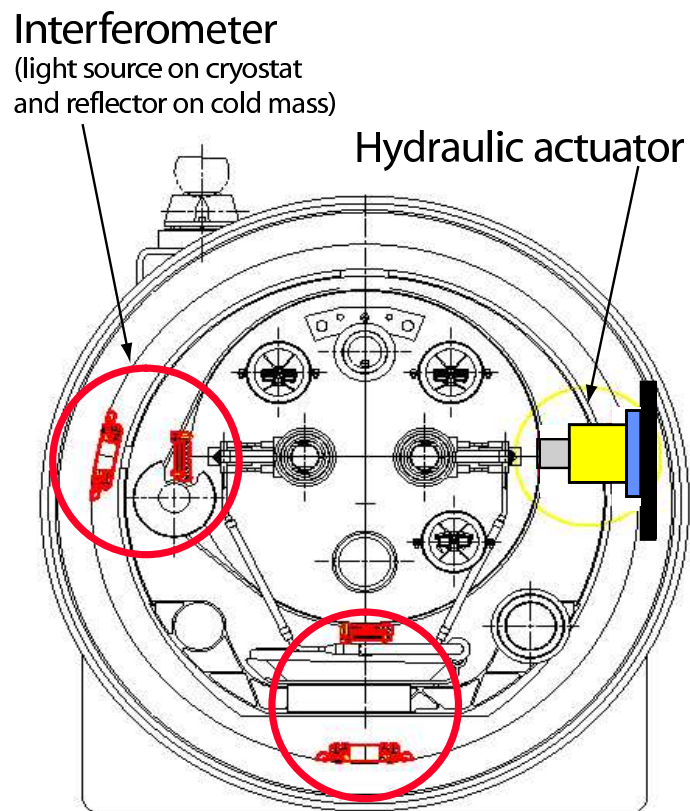


Figure 6.2: Schematic of test set-up.

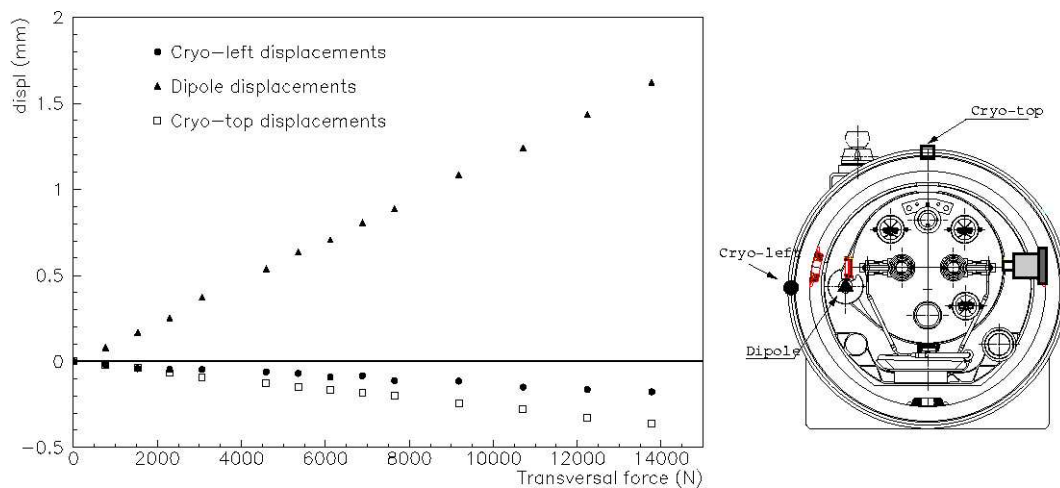


Figure 6.3: Force-displacement relation in a transversal plane at cold mass extremity. Laser tracker data.

and the displacements of two fiducials on the cryostat, shown in the drawing of Fig. 6.3, versus the applied force. The values, given with respect to the starting position and positive leftward, show a non negligible ovalization of the cryostat that must be taken in to account to correct the cold mass displacements measured by the interferometer.

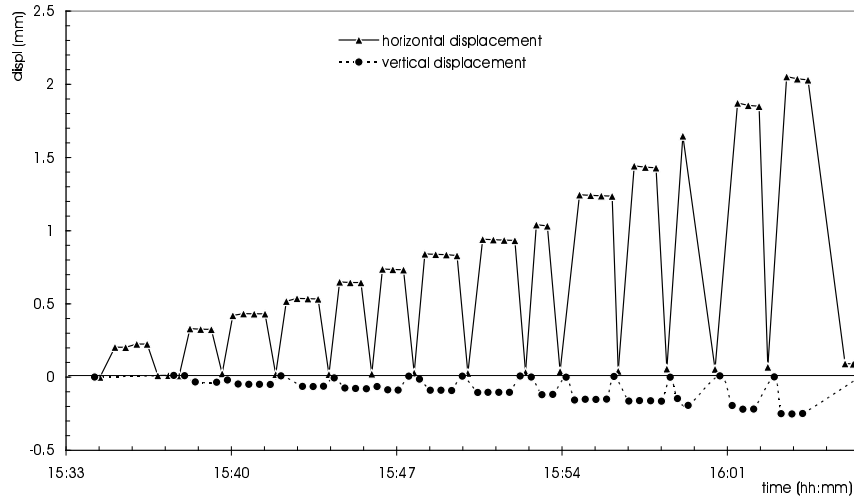


Figure 6.4: Horizontal and vertical displacement of loaded end. Interferometer data.

In Fig. 6.4 we plot the horizontal and vertical displacement of the cold mass measured by the interferometer. It can be seen that, after the removal of each load, the cold mass regains its position both in vertical and in horizontal directions within hundredths of millimeter.

In Fig. 6.5 the load F is plotted versus the horizontal displacement d , corrected from cryostat deformation. As the force-displacement relation is clearly linear we defined an elastic coefficient given by the slope of the curve that is $8.8 \pm 0.3 \text{ kN/mm}$ (with a 95 % confidence level).

Then, to study the change of the whole cold mass geometry, we applied the same loads and we measured the horizontal displacement d all along the cold mass axis during and after each load. In the plot of Fig. 6.6, lines represent axis deformations measured under the loads and markers after the load (almost coincident with the abscissae axis); black arrows indicate the longitudinal locations of the supports. We can see that the axis shapes measured after the removal of each load (markers: 0-3.8 kN, 0-7.7 kN and 0-15.4 kN) fully overlap so that we can exclude any permanent residual displacement.

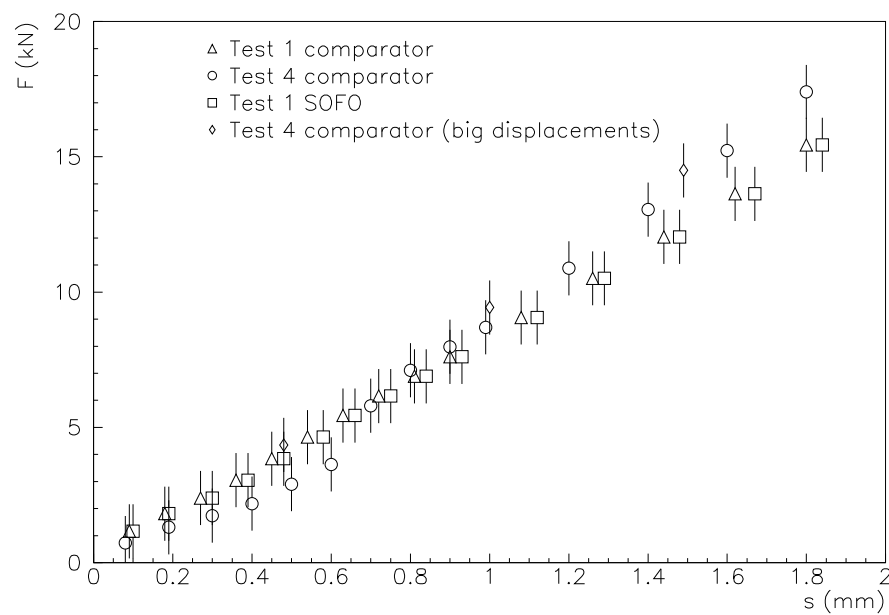


Figure 6.5: Loaded end horizontal displacement vs. applied load.

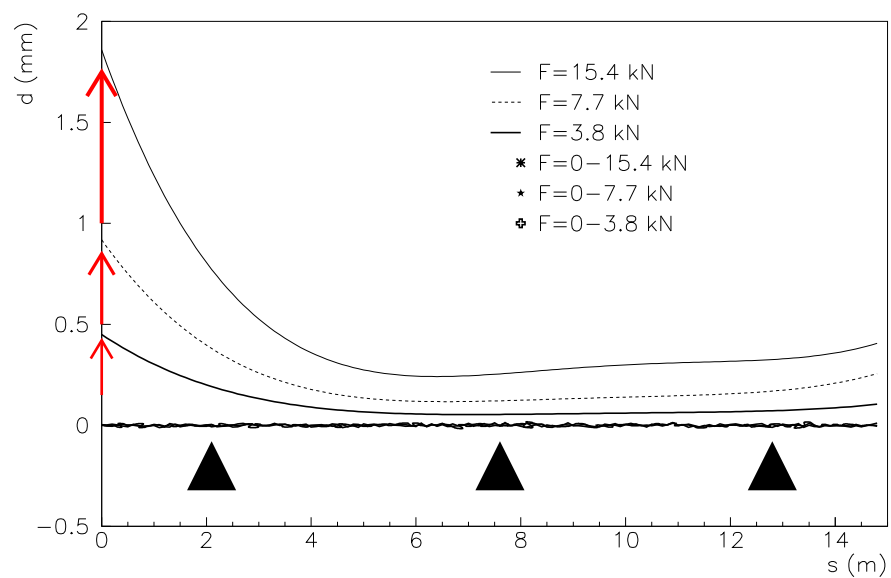


Figure 6.6: Axis shape in the horizontal plane under load and rest conditions. Arrows indicate support positions.

6.2.3 Model description

The finite element model is fundamentally the one described in Paragraph 3.3 apart from the cryostat that was assumed to be rigid and stable and hence ignored. The restraints were applied to the support post bases so that the two supports closer to dipole ends are allowed to slide longitudinally and are blocked transversally, whilst the central support is constrained in the longitudinal direction and can slide in transversal direction (Fig. 6.1). Consequently the central support is the only one that influences the Cold mass response to transversal loads. To investigate the role of friction in the central support sliding interface we decided to compare the experimental data to two FEM models. One model has the central post blocked also in transversal direction and represents the cold mass deformation in case that the friction coefficient is high enough to prevent the central post from sliding. The other model has the central post free to slide transversally without friction and gives an estimation of the cold mass deformation in case that the friction coefficient is insufficient to prevent the central post from sliding.

Some minor variations in the model concern the material properties used. They reflect in fact the design specification of the early production stage and are listed in Table 6.1.

Table 6.1: Elasticity of materials used in the FEM .

Component	Material	Young's modulus [MPa]	
		Longit.	Transv.
Shrinking cylinder	St. steel	$2 \cdot 10^5$	$2 \cdot 10^5$
Yoke	Iron	$6.6 \cdot 10^3$	$2 \cdot 10^5$
Collar	St. steel	$6.6 \cdot 10^3$	$2 \cdot 10^5$
Supports	GFRE	$17.3 \cdot 10^3$	$17.3 \cdot 10^3$

6.2.4 Measurements and simulation comparison

In the top graph of Fig 6.7 we show the horizontal deformation of the dipole axis corresponding to a load of about 15.4 kN. The narrow dotted line gives the measured value, the solid line represents the result of a simulation with frictionless sliding supports and the dashed line shows the result of a simulation where the central support is blocked. The model with frictionless sliding post predicts a large deformation of the dipole shape, which should exhibit a large curvature and a considerable negative shift at the position of the central post (in the opposite direction with respect to the applied force). Instead, the dipole axis, as measured by the laser tracker during the test, does not show such a shape. The observed curvature is drastically smaller and

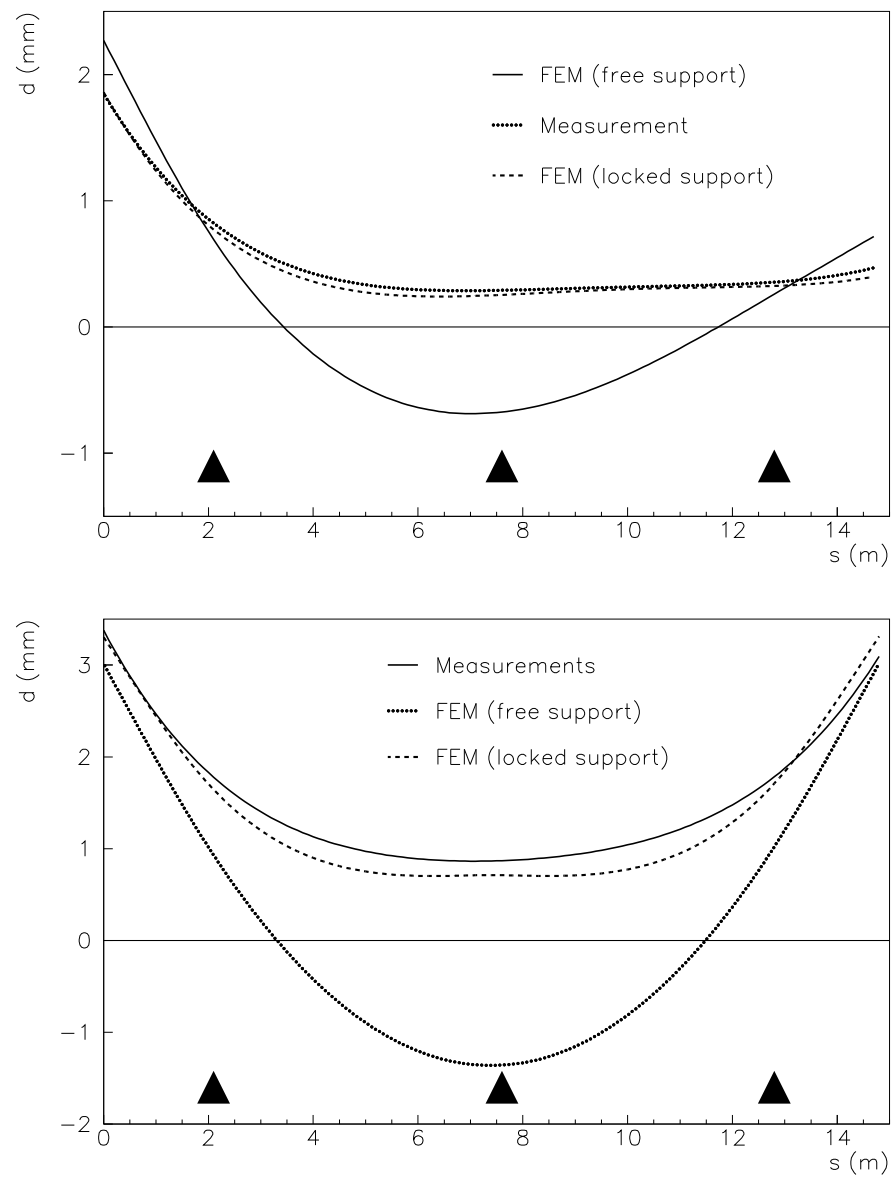


Figure 6.7: Measured and simulated axis deflections in horizontal plane for an applied force of 15.4 kN at one extremity (top) and ~ 23 kN at both the extremities.

the deformation at the location of the central post is positive. The FEM model with the central support fully blocked gives results in excellent agreement with the experimental data. We can therefore conclude that the friction prevented the support sliding and estimate the lower limit of the friction coefficient. The friction coefficient must be, in fact, equal or greater than the transverse over normal force ratio in the support interface. From the model we get 5.5 kN over 105 kN that results in a minimum friction coefficient of 0.053. Such a value is consistent with expected value of 0.08.

In a second test, we loaded both the cold mass ends with transversal forces of about 23 kN per side. The results are shown in the bottom graph of Fig. 6.7. Through the comparison of experimental results (dotted line) with the finite element model (solid line for frictionless support interface and dashed line for locked support interface), it can be argued that no transversal sliding of the central support occurs even in this case. The model provides an estimate of the resulting transversal force applied on the central support of about 17 kN. This corresponds to a friction coefficient be equal or greater than 0.16, i.e. by far in excess of the above mentioned expected value of 0.08. On-going investigations should clarify why the sliding interface of the central support is so sticky and suggest possible remedies.

6.3 Cryo-dipole transport, handling and stocking.

The transport and the handling necessary to transport the cryo-dipole from the cryostating facility down in to the tunnel, along with the prolonged outdoor stocking, could have harmful consequences on magnet shape and on the integrity of some critical components. Careful analyses have been performed on the effect of dynamic loads on the cryo-dipole [30], [31], [32] to define the transport specifications [33]; however the considerable mass and small rigidity of the magnet could turn into critical the effects of static inertial loads. Such loads are induced for example during up-lifting and down-lifting of the magnet by a crane or during braking or turning of the truck used for road transport; their effect on magnet integrity has not been studied yet. To validate the transport specifications given in Table 6.2 we will study the loads induced by the maximum admissible accelerations considering different transport restraints. We will focus on the stresses induced in the composite supports and in the cold mass. We will also present the effect of differential thermal contraction induced by a ± 30 K temperature difference between the cryostat and the cold mass as expected during outdoor storage.

Table 6.2: Maximum allowed accelerations during transport.

	Longitudinal (Y)	Lateral (X)	Vertical (Z)
Acceleration (m/s^2)	4	5	7

6.3.1 Transport specifications

From the structural point of view the most critical components of the cryo-dipole are represented by the composite material columns supporting the 30 t cold mass inside the cryostat. The support composite material, chosen for the good balance between thermal conductivity and structural properties [34], is a Graphite Fiber Reinforced with Epoxy (GFRE) and it showed a good resistance to mechanical tests [35], [15]. However during transport, to relief stresses in the composite supports, it is safe to minimize relative displacements between the cold mass and the cryostat. The cryo-dipole design allows the installation of additional cold mass/cryostat restraints only at its extremities, hence the need to develop specific apparatus as described in [36], [37], [38], [39], and shown in Fig 6.8 (from now on: ‘nominal transport restraint’).

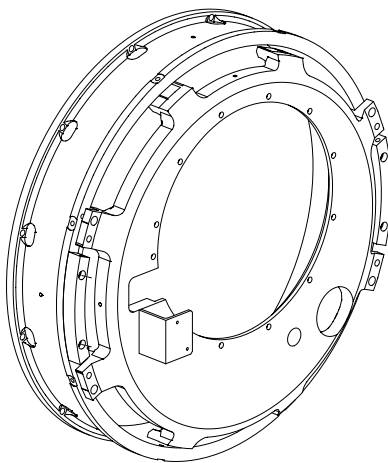


Figure 6.8: Nominal transport restraint.

Facing production delay problems affecting the nominal transport restraints, we want to investigate the feasibility of an alternative solution based on the use of much simpler components as the temporary restraints used for indoor cryo-dipole moving. This component (from now on: ‘light restraint’) is shown in Fig. 6.9 and is made of three plates: the front plate hosts the bolts connecting to the cold mass, the back plate hosts the bolts connecting to the cryostat and the central plate connects the back to the front plate. Two triangles are designed to reinforce the connection between the central and the front plate. The remarkable size difference between the light and the nominal restraint is shown in the drawing of Fig. 6.10. The presence of holes close to the edges requires a detailed analysis of stress distribution that we carried out using finite element method taking also into account stresses arising inside the screws. Another possible solution that we studied is represented by the Cremonian type restraint (a structure made of beams) shown in Fig. 6.11.

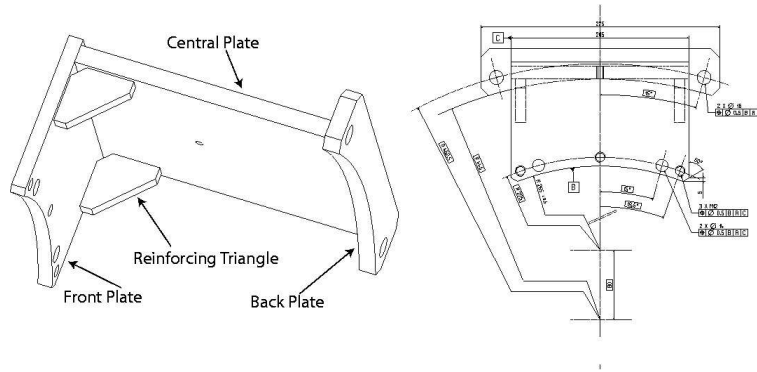


Figure 6.9: Light transport restraint.

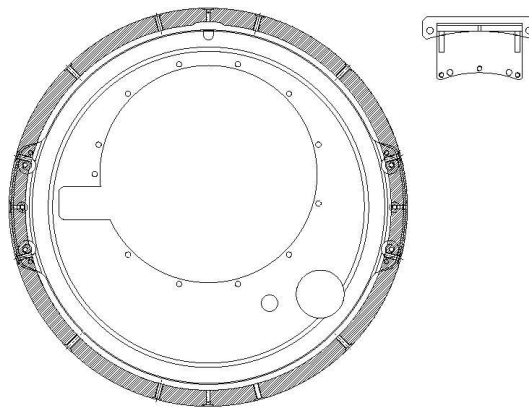


Figure 6.10: Front view of nominal and light transport restraints.

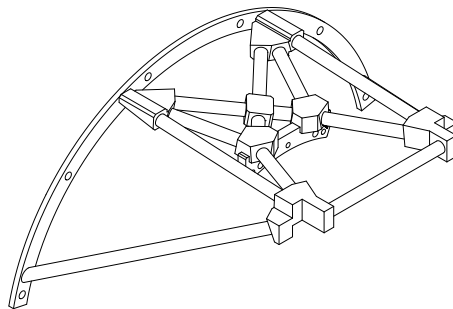


Figure 6.11: Cremonian type transport restraint.

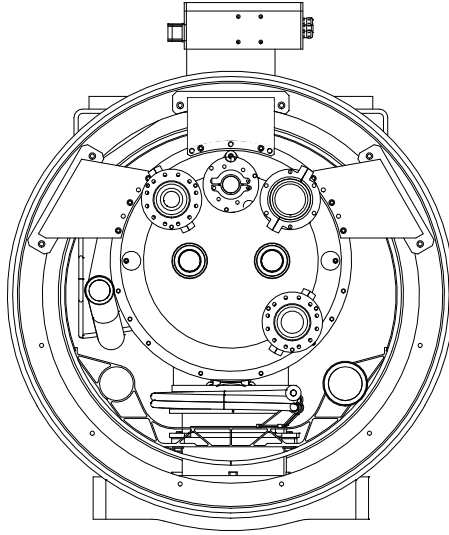


Figure 6.12: Transport configuration with three light restraints.

6.3.2 The finite element model

The finite element model of the light transport restraint is shown in Fig. 6.13; material properties are given in Chapter 3.3. The finite element software used is ANSYSTM and the elements are BRICK45 for the restraint body and different type of beams for the screws. Out of the seven screws we decided to model only the five interfacing the restraint with the cold mass extremity as they are thinner and potentially subjected to bending. As shown in the top-right of Fig. 6.13 the solid element mesh is denser around the holes where the stresses concentrate. The five screws interface design presents two bolts engaged in the cold mass and three headless set screws engaged in the threaded holes of the transport restraint (Fig. 6.9). Once mounted, the restraint front plate and the cold mass extremity are not in close contact; this is necessary to take up slightly different relative positions, from magnet to magnet, between cold mass and cryostat. The consequent gap is bridged by the five screws that can thus be subjected to bending. The bending stress increases the tension stress in the bolts and the compression stress in the set screws. To implement this features in the FEM model we used element LINK10 (only compression/tension truss) in conjunction with BEAM4 (to take into account the bending). The connection between the beam representing the screw body and the hole on the restraint is implemented differently for the headless set screws and for the bolts. A detailed description of the screw modelization is given in Appendix F.

To test the alternative restraint solutions we modeled different designs and we used the stiffest one, composed of a net of beams connecting the cold mass and the cryostat, as shown in Fig. 6.13, as target in the performance comparisons. We tested the following transport restraint configurations:

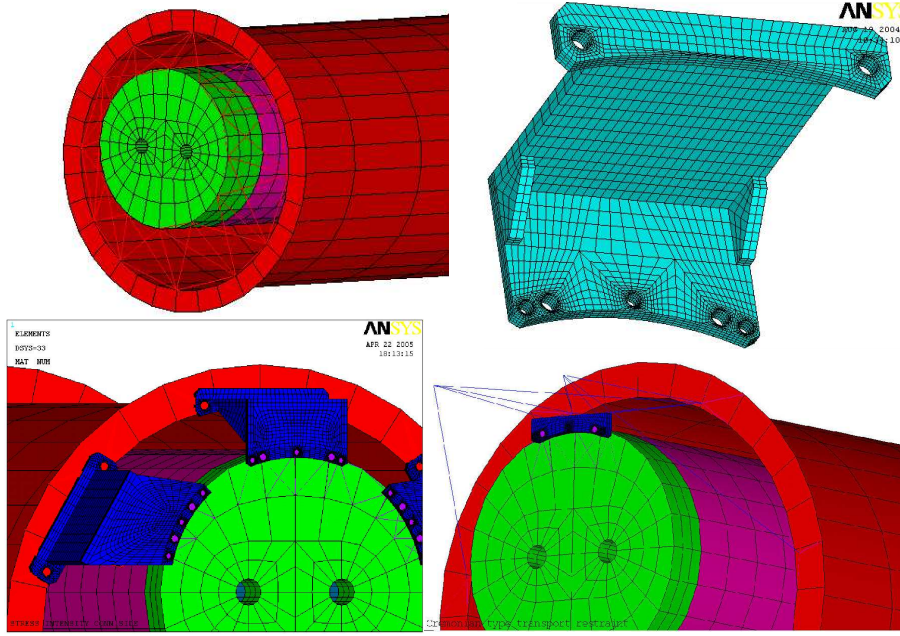


Figure 6.13: Clockwise from top left: very rigid transport restraint composed of a net of beams, light transport restraint, three light transport restraints configuration, Cremonian type transport restraint.

- one light restraint per side
- three light restraints per side
- three modified light restraints per side
- one Cremonian type restraint per side

All the finite element models are shown in Fig 6.13. The modification of the light restraint consists in an enlargement of the triangles connecting the horizontal and vertical plates (compare top-right and bottom-left of Fig 6.13). Specifications of cryo-dipole finite element model are given in Chapter 3.3. The central GFRE support is solid with the cryostat whereas the sliding interfaces between the other two composite supports and the cryostat have been implemented with two different friction coefficients, zero and infinite, in order to respectively recreate the worst and the best possible occurrences for the transport restraints. The cryostat is fixed to the ground through the bottom of the three cradles. The applied loads are represented by the maximum allowable accelerations during surface transport, as stated in [33] and reported in Table 6.2, and by a 30 K temperature difference between cryostat and cold mass.

6.3.3 Results

The analysis results we are mainly interested in are:

- the loads on the central support,
- the stress distribution inside the restraints,
- the cold mass/cryostat relative displacement.

It must be noticed that when the restraints are mounted on the cryo-dipole the gravity is already deforming the cold mass ideal shape in the vertical plane. In the first phases of our study, to evaluate the effect of this initial condition, we performed the analysis in successive steps: application of the gravity first, application of the restraints and then application of the additional inertial loads. We found a linear response of the system so that in the radial and longitudinal directions the support reactions were not influenced by the gravity whereas in the vertical direction they corresponded to the sum of the loads due to gravity and to acceleration. Therefore, to save computing time, in the successive analyses we did not apply the gravity so that an implicit vertical force of -105 kN for the central and -80 kN for the two lateral supports must be added to the results.

We give now the analysis results concerning the three following designs: the three light restraints ('3LR') the three modified light restraints ('3Mod LR') and the Cremonian type compared with the ideal one and grouped by load. We take into account the worst case of negligible friction between support posts and cryostat, except for the central one that is blocked. The concentrated forces and bending moments resulting on a support are computed as the sum of all the nodal forces at the bottom of the support and the moments are referred to the center of the column base. For the transport restraints we considered the forces acting on the cryostat flange and the moments are referred to the flange center; longitudinal forces are positive when pushing inward with respect to cryostat, radial forces have opposite positive directions at Connection and at Non-Connection side (toward center of curvature at Connection side), vertical forces are positive upward. The reference system Y-axis matches the cryostat axis from Non-Connection to Connection side, the Z-axis is opposite to gravity direction and the X-axis is consequently directed outward w.r.t. ring center.

Screw results are represented by the sum of the maximum longitudinal stresses induced by the normal load and by the bending; results concern the radial acceleration load for the three modified transport restraints design since it represents the most critical occurrence for the preferred option. We go now through the detailed results for the different load cases.

Table 6.3 lists the loads on the supports and on the transport restraints induced by a longitudinal acceleration of 4 m/s^2 . As the extremity supports ('Non-Connection' and 'Connection') are free to slide longitudinally, the total load of

~ 110 kN is transferred to the central support and to the transport restraints. The longitudinal force acting on the central support strongly depends on the transport restraint longitudinal stiffness. It can be noticed that the light modified and the Cremonian reduce the force to one half with respect to the light ones so that the value stays below the critical value of 40 kN (considered an acceptable safety limit [40]). The longitudinal acceleration induces a pitch of the cold mass that compresses the Non-Connection support and stretches the Connection support by a force of 3 to 4 kN depending on the restraint type. These values, negative for compression and positive for stretching, must be algebraically added to the -85 kN due to cold mass weight.

Table 6.3: Sum of forces on support bases and transport restraints induced by a 4 m/s² longitudinal acceleration.

$a_y = 4 \text{ m/s}^2$	Forces [N]	3LR	3 Mod LR	Cremonian	Ideal
Support bases					
Non-Connection	$\sum F_x$	$-2.46 \cdot 10^1$	$-5.35 \cdot 10^1$	$-8.70 \cdot 10^0$	$2.94 \cdot 10^2$
	$\sum F_y$	$1.88 \cdot 10^1$	$1.89 \cdot 10^1$	$1.88 \cdot 10^1$	$1.80 \cdot 10^1$
	$\sum F_z$	$-4.22 \cdot 10^3$	$-3.89 \cdot 10^3$	$-2.72 \cdot 10^3$	$-3.35 \cdot 10^3$
Central	$\sum F_x$	$-3.06 \cdot 10^2$	$-2.84 \cdot 10^2$	$-3.11 \cdot 10^2$	$-2.37 \cdot 10^2$
	$\sum F_y$	$-6.03 \cdot 10^4$	$-3.53 \cdot 10^4$	$-3.48 \cdot 10^4$	$-8.40 \cdot 10^3$
	$\sum F_z$	$1.93 \cdot 10^1$	$-2.67 \cdot 10^{-1}$	$-8.52 \cdot 10^{-2}$	$8.23 \cdot 10^{-1}$
Connection	$\sum F_x$	$-7.18 \cdot 10^1$	$-9.03 \cdot 10^1$	$-5.33 \cdot 10^1$	$-5.66 \cdot 10^2$
	$\sum F_y$	$1.90 \cdot 10^1$	$1.90 \cdot 10^1$	$1.89 \cdot 10^1$	$2.03 \cdot 10^1$
	$\sum F_z$	$4.21 \cdot 10^3$	$3.89 \cdot 10^3$	$2.72 \cdot 10^3$	$3.35 \cdot 10^3$
Transport restraints					
Non-Connection	$\sum F_x$	$-1.14 \cdot 10^2$	$-1.17 \cdot 10^2$	$-1.40 \cdot 10^2$	$-4.86 \cdot 10^2$
	$\sum F_y$	$-2.52 \cdot 10^4$	$-3.89 \cdot 10^4$	$-3.77 \cdot 10^4$	$-5.08 \cdot 10^4$
	$\sum F_z$	$1.96 \cdot 10^3$	$2.75 \cdot 10^3$	$2.33 \cdot 10^3$	$2.43 \cdot 10^3$
Connection	$\sum F_x$	$6.80 \cdot 10^1$	$4.98 \cdot 10^1$	$6.60 \cdot 10^1$	$4.16 \cdot 10^2$
	$\sum F_y$	$-2.55 \cdot 10^4$	$-3.89 \cdot 10^4$	$-3.77 \cdot 10^4$	$-5.08 \cdot 10^4$
	$\sum F_z$	$-1.97 \cdot 10^3$	$-2.75 \cdot 10^3$	$-2.33 \cdot 10^3$	$-2.43 \cdot 10^3$

Table 6.4 lists the forces induced by a transversal acceleration of 5 m/s² corresponding to a 10 m-radius turn when the transport truck travels at 25 km/h. This time the total load of ~ 140 kN is shared by all the three supports and by the transport restraints. In all the cases, ideal included, the transversal force loading the central support is higher than the 40 kN safety limit. It can be noticed the high transversal stiffness of the Cremonian type restraint that decreases the load from the extremity supports but increases the one on the central. When comparing the light restraint to the modified ones it can be noticed that the extremity supports get a smaller transversal force with the non modified restraints.

Table 6.4: Sum of forces on support bases and transport restraints induced by a 5 m/s² lateral acceleration and by a 7 m/s² vertical acceleration.

$a_x = 5 \text{ m/s}^2$	Forces [N]	3 LR	3 Mod LR	Cremonian	Ideal
Support bases					
Non-Connection	$\sum F_x$	$-1.97 \cdot 10^4$	$-2.30 \cdot 10^4$	$-1.14 \cdot 10^4$	$-3.35 \cdot 10^4$
	$\sum F_y$	$5.19 \cdot 10^1$	$6.06 \cdot 10^1$	$3.02 \cdot 10^1$	$8.82 \cdot 10^1$
	$\sum F_z$	$-8.75 \cdot 10^0$	$-8.97 \cdot 10^0$	$-1.36 \cdot 10^1$	$-1.41 \cdot 10^2$
Central	$\sum F_x$	$-6.47 \cdot 10^4$	$-6.21 \cdot 10^4$	$-6.98 \cdot 10^4$	$-5.53 \cdot 10^4$
	$\sum F_y$	$-5.61 \cdot 10^1$	$-3.59 \cdot 10^1$	$-1.81 \cdot 10^1$	$-4.19 \cdot 10^0$
	$\sum F_z$	$4.04 \cdot 10^1$	$2.49 \cdot 10^1$	$6.20 \cdot 10^1$	$1.86 \cdot 10^2$
Connection	$\sum F_x$	$-1.97 \cdot 10^4$	$-2.30 \cdot 10^4$	$-1.14 \cdot 10^4$	$-3.35 \cdot 10^4$
	$\sum F_y$	$5.19 \cdot 10^1$	$6.06 \cdot 10^1$	$3.02 \cdot 10^1$	$8.82 \cdot 10^1$
	$\sum F_z$	$2.31 \cdot 10^1$	$2.72 \cdot 10^1$	$1.41 \cdot 10^0$	$9.62 \cdot 10^1$
Transport restraints					
Non-Connection	$\sum F_x$	$1.73 \cdot 10^4$	$2.04 \cdot 10^4$	$2.25 \cdot 10^4$	$7.78 \cdot 10^3$
	$\sum F_y$	$6.07 \cdot 10^1$	$1.83 \cdot 10^2$	$2.14 \cdot 10^2$	$2.10 \cdot 10^3$
	$\sum F_z$	$1.41 \cdot 10^1$	$5.15 \cdot 10^0$	$1.76 \cdot 10^1$	$4.58 \cdot 10^1$
Connection	$\sum F_x$	$1.73 \cdot 10^4$	$2.04 \cdot 10^4$	$2.25 \cdot 10^4$	$7.78 \cdot 10^3$
	$\sum F_y$	$-1.29 \cdot 10^1$	$-9.75 \cdot 10^1$	$-1.71 \cdot 10^2$	$-1.93 \cdot 10^3$
	$\sum F_z$	$4.07 \cdot 10^1$	$3.79 \cdot 10^1$	$3.22 \cdot 10^1$	$5.30 \cdot 10^0$

$a_z = 7 \text{ m/s}^2$	Forces [N]	3 LR	3 Mod LR	Cremonian	Ideal
Support bases					
Non-Connection	$\sum F_x$	$1.42 \cdot 10^1$	$1.37 \cdot 10^1$	$1.81 \cdot 10^1$	$-5.35 \cdot 10^1$
	$\sum F_y$	$-3.73 \cdot 10^{-2}$	$-3.61 \cdot 10^{-2}$	$-4.77 \cdot 10^{-2}$	$1.41 \cdot 10^{-1}$
	$\sum F_z$	$-5.57 \cdot 10^4$	$-5.57 \cdot 10^4$	$-5.69 \cdot 10^4$	$-5.45 \cdot 10^4$
Central	$\sum F_x$	$-9.71 \cdot 10^0$	$-9.07 \cdot 10^0$	$-1.17 \cdot 10^1$	$2.64 \cdot 10^1$
	$\sum F_y$	$6.50 \text{E} \cdot 10^{-1}$	$9.95 \cdot 10^{-1}$	$9.46 \cdot 10^{-1}$	$1.53 \cdot 10^0$
	$\sum F_z$	$-7.58 \cdot 10^4$	$-7.58 \cdot 10^4$	$-7.50 \cdot 10^4$	$-7.62 \cdot 10^4$
Connection	$\sum F_x$	$1.32 \cdot 10^1$	$1.28 \cdot 10^1$	$1.70 \cdot 10^1$	$-5.64 \cdot 10^1$
	$\sum F_y$	$-3.48 \cdot 10^{-2}$	$-3.37 \cdot 10^{-2}$	$-4.49 \cdot 10^{-2}$	$1.48 \cdot 10^{-1}$
	$\sum F_z$	$-5.57 \cdot 10^4$	$-5.57 \cdot 10^4$	$-5.69 \cdot 10^4$	$-5.45 \cdot 10^4$
Transport restraints					
Non-Connection	$\sum F_x$	$-9.16 \cdot 10^0$	$-9.03 \cdot 10^0$	$1.21 \cdot 10^1$	$4.07 \cdot 10^1$
	$\sum F_y$	$-1.50 \cdot 10^2$	$-2.37 \cdot 10^2$	$3.26 \cdot 10^2$	$1.71 \cdot 10^3$
	$\sum F_z$	$-3.41 \cdot 10^3$	$-3.67 \cdot 10^3$	$1.99 \cdot 10^3$	$-3.62 \cdot 10^3$
Connection	$\sum F_x$	$-8.53 \cdot 10^0$	$-8.41 \cdot 10^0$	$1.14 \cdot 10^1$	$4.28 \cdot 10^1$
	$\sum F_y$	$1.49 \cdot 10^2$	$2.37 \cdot 10^2$	$-3.25 \cdot 10^2$	$-1.71 \cdot 10^3$
	$\sum F_z$	$-3.41 \cdot 10^3$	$-3.67 \cdot 10^3$	$1.99 \cdot 10^3$	$-3.62 \cdot 10^3$

In the case of a vertical acceleration of 7 m/s^2 the force distribution reported in Table 6.4 is almost independent from the restraint type. The vertical forces are to be considered extra loads and must be added to the -85 and -105 kN that respectively charge the extremity and the central support because of the 9.81 m/s^2 gravitational acceleration. The Cremonian type takes a smaller percentage of the total 200 kN with the result of a slightly higher charge of the two extremity supports.

The forces arising on the supports and on the restraints as effect of a 30 K temperature difference between the cryostat and the cold mass are given in Tables 6.5. In this case the loads on the supports are of secondary importance with respect to the ones on the restraints. In fact, for symmetry reasons, the central support is not charged at all whereas the extremity supports are allowed to slide with a certain friction. The assumption of free sliding of the extremity supports in the model is conservative for the restraints since in the real case some of the longitudinal force would be transmitted to the cryostat by friction. In case of cold mass thermal expansion the forces taken by the restraint increase directly with their stiffness and can reach critically high values so that a safer solution is represented by a more flexible restraint.

Table 6.5: Sum of forces on support bases and transport restraints induced by a 30 K temperature difference.

$\Delta T=30 \text{ K}$	Forces [N]	3 Mod LR	Cremonian	Ideal
Support bases				
Non-Connection	$\sum F_x$	$6.33 \cdot 10^1$	$8.28 \cdot 10^1$	$3.79 \cdot 10^3$
	$\sum F_y$	$-1.67 \cdot 10^{-1}$	$-2.18 \cdot 10^{-1}$	$-9.98 \cdot 10^0$
	$\sum F_z$	$4.07 \cdot 10^3$	$8.44 \cdot 10^2$	$3.54 \cdot 10^4$
Central	$\sum F_x$	$-4.01 \cdot 10^2$	$-4.30 \cdot 10^2$	$1.31 \cdot 10^3$
	$\sum F_y$	$5.22 \text{E} \cdot 10^{-1}$	$-1.94 \cdot 10^{-1}$	$-6.01 \cdot 10^{-1}$
	$\sum F_z$	$6.41 \cdot 10^3$	$1.31 \cdot 10^4$	$-3.58 \cdot 10^4$
Connection	$\sum F_x$	$5.11 \cdot 10^1$	$6.93 \cdot 10^1$	$3.80 \cdot 10^3$
	$\sum F_y$	$-1.35 \cdot 10^{-1}$	$-1.82 \cdot 10^{-1}$	$-1.00 \cdot 10^1$
	$\sum F_z$	$4.07 \cdot 10^3$	$8.44 \cdot 10^2$	$3.54 \cdot 10^4$
Transport restraints				
Non-Connection	$\sum F_x$	$-1.39 \cdot 10^2$	$-1.34 \cdot 10^2$	$-4.45 \cdot 10^3$
	$\sum F_y$	$-1.41 \cdot 10^5$	$-1.45 \cdot 10^5$	$-4.37 \cdot 10^5$
	$\sum F_z$	$7.27 \cdot 10^3$	$7.38 \cdot 10^3$	$-1.75 \cdot 10^4$
Connection	$\sum F_x$	$-1.48 \cdot 10^2$	$-1.44 \cdot 10^2$	$-4.46 \cdot 10^3$
	$\sum F_y$	$1.41 \cdot 10^5$	$1.45 \cdot 10^5$	$4.37 \cdot 10^5$
	$\sum F_z$	$7.28 \cdot 10^3$	$7.38 \cdot 10^3$	$-1.75 \cdot 10^4$

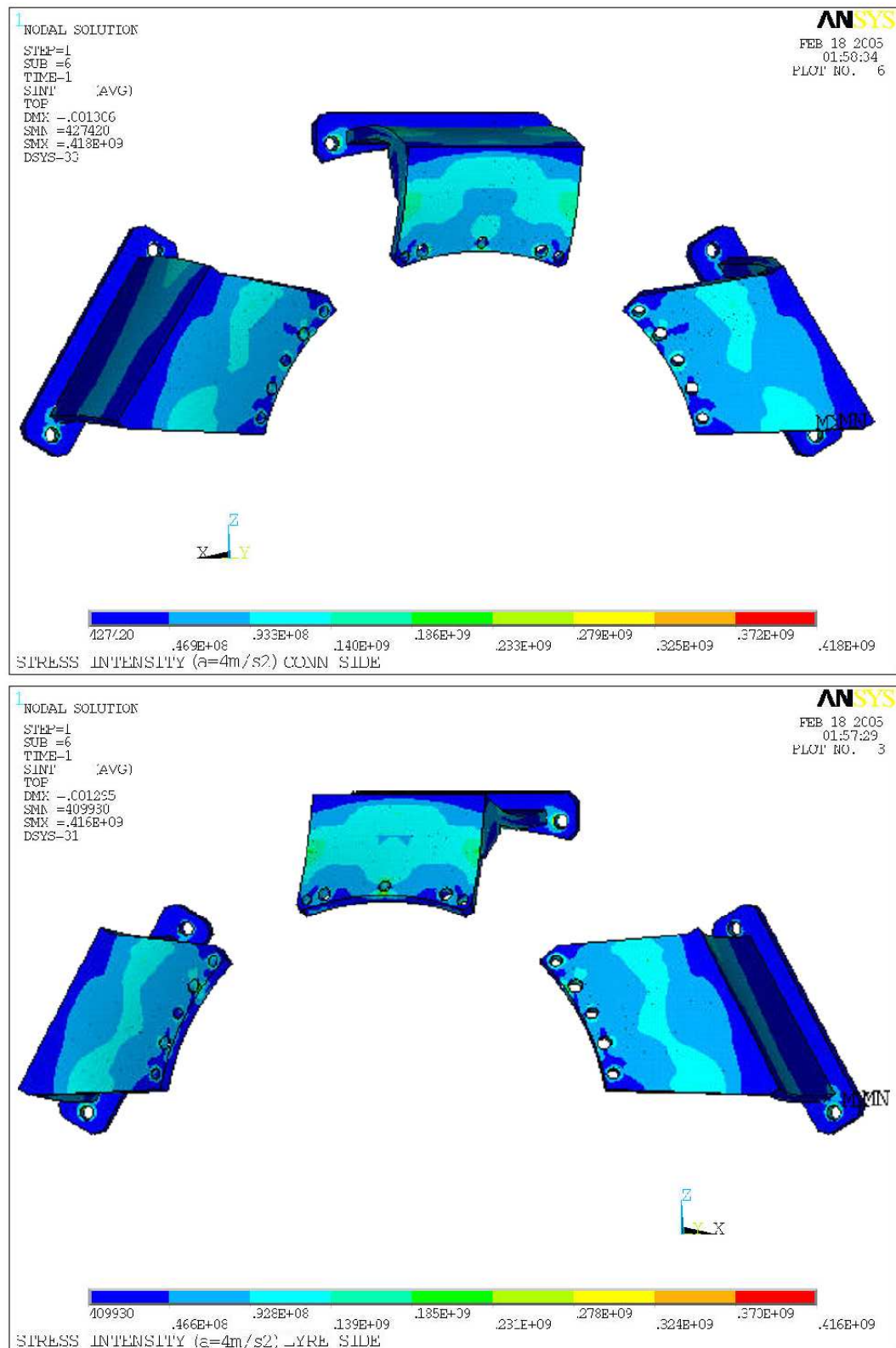


Figure 6.14: Distribution of Tresca equivalent stresses [MPa] in the light restraints induced by a $4 m/s^2$ longitudinal acceleration. Top image is Connection side, bottom is Non-Connection (Lyre) side.

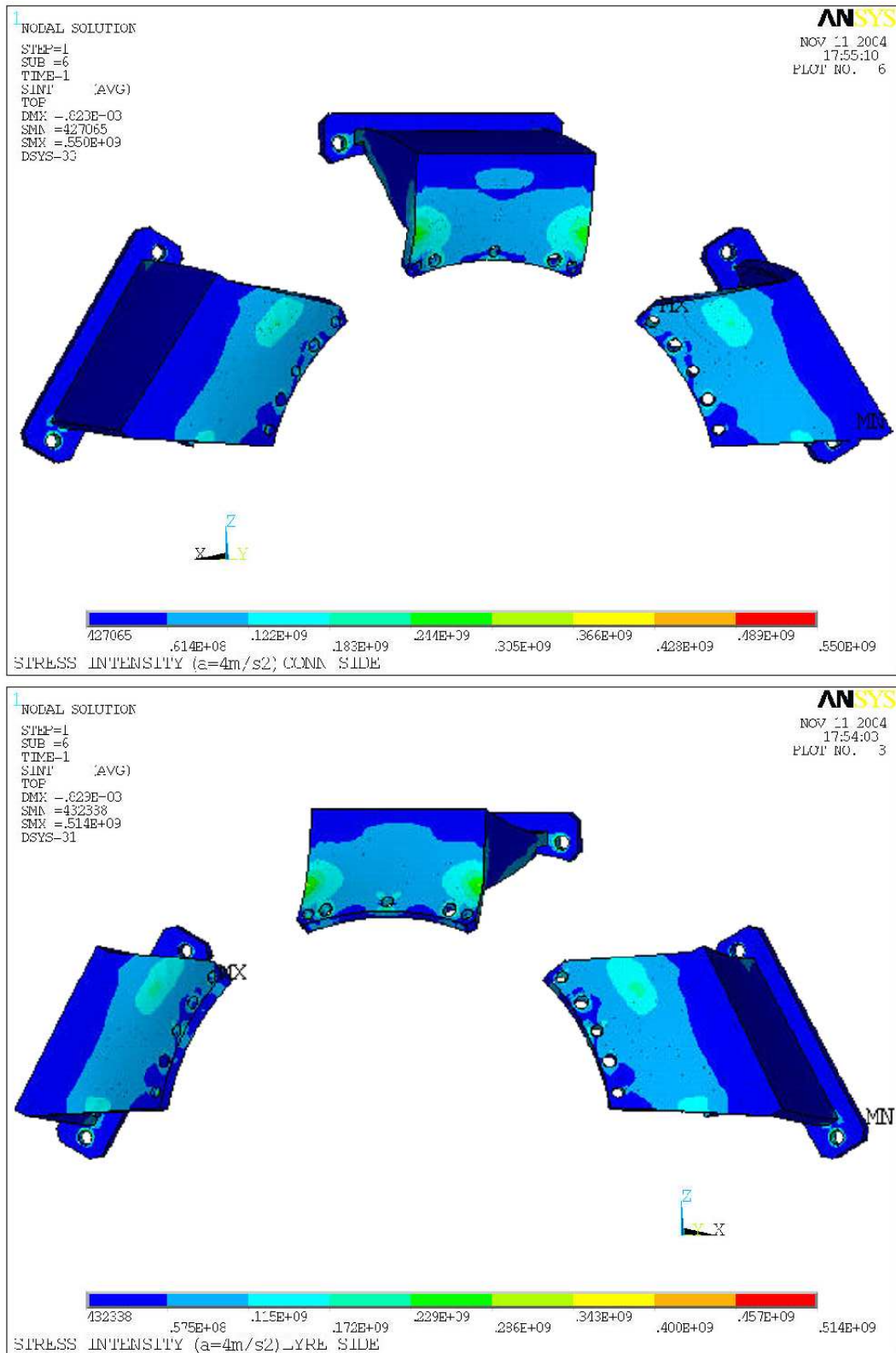


Figure 6.15: Distribution of Tresca equivalent stresses [MPa] in the modified light restraints induced by a $4 m/s^2$ longitudinal acceleration. Top image is Connection side, bottom is Non-Connection (Lyre) side.

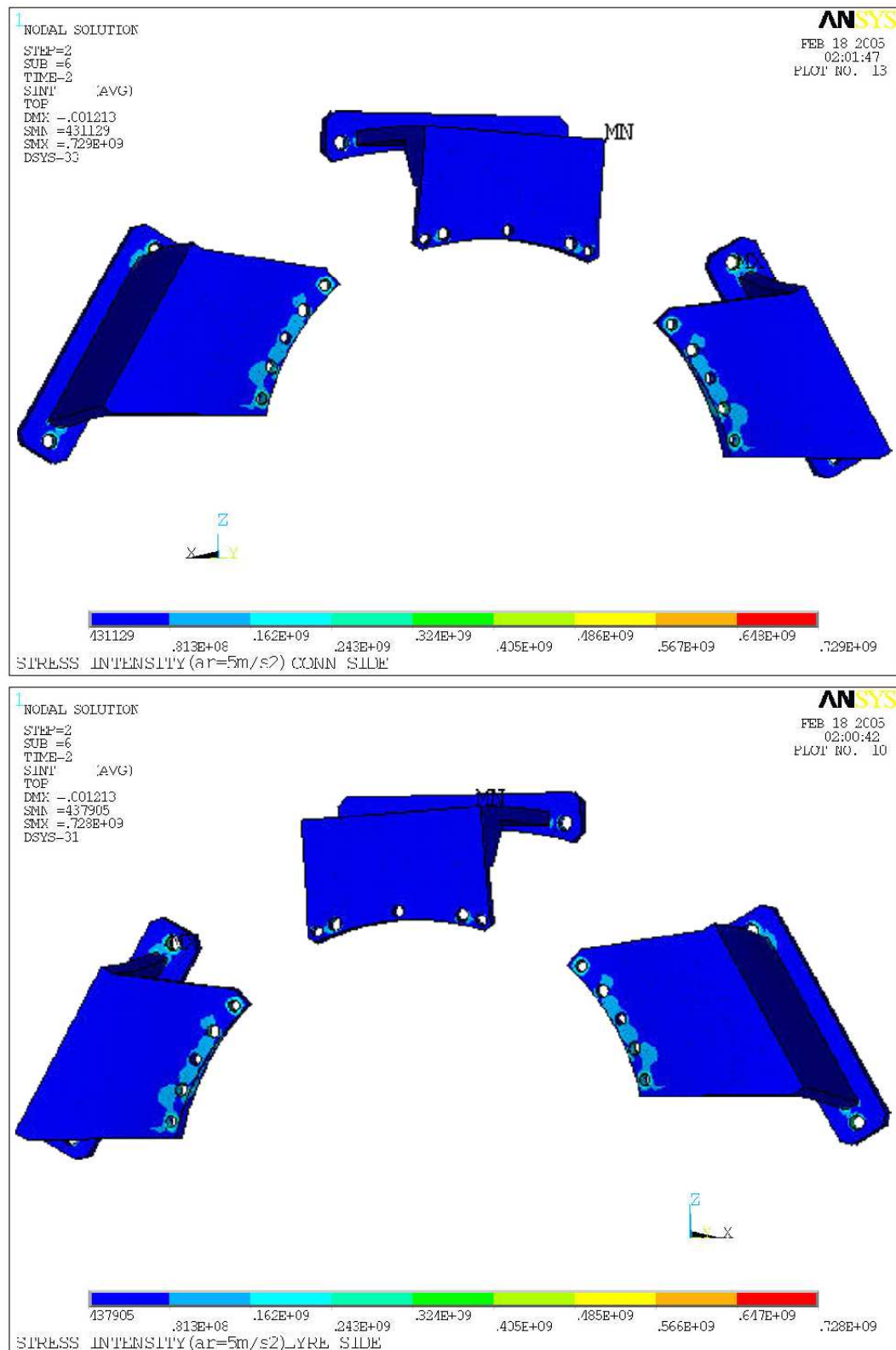


Figure 6.16: Distribution of Tresca equivalent stresses [MPa] in the light restraints induced by a 5 m/s² lateral acceleration. Top image is Connection side, bottom is Non-Connection (Lyre) side.

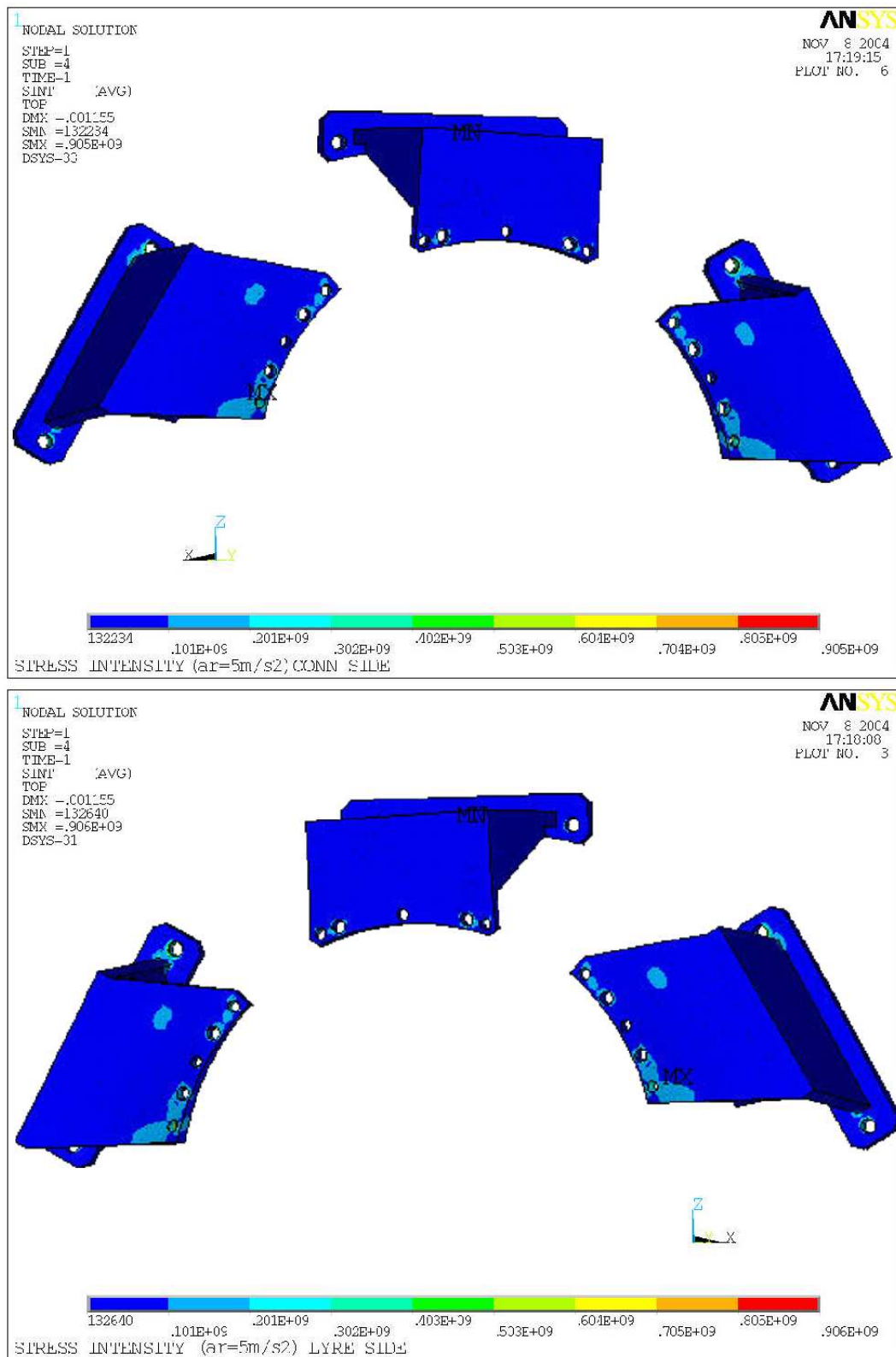


Figure 6.17: Distribution of Tresca equivalent stresses [MPa] in the modified light restraints induced by a 5 m/s² lateral acceleration. Top image is Connection side, bottom is Non-Connection (Lyre) side.

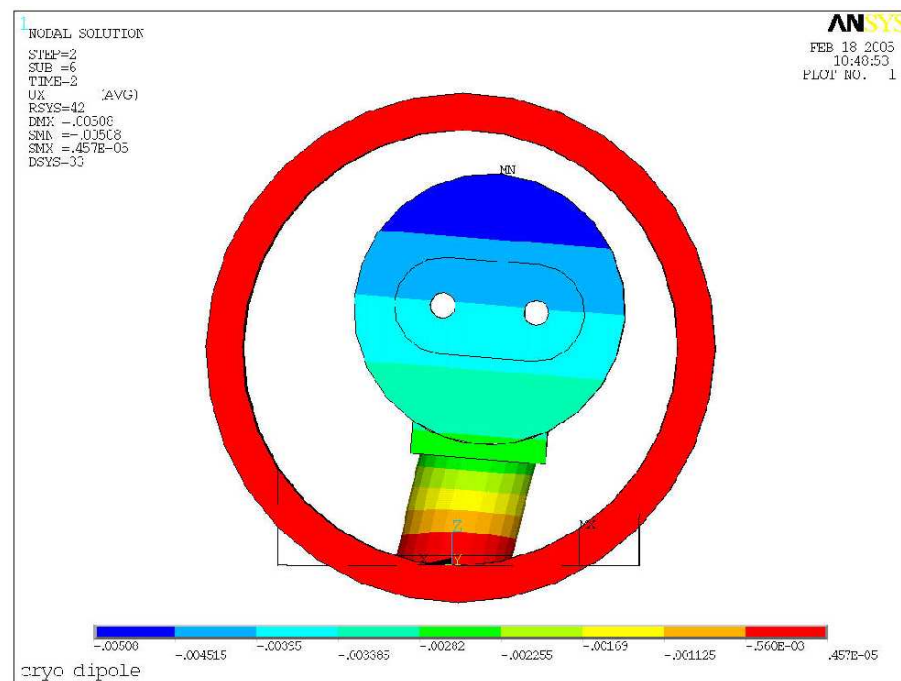


Figure 6.18: Effect of a 5 m/s^2 lateral acceleration on a cryo-dipole equipped with 3 light restraints. Lateral displacement [m] in the middle cross section.

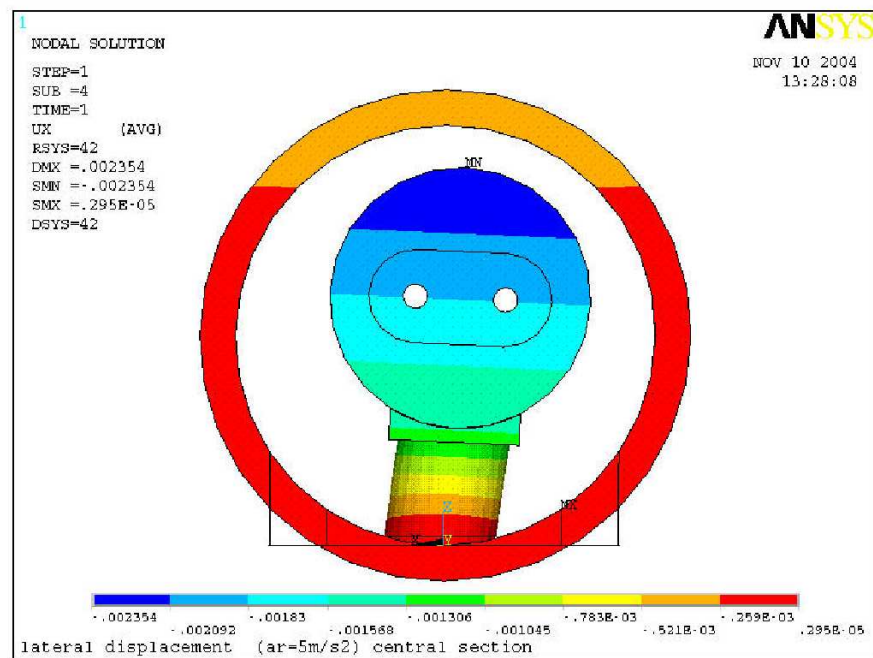


Figure 6.19: Effect of a 5 m/s^2 lateral acceleration on a cryo-dipole equipped with 3 modified light restraints. Lateral displacement [m] in the middle cross section.

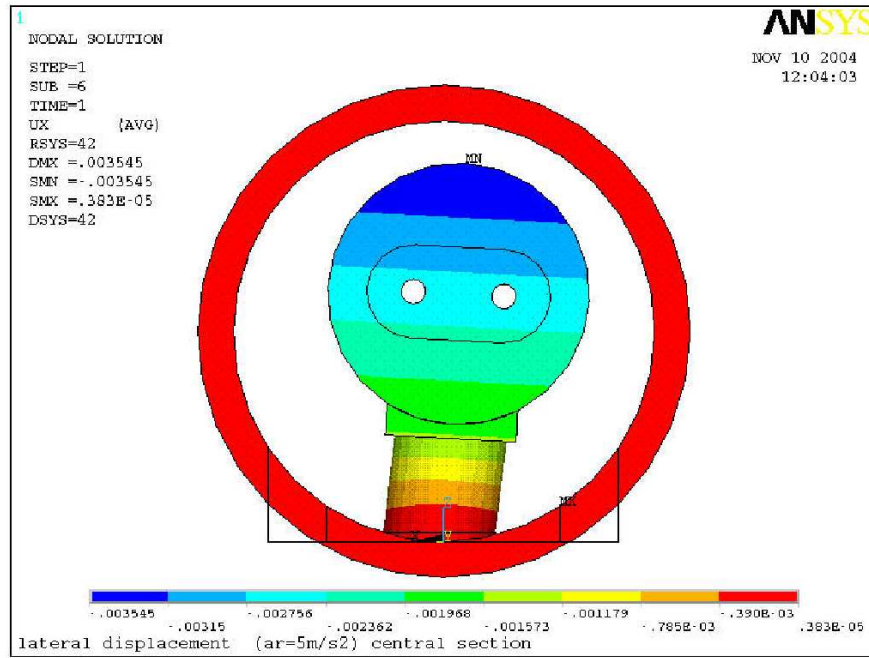


Figure 6.20: Effect of a 5 m/s^2 lateral acceleration on a cryo-dipole equipped with Cremonian type restraints. Lateral displacement [m] in the middle cross section.



Figure 6.21: Effect of a 5 m/s^2 lateral acceleration on a cryo-dipole equipped with ideal restraints. Lateral displacement [m] in the middle cross section.

Table 6.6 gives the cold mass/cryostat relative displacements at the extremities for the three different restraint types.

Table 6.6: Relative cold mass-cryostat extremity displacement in longitudinal direction induced by a 30 K temperature difference.

Displ. [mm]	3 Mod LR	Cremonian	Ideal
u_y	1.90	2.75	0.80

Table 6.7: Lateral (u_x) and longitudinal (u_y) displacements of the central support top respectively induced by a 5 m/s² lateral and 4 m/s² longitudinal acceleration.

Accel. [m/s ²]	Displ. [mm]	3 LR	3 Mod LR	Cremonian	Ideal
5 ²	u_x	2.60	1.25	1.54	0.81
4	u_y	1.25	0.76	0.73	0.12

Table 6.8: Maximum longitudinal stress in the screws connecting the restraint to the cold mass. Values are scaled from a 1 g lateral acceleration simulation.

Stress [Pa]	3 Mod LR
σ_1	$0.70 \cdot 10^8$

We give now, for the three modified transport restraints configuration, the load acting on the most stressed support (usually the central) and the stresses in the constraints summarized in Table 6.9. The total load on the support is the combination of the longitudinal and transversal forces at the column top. The admissible value for such a force in case of pure or guided bending is around 40 kN that drops to 25 kN in combination with a vertical load of 105 kN [41] as the one due to cold mass weight; maximum value for a pure vertical load is 175 kN. It can be noticed that these limits correspond to a safety factor of 2.7 and are often exceeded. The stresses in the restraints given in the table are the equivalent stresses following Tresca theory. We give two values: the ‘Local maximum’ that is the maximum value, usually confined in a small spot close to geometrical discontinuities (holes, corners) where the stresses concentrate, and the ‘Distributed maximum’ that is the higher value distributed over an appreciable area. To judge these values we refer to previous studies on light restraint performance [42] in which, by mean of hardness test, the ultimate strength is evaluated around 530 MPa. Associated to the high local stresses induced by static inertia loads we can consider local plastic deformations and consequent re-distribution of stresses to smaller values.

Table 6.9: Forces on central support and stress distributions in the 3 modified transport restraints for all the loads.

Load case	Force on central support [N]	Max Stress [MPa]	
		Distr.	Local.
$a_y=4\text{ m/s}^2$	$3.53\cdot 10^4 (F_x+F_y)$	230	514
$a_x=5\text{ m/s}^2$	$6.21\cdot 10^4 (F_x+F_y)$	200	900
$a_z=7\text{ m/s}^2$	$7.50\cdot 10^4 (F_z)$	20	100
$\Delta T=30\text{ K}$	$6.41\cdot 10^3 (F_z)$	1300	3000

6.4 Summary

We performed dedicated experiments on a pre-series cryo-dipole by introducing transverse forces similar to those expected in realistic conditions during operation or during cryo-dipole alignment in the LHC tunnel. The experimental results revealed two important facts. From one hand, the deformation of the dipole and of its supports is still elastic, hence no residual deformations should be expected. On the other hand, we observed a rather strong potential interference of the cold mass with the cryostat itself through the sliding posts. Using FEM simulations we were able to point-out that the possible source of the interference is a too large friction coefficient in the sliding interface. The test was done at room temperature and cannot be easily repeated in operational conditions at cryogenic temperature.

Should the strong interference cold mass cryostat be confirmed by farther tests, there will be two important consequences. From one hand, the frictional interference is expected to be beneficial during cryo-dipole transport: it will limit the internal degrees of freedom and hence it will reduce the possibilities of deforming or displacing the cold mass from its nominal position. On the other hand, during thermal cycles the effect of friction is a potential mechanism to produce erratic displacements of the central post and hence to introduce possible change of shape of the cold mass axis and of the position of the multipolar correctors embedded in the extremities. This may be rather detrimental for the reproducibility of beam control

In the second part of the chapter we described the finite element analysis performed to compare the efficiency of different kinds of transport restraints. The different design stiffnesses increase from the three light restraints through the Cremonian and the 3 modified restraints up to the ideal one. Looking at Tables 6.3 to 6.5 it is generally evident that stiffer restraints relief the load directly generated by the acceleration (i.e. in the same direction) on the central support versus the lateral ones. It can also be noticed that stiffer constraints can induce a load distribution characterized by cross-components as happens in statically indeterminate structures. This can be seen, for example, in the lateral (i.e. along X) support reactions consequent to the longitudinal acceleration on a cryo-dipole equipped with ideal restraints (Table 6.3 bottom row).

The stress distributions plotted in Fig. 6.14 to 6.17 show how the modified design increases the stiffness of the restraint by confining slightly higher stresses to a

smaller area on the vertical front plate. Critical spots are represented by all the hole edges and by the connection between the central plate and the back plate that is furthermore close to a hole edge.

The performed simulations highlighted the criticalness of the proposed light restraint solution both in terms of supports and restraints integrity. Dedicated tests and experiments are therefore foreseen to judge the safeness of cryo-dipole transport and handling with the three modified transport restraint solution.

Chapter 7

Operational experience on prototype and pre-series dipoles

7.1 Introduction

The geometrical constraints imposed on dipole shape must be respected in spite of the deformations induced by thermal contractions and Lorentz forces that arise in operative conditions.

In the first part of this chapter we will describe the cold mass geometry modification measured during current ramping (Energization), resistive transitions (Quenches) and thermal transients (cool-down, warm-up). In the second part we will deduce the consequent loads and displacements induced on the central composite support to check for potential risky situations. In the third part we will study in detail the effect of Lorentz forces on the cold mass cross-section: through finite element modeling we analyze the mechanical deformations arising during Energization and we compare them to the experimental data.

7.2 String2 and monitoring system

Magnet displacements and deformations were measured in operative phases during the test of the first LHC full-cell prototype called String2 [43], schematically shown in Fig. 7.1. An LHC ‘DOFO’ cell is composed by a de-focusing quadrupole, three dipoles a focusing quadrupole and three dipoles. Its length corresponds the ele-

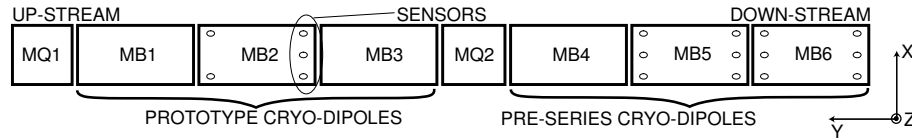


Figure 7.1: String2 magnets layout (LHC standard cell).

mentary cooling loops providing refrigeration at the 1.9 K, 4.5-to-20 K, 50-to-70 K levels to the LHC cryo-magnets. The cool-down of the ~ 200 t cold masses from room to the operating temperature of 1.8 K takes about two weeks. The first refrigerating step from 300 to 80 K is achieved by mean of gaseous Helium injected at decreasing temperature from one string extremity and flowing through the magnets. The further temperature step is obtained through expansion to liquid of sub-cooled super-critical (3 bar, 4.5 K) Helium so that after the expansion the cold masses will be filled with liquid helium at 4.2 K. To reach the operating 1.8 K, the remaining heat is extracted by pumping the vapor on the two-phases Helium flowing in a corrugated heat exchanger tube coupled to the pressurized (1 bar) superfluid Helium bath [44].

This full-scale working model, has undergone typical and atypical operating modes during which the cryogenic apparatus, the magnet electrical circuits and the quench recovery systems have been tested to check their performance and to validate the design choices. In this framework, through the acquisition of magnet extremity displacements in vertical and horizontal directions, it has been possible to identify the operating phases that could harmfully affect the magnet short and long-term mechanical stability.

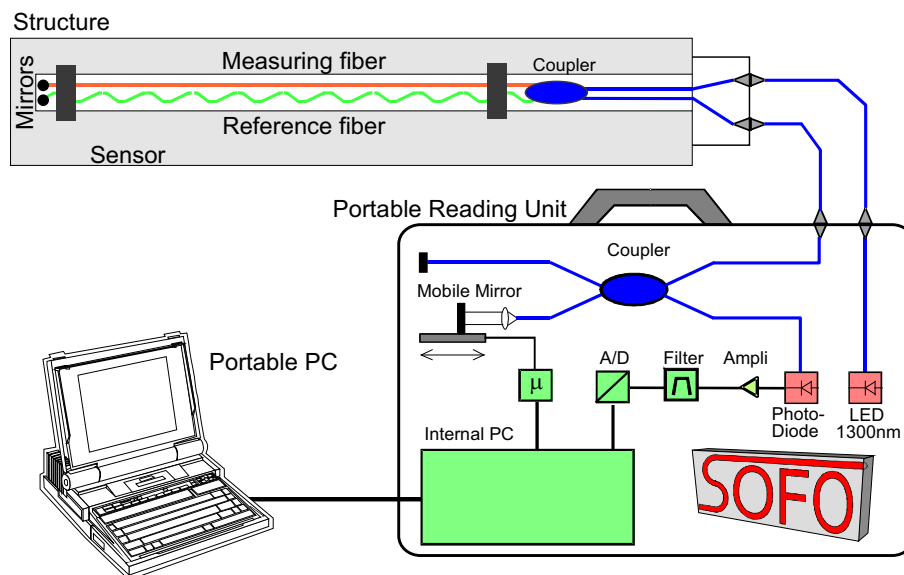


Figure 7.2: Original SOFO system.

In the choice of the monitoring system, the extreme environmental conditions represented by the vacuum and the 300 K thermal gradient between the cold mass and the surrounding cryostat did not suggest common deformation sensors like strain gages or inductive comparators. In fact both of these would have acted as thermal bridge between cold mass and cryostat and consequently suffered from deformations induced by very high thermal gradients. Moreover the magnet extremity six degrees

of freedom would have made hard to distinguish a deformation along one direction from tilt and from deformations in other directions. These constraints pushed us toward a tailor made solution developed in collaboration with the EPFL (Ecole Polytechnique Federale de Lausanne) and SMARTEC S.A. [45]. In fact, the original idea to overcome all the previous issues by mean of an optical device was eventually realized through the modification of a commercial measuring device (‘SOFO’ [46]) used to monitor deformations in civil structures and already in production by SMARTEC S.A.

The original SOFO system, shown in Fig. 7.2, was developed to observe structural deformations in civil engineering construction and consists of two Michelson interferometers arranged in chain configuration. It measures the length difference between two fibers; one, called ‘measuring fiber’, is attached to the structure to monitor whereas the other, called ‘reference fiber’ is freely installed in the nearby. Such original SOFO configuration cannot be employed to detect cold mass deformations since the large temperature gradient suggests preventing any thermal contact, even through optical fibers, and the longitudinal contraction of the cold mass potentially complicates the data interpretation. Thus, to adapt the original sensor to our needs, the measuring fiber has been replaced by the double pass delay line shown in Fig. 7.3.

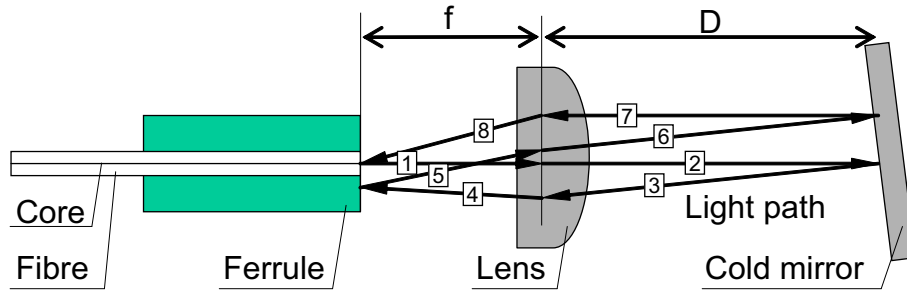


Figure 7.3: Double pass delay line replacing the measuring fiber.

In the operative configuration, a mirror placed on the cold mass (cold mirror) reflects the radiation emitted by an optical fiber through an optical head, located on the inner wall of the vacuum vessel. The LED primary radiation enters in the vessel through a fiber and an optical connector, illuminating through a coupler both the reference fiber and the delay line. In the latter, the fiber end, mounted inside a polished reflective ferrule, irradiates a focusing lens and, through the head mirror, reaches the cold mirror. The light is reflected back and forth from the cold mirror to the ferrule. As the position of the fiber end and the lens focal point are optically conjugated through the lens-mirror system (double pass delay line, Fig. 7.3), after two round trips the light will be focused back to the fiber core. The coupler mixes this radiation with the light reflected back by the reference fiber end and feeds a SOFO-type analyzer arm (mobile mirror in Fig. 7.2) monitoring the distance between the ferrule and the mirror, i.e. between the vessel and the cold mass.

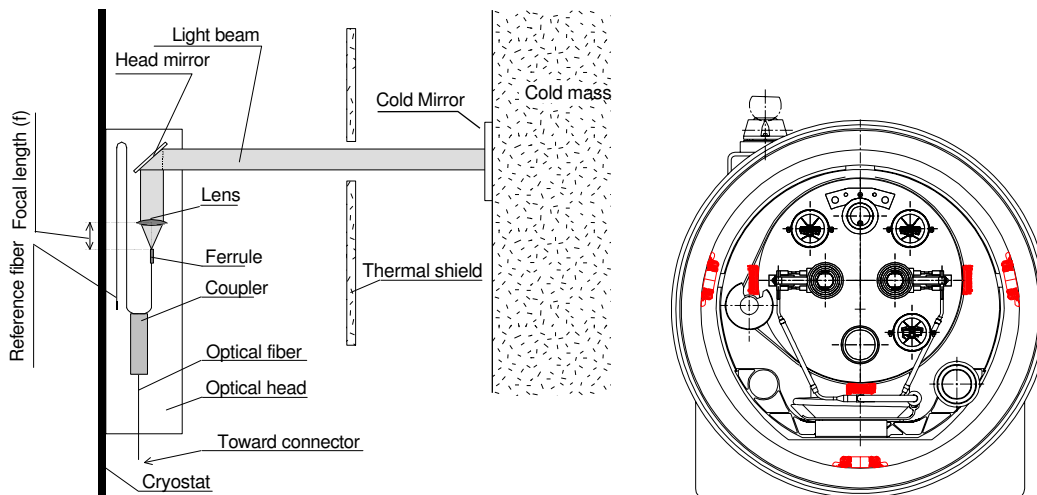


Figure 7.4: Installation of the SOFO modified sensor.

To monitor vertical and horizontal position of the ends (that is along Z and X axis of Fig. 7.1 reference system) as well as cross-section contraction, three sensors mounted as shown in Fig. 7.4 are needed for each magnet extremity. Three sensors were installed in both ends of the pre-series dipoles MB5 and MB6 and in the down stream end of the prototype MB2. Only two sensors were mounted in the up stream of dipole MB2 so that no vertical displacement could be detected in that extremity. The optical device main features are summarized in Table 7.1.

Table 7.1: SOFO main features.

Parameter	SOFO characteristic
Complete system reading resolution	0.01 mm
Resolution	0.002 μm
Precision	better than 0.2 of measured deformation
Measurement range	~ 50 mm
Cable length	Up to 5 km
Temperature sensitivity	Insensitive: self-compensated sensors

7.2.1 String powering

Before reaching the nominal energy, particles have to travel several million turns at increasing momentum so that, to keep them in the same circular trajectory, an increasing dipolar field is required. In this 20 min-long transient phase, the increas-

ing electro-magnetic forces can modify the stress distribution inside the coils and may provoke a slight change of the cold mass curvature and a consequent sizable misalignment of the extremities in radial and vertical directions. Both phenomena have been detected during the energization of the main magnet circuits performed in the cold test facility.

The amount of collected data, once manipulated to make them homogeneous, revealed a reproducible behavior of magnet ends in terms of displacements and cross-section deformation. The typical effect of current ramping on the cold mass cross-section is displayed in the top graph of Fig. 7.5, where the exciting current and the horizontal diameter of a pre-series magnet are plotted versus the time. The tight

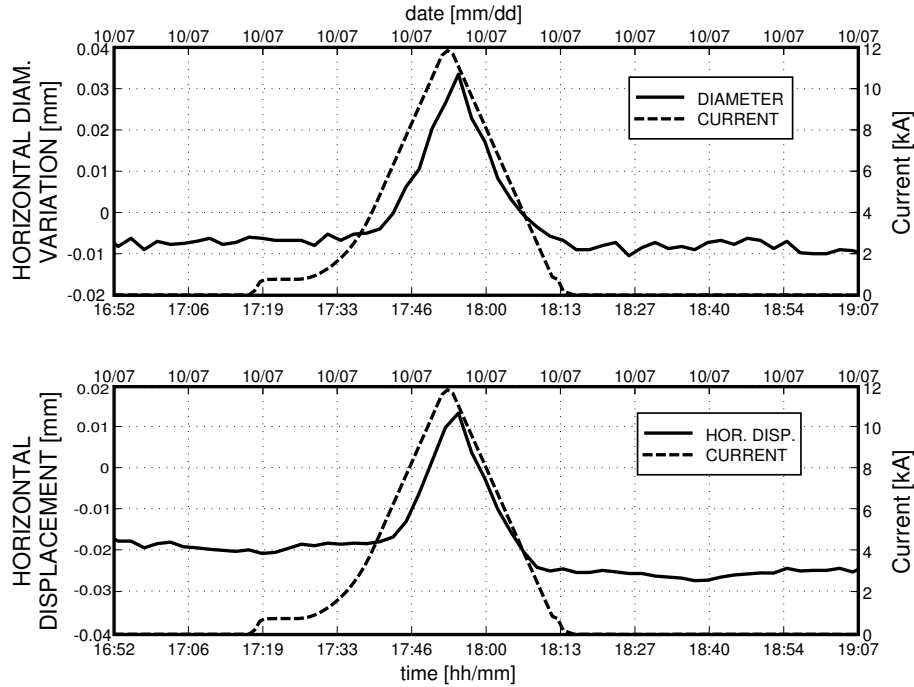


Figure 7.5: Energization effect on horizontal displacement and outer cold mass diameter variation of prototype magnet MB2.

correlation between diameter variation and current level is evident in spite of the horizontal shift of few minutes due to different settings of measuring system clocks. Diameter variation is due to the electro-magnetic forces acting on the coils and pushing along the top-bottom symmetry axis of the cross-section, in outward direction. By assuming a linear elastic behavior of the cold mass the current-deformation relation that comes from the Lorentz equation is parabolic and precisely fits the experimental data. A clear current-driven behavior is also visible in the bottom part of Fig. 7.5 where the horizontal displacement of the pre-series dipole end is plotted along with the current ramp, versus the time. In this case the relation cannot be quickly resolved in a quantitative way because of the three-dimensional

nature of the phenomenon. We interpret it as a straightening of the cold mass in the horizontal plane due to the coil thrust that counteracts the elastic forces that keep the cold mass bent. What must be pointed out first is the magnitude of the observed phenomena which is rather small with respect to the critical values that could affect the machine performance. Maximum displacements in fact, generally far below 0.1 mm in horizontal direction and around it in vertical direction, cannot result by themselves in a harmful misalignment of the multipolar correctors (that is > 0.3 mm). Second point to be noted is the fully elastic feature of the displacements and deformations provoked by current-related phenomena. It is indeed clear, in both the figures, the absence of any significant residual effect on the diameter size as well as on the displacement once that the current is brought down to the original value. In Table 7.2 we summarize maximum displacements and deformations experienced

Table 7.2: Energization-Induced Displacements

$I_{max}[\text{A}]$:		5000	8000	10800	11850	
n of meas.:		4	1	2	14	
<i>magnet</i>	<i>def.[mm]</i>					
						Mean Std
MB2	Δd_{max}	<0.01	0.02	0.02	0.04	0.002
	ΔX_{max}	<0.01	0.01	0.03	0.04	0.002
MB5	Δd_{max}	—	0.02	0.03	0.03	0.004
	ΔX_{max}	—	<0.01	0.03	0.06	0.03
	ΔZ_{max}	-0.01	0.08	-0.14	-0.09	0.04

by two string magnets for different current ramps. Data are about the down stream extremity of a pre-series and of a prototype magnet for which the vertical displacement is not available. From those data (averaged over all the measurements), we see that diameter variation Δd_{max} and horizontal displacement ΔX_{max} are small and to follow the same linear trend in both the magnets whereas vertical displacements ΔZ_{max} shows a slightly larger size and a more nervous trend.

7.2.2 String quenches

Quenches performed in the string have been provoked at different current intensities, on different magnets and with different current decay time rates. In spite of the different quench features, the analysis showed up quite well reproducible behavior for the diameter and for the horizontal displacements. Quenches are provoked by resistive heaters placed in specific locations of the coil and activated at pre-defined current values. It can be noticed that in the first part, that is the current ramping, there is no difference with respect to the energization phase. This is clearly visible in the top graph of Fig. 7.6 where the diameter variation is plotted, along with the

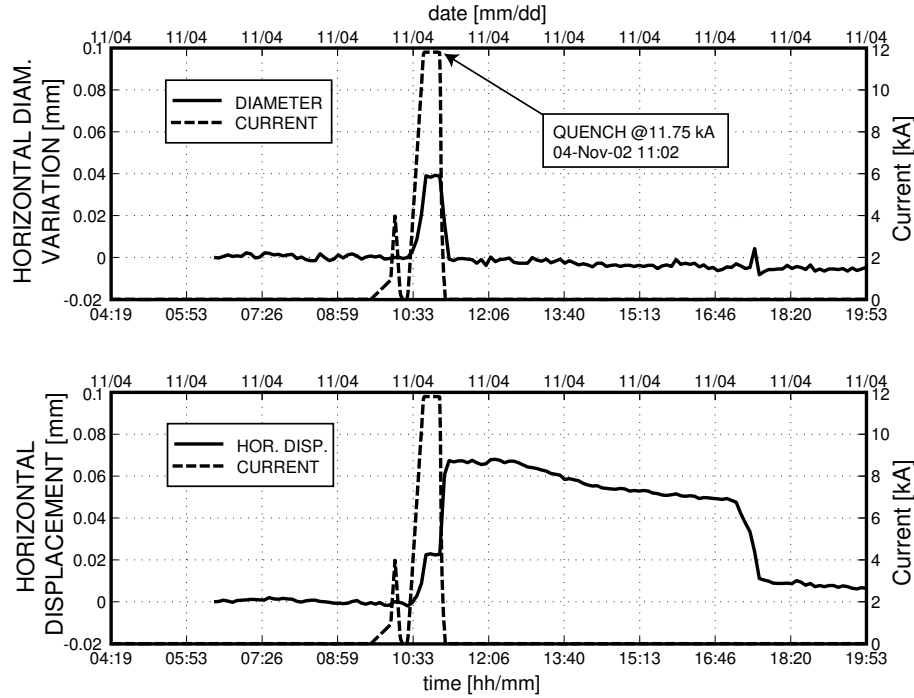


Figure 7.6: Horizontal displacement and diameter variation induced by quench at 11.75 kA

current, versus the time. After the preliminary part, in which the current raises with a fixed time-rate value, the current is kept constant until the quench is provoked and then it is cut off by the protection system. We notice that the diameter closely follows the current profile so that after the current cut no residual deformation is present in the cross-section. The horizontal displacement of magnet extremity for the same quench test is visible in the bottom graph of Fig. 7.6. The behavior is the same for the current ramp until the quench occurs. After the quench and the consequent current cut, the magnet end experiences a sizable displacement in the horizontal direction of about 0.7 mm, recovered only much later. Since that happens after the quench it cannot be obviously related to electro-magnetic forces and a plausible explanation can be found in the thermal-driven phenomena. One of the main outcomes of a resistive transition is, indeed, the release of a large amount of magnetic energy dissipated as heat in the coil. Moreover, at very low temperatures the specific heat and the thermal conductivity of metals are both low so that a little amount of energy can cause a relevant and localized increase of temperature in the structure. This can be seen in Fig. 7.7 where magnet temperature, measured in proximity of the quench spot, is plotted along with the end displacement, versus the time. As soon as the quench takes place the current drops and the temperature rises very quickly and so does the horizontal displacement. The amount of stored energy needs a long time to be extracted by the helium and, as visible in the plot,

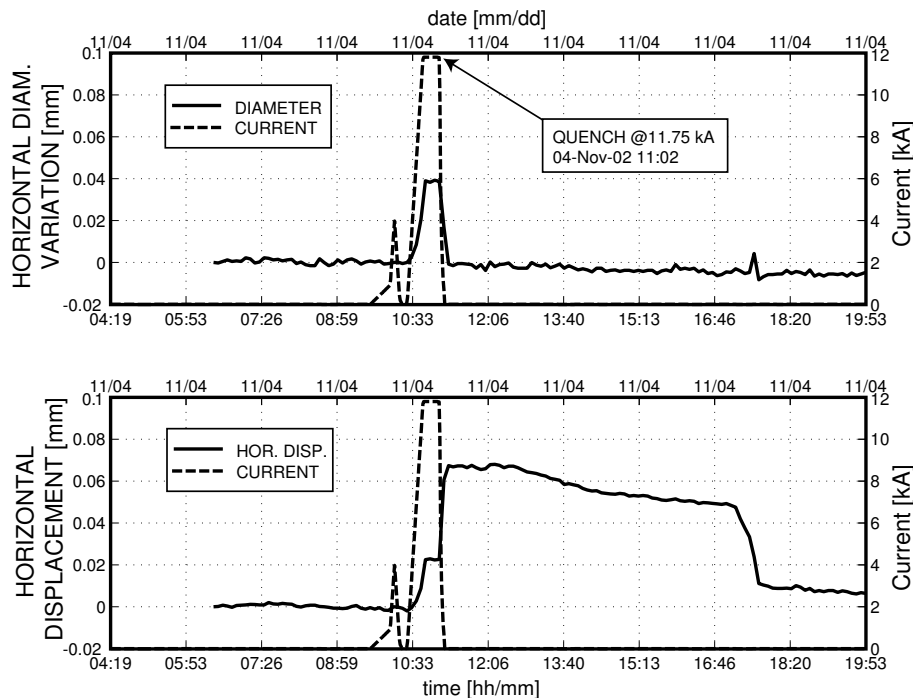


Figure 7.7: Horizontal shift and temperature raise provoked by quench at 11.75 kA

more or less the same time is needed by the magnet to regain its original position. The relation between thermal and structural phenomena is thus evident even if a quantitative model is not straightforward. The recovery time, reported in Table 7.3 along with a summary of the collected data, is generally around 3.8 hours with a standard deviation of about 0.8 hours.

The maximum displacement, usually reached just after the energy release by the coil resistive part, is not very large in the horizontal direction (ΔX_{max}) whereas is almost critical in the vertical direction (ΔZ_{max}). In spite of the few (5) available data the reproducibility is quite good and the average value is set close to the critical 0.3 mm. In operative condition, anyhow, such a sizable misalignment is reached when

Table 7.3: Displacements Induced by Quenches

	Mean	Std	<i>n</i> of meas.
ΔX_{max}	0.07 mm	0.02 mm	23
Recovery Time	3.8 hours	0.8 hours	
ΔZ_{max}	-0.24 mm	0.03 mm	5
Recovery Time	3.6 hours	0.7 hours	

the beam has already been dumped because of the quench and the recovery toward the original position, accomplished after the recovery time, ensures that there is no real danger for beam stability related to this effect.

7.2.3 String cool-down and warm-up

The effects of thermal gradients along the magnets can be made clearly visible in the cooling phase, needed to bring the magnet structure down to the operational temperature of 1.9 K. In fact the cool-down phase, is performed by flowing helium through the magnets. Cold gas is injected from one end (up-stream) at decreasing temperature and extracted from the opposite (down-stream) [47]. The cool-down rate provoke the longitudinal thermal gradient with a consequent structural deformation of the dipole. Both fast or slow cool-downs were already proved to provoke shift of magnet end positions in previous tests performed either on prototype and on pre-series magnets as reported in [48]. In those occasions non-negligible displacements affecting the magnet also after the transient were detected during fast cool-downs in prototype magnets. The most unfavorable event indeed was a peak displacement of 2 mm in horizontal direction experienced by a prototype magnet during a fast thermal transient.

Table 7.4: Displacements Induced by Slow Cool-Down

<i>end</i>	<i>def</i> [mm]	MB2	MB5	MB6
Up Stream	Δd		-1.14	
	ΔX_{max}		-0.30	
	$\Delta X_{residual}$		-0.20	
	ΔZ_{max}		-1.37	
	$\Delta Z_{residual}$		-0.92	
Down Stream	Δd			-1.00
	ΔX_{max}			0.10
	$\Delta X_{residual}$	0.40	0.20	0.02
	ΔZ_{max}		-1.20	
	$\Delta Z_{residual}$		-1.10	

In the run of the String2 the cool-down was of slow rate in order to keep the thermal gradient along a single magnet below 80 K and to limit potentially harmful thermo-mechanical stresses. The measured displacements in vertical and horizontal direction are reported, along with the diameter contraction, in Table 7.4. In spite of the lack of data due to temporary sensor failures, it can be noticed a diameter contraction Δd close to the one expected (1.2 mm) and the presence of non-zero

Table 7.5: Residual Displacements after String Shut-Down

	Up Stream		Down Stream	
	ΔX [mm]	ΔZ [mm]	ΔX [mm]	ΔZ [mm]
MB2	0.02	-	-0.04	-0.07
MB5	0.20	-0.10	-0.03	-0.07
MB6	-0.06	-	-	-

displacements in both directions once terminated the transient phase. In vertical direction ($\Delta Z_{residual}$) they are induced by support post and cold mass shrinking (0.3 and 0.6 mm, respectively) and close to what expected, whereas in horizontal direction ($\Delta X_{residual}$) they can reach critical values and are not fully understood yet. To check if the misalignments provoked by cool-down are still present after the string warming up to the room temperature one can look at Table 7.5 in which are reported the measurement taken right after the string shut down. It can be noticed that the measured displacements are usually around few hundredths of millimeter and always smaller than the tolerance range.

7.3 Loads on central composite support in working conditions.

As already mentioned in Section 2.2.7 the cold mass-cryostat interface is one of the most critical components of the LHC cryo-dipole. It is composed by three thin walled short cylinders made of glass fiber reinforced with epoxy, a composite material chosen for its favorable balance between structural and thermal properties. Each column has in fact to bear a vertical load of ~ 100 kN and a maximum thermal gradient, in steady state conditions, of 1500 K/m. Magnet shape modifications during operative phases induce support deformations and consequent extra stresses in the thin composite material that could affect its mechanical integrity. For this reasons we used the geometrical measurements taken during magnet testings to evaluate the intensity of the extra static loads acting on the supports during, cool-downs, quenches and energization phases. Our attention focuses on the central support as it is the one subjected to higher loads and deformations.

As the cryo-dipole design doesn't allow a direct measure of the central foot deformations, the first step is to deduce them from the extremity displacements that we have already measured (see 7.2). Extremity displacements can be associated to two different phenomena outlined in Fig. 7.8. The first is a rigid tilt of the entire cold mass around a longitudinal axis whereas the second is a variation of the nominal curvature; we will refer to them as to the tilt and bending scenario, respectively.

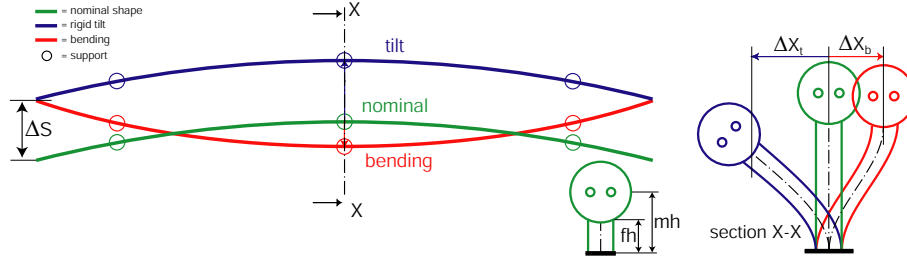


Figure 7.8: Different possible scenarios featuring the same extremity horizontal displacement ΔS (view of X section is out of scale).

In the tilt scenario the central foot top displacement Δx_t for a given extremity displacement ΔS will be approximatively given by:

$$\Delta x_t \approx \Delta S \frac{fh}{mh} \quad (7.1)$$

where: $\frac{fh}{mh}$ is the ratio between the height of the feet and of the measured point that corresponds to 0.42. As shown in Fig. 7.8 in the tilt case all the three feet are subjected to the same bending resulting from the lateral displacement and rotation of their top extremity.

In the bending scenario, to evaluate the foot displacement, we must take into account two main assumptions: the cold mass shape is well represented by a parabolic curve and the three feet have the same rigidity to flexion. The three feet are thus subjected to a guided bending that is imposed by the lateral translation without rotation Δx_b of their top extremities. Under the previous assumptions the relation between magnet extremity and central foot displacement is given by:

$$\Delta x_{b_{ctr}} = 0.55\Delta S \quad (7.2)$$

$$\Delta x_{b_{trl}} = 0.27\Delta S \quad (7.3)$$

for the central and the lateral feet, respectively. The geometrical considerations behind the two equations can be found in Appendix E.

We can now easily analyze the influence of different operative circumstances that we monitored during magnet testings. The extremity displacements measured during cool-down, warm-up, energization and quenches are given in Table 7.6. The specifications to guarantee the mechanical integrity of the support posts define 1.8 mm [41] as the maximum transversal displacement of the top extremity that roughly corresponds to a transversal load of 40 kN. In Table 7.6 we give the central foot displacements evaluated in the two possible scenarios for each operative phase.

As one can see the reported values are quite far from the dangerous limit of 1.8 mm in every operative phase. However it must be pointed out that this study did not take into account the presence of any pre-stress in the composite material associated, for example, to the blocking of the central foot during cryostating or to a

Table 7.6: Displacements of extremities (measured) and of central support (computed).

Extremities		Central support		
Operative phase	Max. hor. displ. [mm]	Operative phase	Hor. displ. [mm]	
			Tilt	Bending
Energization	0.17	Energization	0.07	0.09
Quenches	0.1	Quenches	0.04	0.05
Cool-down	1.2	Cool-down	0.5	0.66

particular displacement not completely recovered because of the friction at the foot base.

7.4 Modeling of cross-section deformations in working conditions.

In superconducting magnets, a crucial aspect to guarantee the expected performance is the mechanical behavior of the structure. Every conductor deformation is reflected indeed on the field shape spoiling its quality. In our case the coils can undergo unwanted deformations mainly in two circumstances; these are the assembly and the energization phases. During the assembly, at room temperature, the coils are clamped by the steel collar, the iron yoke is assembled around the collar and all these components are tightly enclosed in the shrinking cylinder. That procedure usually provokes internal stresses in the coils up to 130 MPa that can lead to consistent cable deformations and displacements.

The energization phase takes place at the operational temperature of 1.9 K and it consists in the progressive increase of current flow through the coils. In this occurrence Lorentz forces grow up inducing coil deformations that can spoil the dipolar field by enhancing the multipolar components. An intense analysis of coil geometries influence on field quality has been carried out in the last years [16]. The aim is to provide a model of the whole magnet cross section to allow the early detection of defects in the magnet assembly and of faulty components. Therefore, it must be suitable for the definition of potential corrective actions, on series production, to drive the field quality inside the tight constraints given by beam dynamics. Here we report the validation of the magneto-mechanical behavior of the cross section model, described in Chapter 3.4, through the comparison with mechanical measurements taken during the energization phase of the LHC test String2.

7.4.1 Mechanical modeling versus measurements at 1.9 K

In the energization phase, the electromagnetic forces acting on the coils deform their confinement structure as well as the iron yoke and the shrinking cylinder. That means an increasing of the cross-section diameter in the horizontal plane. The model has thus been validated through the comparison of the diameter variation as a function of the current. In the magneto-static finite element model, five different current densities have been defined for the areas corresponding to the cables. The corresponding Lorentz forces acting on the cables have been obtained as results and then used as load in the structural model along with the thermal shrinking induced by the cool-down. The related measurements have been taken during the energization of the LHC test String2. The horizontal diameter variations have been measured in two dipoles (named ‘MB2’ and ‘MB5’) during two different current ramping (‘ct1’ and ‘ct2’) by mean of a measuring system based on optical interferometry and described in Section 7.2 . In order to have the diameter variations as a function of the current the electrical and mechanical measurement have been correlated. The post-processed experimental data, providing diameter increase versus current values, are shown in Fig. 7.9 along with model result. It can be noticed the almost

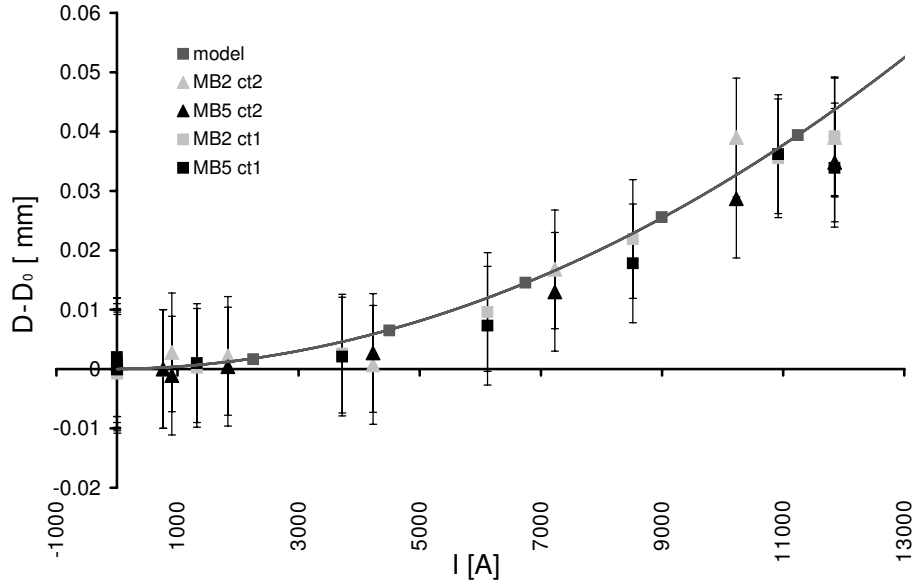


Figure 7.9: Diameter variation versus current intensity for two magnets (MB2, MB5) and two current ramps (ct1,ct2).

perfect parabolic shape of the model that reflects the quadratic relation between the forces and the current and the linear relation between forces and deformations. This trend is evident also in the experimental data in spite of some small spread between different magnets and, for MB2, also for different current ramps. The agreement between model and data must be considered also at cryogenic temperature really

good. It must be pointed out that, to obtain the correct intensity of electromagnetic forces for a given current, it is necessary to take in to account the lack of parallelism between the current flow and the coils. The Rutherford cable structure is actually made of twisted strands arranged in two layers. Following the twisted strands, the nominal current in both the two layers is never going in the longitudinal direction of the cable. The effective current that we must consider for the computation of electromagnetic forces, is thus given by the longitudinal component of the nominal current, that is around the 95% of it.

7.5 Summary

To ensure the respect of the imposed tolerances on alignment and shape of the main LHC dipole, three cold masses of the LHC cell prototype String2 were equipped with specifically developed optical sensors. Cold mass end positions were thus monitored with respect to the cryostat during the whole series of test performed on String2 to reproduce standard working conditions as well as risky occurrences as, for example, propagation of resistive transitions (Quenches). During energization the maximum horizontal displacements generally did not exceed 0.05 mm whereas in vertical direction they reached -0.1 mm. Effects of quenches led to larger displacements due to the release of thermal energy in the conductors. Maximum misalignments of the ends in vertical and horizontal direction, around 0.1 mm and 0.2 mm respectively, were considered safe since they will occur when the beam will be already dumped. Such displacements are usually recovered as soon as a uniform temperature along the magnet is restored as generally happens after some hours. More critical effects are related to the deformations induced by thermal transients. During nominal cool-down rate they can reach values of some tenths of millimeter (at the maximum of the temporary longitudinal thermal gradient) and can sporadically lead to small residual misalignments. It must be nevertheless pointed out that the worst cases were generally represented by displacement never exceeding 0.3 mm. A last note is that small residual deformations and displacements induced by cool-down can persist even after the opposite thermal transient (warm up).

To evaluate the effect of cold mass displacements and deformations on the crucial component represented by the composite support posts we used the measured extremity displacements. We took in to account two possible scenarios to relate displacement of the extremities to displacements of the central foot that is the most charged. Both the scenarios gave a ratio of around one half between extremity and foot displacement. We found that even the maximum displacements ever measured at cold mass extremities didn't result in dangerous situation for the central foot.

A magneto-mechanical model for the LHC superconducting dipole has been outlined. Outstanding features of this model are the modelization of coil mechanical properties to take into account non-linearities, mechanical hysteresis and assembly procedures [16]. This finite element model is currently used at CERN to foresee

conductor displacements due to thermo-mechanical and electro-magnetic phenomena taking place during various stages of magnet life. We compared modeled and measured variation of dipole diameter during the energization and we found a very agreement is found.

Chapter 8

Conclusions

The research activity reported in this thesis dealt with the geometry of the superconducting dipole for the Large Hadron Collider. The purpose was to face the different events, expected and unexpected, that could modify the precise geometry of the structure and evaluate their effect through the development of models and tests.

We analyzed and modeled the mechanical behavior of the main superconducting dipole for the Large Hadron Collider. We implemented both analytical and finite element models to foresee and interpret cold mass geometry variations; we validated and tuned model properties accordingly to dedicated experimental investigations.

We monitored over 2/3 of the magnet production from the point of view of the geometry. We followed all the successive steps as the assembly, the transport to CERN, the cryostating, the testing at cold and the final storage. We defined two characteristic parameters of magnet geometry to easily identify faulty shapes: the horizontal sag and the extremity positions. The statistical analysis revealed that the nominal curvature, obtained with the assembly in the industries, is susceptible to changes in the post-assembly steps. In particular, the systematic increase of the horizontal sag along with the displacement of the extremity toward the curvature center, highlighted the tendency of the cold mass to increase its horizontal curvature. We found that an important change of curvature occurs during the road transport from the industries to CERN whereas the other phases slightly influence the geometry. We concluded that the geometry instability is likely due to an amount of elastic energy in the cold mass trapped by friction between internal laminations. A stick-slip effect, activated by dynamic excitation, helps the release of such energy letting the cold mass assume the shape of the enveloping cylinder that, by design, has a larger curvature.

We found that some of the measurements in the database had been taken with different boundary conditions. We used the analytical model to automatically identify the boundary conditions and subtract their effect from the measured geometry.

A proposed solution to the problem of cold mass shape instability was the blocking of the central support with respect to the cryostat. We simulated the effect of two alternative strategies on all the magnets in the database and we compared the

results. We found that the cheaper and faster solution was still effective and we therefore endorsed it.

For what concerns magnet shape in the vertical plane, the deflection induced by gravity resulted bigger than what expected. We therefore investigated if that was due to a systematic fault of the shape obtained in industry. As gravity is always present during geometric measurements, we had to disentangle effect of gravity and intrinsic shape in the already stored geometry data. We used the analytical model to estimate the effect of gravity through the best fit of the measurements. To check for consistency we studied a group of magnets with measurements taken on three and on two supports and we found no systematic fault of the shape in the vertical plane. We found, instead, that the deflection induced by gravity was bigger than expected and we concluded that the cold mass flexural rigidity had been previously overestimated.

To measure the magnet geometry with a few tenths of millimeter accuracy over 15 m, a multi-station measurement based on laser tracker technology, is used. To estimate the operative accuracy associated to the measure we implemented all the procedure steps in a numerical simulation. Starting from laser tracker specifications we reproduced the error propagation through each measuring step by means of a Montecarlo-based simulation. By comparing the simulation results with the real measurements we were able to identify critical circumstances related to the potential instability of the laser tracker. We also found that the accuracy reaches an asymptotic value characteristic of the multi-station procedure so that we suggest not to increase the number of stations.

The main field direction is a very important requirement for machine performance. The angle check procedure is complicated by the assembly hall logistic that requires two different measuring benches. We were therefore interested in evaluating the influence of the test bench on measurement accuracy: we set up a dedicated test and we simulated several different bench configurations. We then checked the presence of undesired cold mass longitudinal twist induced by the bench. We found that the influence of test bench poor planarity does not compromise the validity of the angle check procedure. The test also gave us the opportunity to estimate the cold mass torsional stiffness that, because of the compound cross-section structure, is not analytically deductible.

In operative conditions the cold mass is hosted in the cryostat and it is not accessible any more for position adjustments. It is therefore extremely important to know how the cryostat can affect the cold mass mechanical behavior. As the behavior is strictly related to the boundary conditions, represented by the three cold mass/cryostat sliding interfaces, we set up a test to study the interface features. We studied the response of the cold mass, inside the cryostat, to transversal forces applied at the extremities. Through comparison with the 3D finite element model we concluded that the expected sliding of the central foot (not directly observable) was never activated in the range of the applied forces. We computed the friction

coefficient at the central foot base and we obtained a value two times bigger than the expected one; hence we suggested organizing specific tests to evaluate the effective friction coefficient of the sliding interfaces. We used test data to define an equivalent transversal stiffness of the cold mass extremities, useful to analytically model the interaction between adjacent cryo-dipoles.

To guarantee a safe cryo-dipole road transport from the cryostating facility to the storage area and then to the tunnel, special transport restraints have been designed. Facing the need of a back-up solution to overcome a production delay of the nominal transport restraints, we used the complete cryo-dipole finite element model to compare the performances of alternative restraints. For each restraint type we evaluated the effect of the maximum accelerations, along the three axes, allowed during transport and handling. We compared the results in term of cold mass displacements and deformations, central composite support deformation and stress distribution inside the restraint structures. We also studied the effect of the differential thermal expansion between cryostat and cold mass as the one foreseen during outdoor long-term storage. We found that the proposed alternatives allow loads on central foot and stresses in the restraints that can, in some cases, exceed safety limits. We also found critical loads on central foot associated to ideal, very rigid transport restraints. We therefore suggested reconsidering transport specifications to decrease some of the maximum allowed accelerations.

The geometry of the cold mass inside the cryostat must be guaranteed for the whole life of the accelerator that is, at least, 20 years. Hence we investigated the effects of nominal and accidental operative circumstances on the geometry and position of the cold mass inside the cryostat. The nominal operative modes that we studied are: the Energization phase, the cool-down from ambient temperature to the operative 1.8 K and the warm-up to return to the ambient temperature. The most important accidental circumstance is the resistive transition (Quench) provoked by micro-movements of the superconductors induced by electromagnetic forces. To detect cold mass movements and deformations we used a device based on optical interferometry and specifically developed at CERN. We equipped, with 17 optical sensors, three out of the six dipoles composing the LHC full-cell full scale working prototype built at CERN. We acquired data during several months of nominal and non-nominal operating modes, run to test cryogenic, electrical and vacuum LHC systems.

We observed that the deformations of the cold mass induced by Energization are small, reproducible and directly related to the current density in the coils.

Greater but yet reproducible deformations are associated to Quench; they are induced by thermal phenomena and are completely recovered only after the cold mass thermal stabilization that can take up to six hours. We studied the potential criticalness of such deformations in terms of integrity of crucial components as the central composite support. From the measured extremity displacements we derived the loads induced on the support according to two different scenarios, none of which

was found dangerous.

We observed that during the thermal transients, needed to reach the operating temperature of 1.9 K, the cold mass extremities can experience large lateral displacements. However the maximum amplitude varies considerably from magnet to magnet and the average is not critical. Transient displacements are completely recovered after the thermal stabilization of the cold mass, hence the original geometry is preserved.

During Energization the arising Lorentz forces can provoke deformations of the coil cross-section and consequent field quality downgrading, detrimental for particle beam survival. We computed with a 2D finite element model the cross-section deformations induced by electromagnetic forces and we compared them with the cold mass diameter variation acquired during energization. We found a very good match between predicted and measured deformation.

Part IV

APPENDICES

Appendix A

Analytic beam model.

Under the assumption of homogeneous and continuous thin beam we can consider the cold mass deformed shape $v(x)$ as a continuous function of the bending moment along the axis $M_b(x)$. Since we neglect any cross-talk between forces and deformations in vertical and horizontal planes we can reduce the system to two dimensions. We can therefore study vertical plane and horizontal plane separately using the same 2D model hereby described.

In a homogeneous and continuous thin beam, initially straight, the deformation comes only from the rise of a curvature $\frac{d^2v(x)}{dx^2}$ induced by the bending moment $M_b(x)$ (in fact the effects of shear stress, introducing the shear deformation $\frac{dv(x)}{dx}$, are neglected). The curvature induced by a bending moment $M_b(x)$ is given by the relation:

$$\frac{d^2v(x)}{dx^2} = \frac{M_b(x)}{EI} \quad (\text{A.1})$$

where EI is the bending stiffness (E = Young's modulus [MPa], I = moment of inertia [m^4]). Previous equation can be derived by imposing the equilibrium between internal stress and external forces, the congruence of deformations and displacements and the elastic relation between stress and strain as explained in mechanic books [49].

By integrating eq. A.1 and imposing the boundary conditions (external forces and constraints) we obtain the polynomial expression of the deformed shape:

$$v(x) = ax^4 + bx^3 + cx^2 + dx + e \quad (\text{A.2})$$

that, in the most general case of both distributed and concentrated loads, is a 4th-order polynomial. In the domain of small deformations and displacements we can neglect non-linearities associated to material properties and to geometric degenerations. We can therefore use the superposition effect and consider the deformation $v(x)$ as the sum of the deformations individually induced by the different loads. This means that each polynomial coefficient of eq. A.2 contains the sum of the contributions of the different mechanical loads (distributed and/or concentrated forces and/or moments).

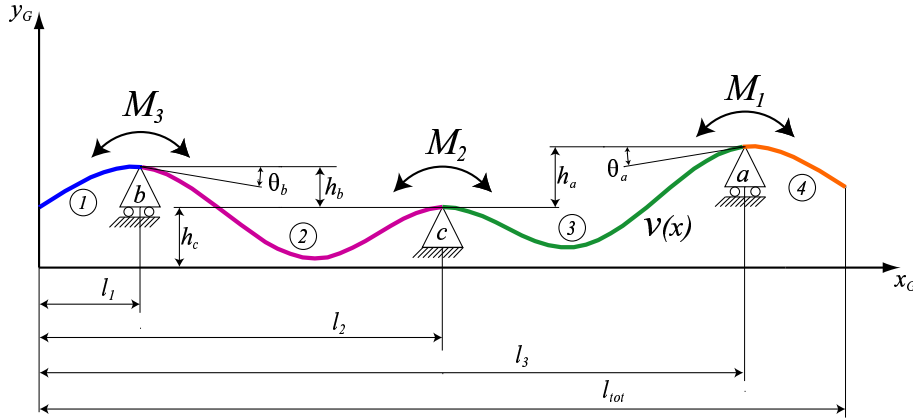


Figure A.1: Thin beam model of cold mass on three supports. Model is composed of four beams.

As already explained in 3.2 we consider the cold mass on three supports as a system of four beams rigidly connected as shown in Fig. A.1. We can therefore study each beam individually, taking in to account that they transmit each other the bending moments M_1 , M_2 and M_3 shown in Fig. A.1. The deformed shape of each beam is given by a polynomial curve identical to eq. A.2 (v_{Li} , $i=1,\dots,4$) here we provide the coefficients for all the polynomials. In this appendix we consider loads and deformations in the vertical plane, however the equations that we present are valid for the horizontal plane as well.

The mechanic loads on the cold mass that we consider are shown in Fig. A.2: a longitudinally distributed vertical force q_g [N/m], a vertical force F_{cc} [N] and a bending moment M_{cc} [Nm] concentrated at the Connection extremity, and a vertical force F_{nc} [N] and a bending moment M_{nc} [Nm] concentrated at the Non-Connection extremity.

In Table A.1 we give the polynomial coefficients divided by outer beams (n. 1 and 4) and inner beams (n. 2 and 3). With these coefficients each polynomial curve (v_{Li} , $i=1,\dots,4$) represents the deformed shape of each beam in the local reference system (x_{Li}, y_{Li} , $i=1,\dots,4$, shown in Fig. A.2). The coefficients of each beam are function of the beam length l , of the flexural rigidity EI , of the distributed load q and of the concentrated loads F_0, M_0, F_L and M_L applied at $x_L = 0$ and $x_L = l$.

For the inner beams (as the one shown in Fig. A.3, left) the moments at the extremities F_0, M_L represent the internal moments transmitted by the adjacent beams whereas forces at the extremities are zero because of constraint reactions. Internal moment expressions are given in Table A.3 as function of beam lengths and external loads. For the outer beams (Fig. A.3) the moment and the force concentrated at $x_L = 0$ are zero because of constraint reactions. Expression of specific loads on each beam are given in Table A.2.

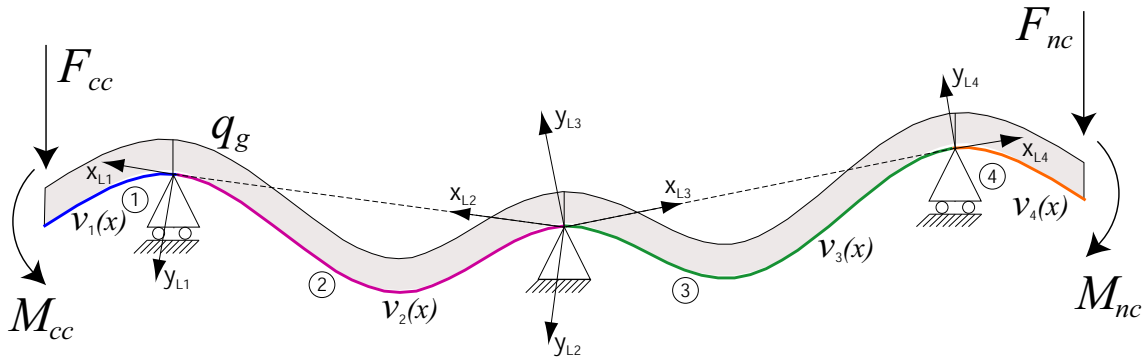


Figure A.2: Distributed and concentrated loads in the vertical plane. Local reference system of each beam is also shown.

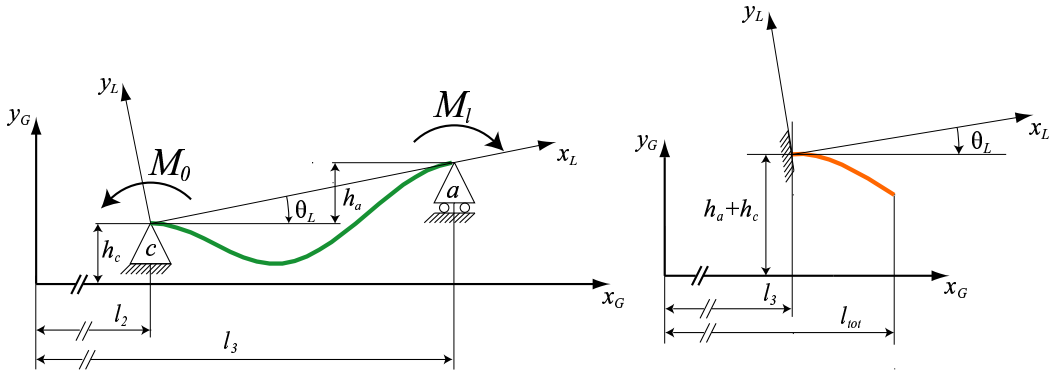


Figure A.3: Right inner beam (n. 3).

Table A.1: Polynomial coefficients for outer beams (n. 1 and 4) and inner beams (n. 2 and 3). Contributions of distributed force q , concentrated force F and moment M are given separately. Specific expressions of q , F and M are given in Table A.2.

Outer beams.				Inner beams.			
	q	F	M		q	F	M
a	$\frac{-q}{24EI}$	0	0	a	$\frac{-q}{24EI}$	0	0
b	$a \cdot 4l$	$\frac{-F_l}{6EI}$	0	b	$\frac{-ql}{12EI}$	0	$\frac{M_0 - M_l}{6EI}$
c	$a \cdot 6l^2$	$\frac{-F_l l}{2EI}$	$\frac{M_l}{2EI}$	c	0	0	$\frac{M_0}{2EI}$
d	0	0	0	d	$\frac{ql^3}{24EI}$	0	$(\frac{M_0}{3} + \frac{M_l}{6}) \frac{l}{EI}$
e	0	0	0	e	0	0	0

To obtain the cold mass deformation we must transform the curves v_{Li} , referred to the local reference system of each beam (x_{Li}, y_{Li} , $i=1, \dots, 4$, shown in Fig. A.2) to the global reference system (x_G, y_G). This is done through the coordinate transformation:

$$\begin{bmatrix} x_G \\ y_G \end{bmatrix} = \begin{bmatrix} \cos(\theta_L) & \sin(\theta_L) \\ -\sin(\theta_L) & \cos(\theta_L) \end{bmatrix} \begin{bmatrix} x_L - x_{GL} \\ y_L - y_{GL} \end{bmatrix} \quad (\text{A.3})$$

where (x_{GL}, y_{GL}) is the origin of the global reference system in local coordinates and θ_L is the rotation *from* the local *to* the global reference system (θ_L in Fig. A.3 is negative). Since we rather know the origin of the local reference system in global coordinates (that is: x_{LG}, y_{LG}) we can rewrite eq. A.3 and obtain:

$$\begin{bmatrix} x_G \\ y_G \end{bmatrix} = \begin{bmatrix} \cos(\theta_L) & \sin(\theta_L) \\ -\sin(\theta_L) & \cos(\theta_L) \end{bmatrix} \begin{bmatrix} x_L \\ y_L \end{bmatrix} + \begin{bmatrix} x_{LG} \\ y_{LG} \end{bmatrix} \quad (\text{A.4})$$

As θ_L is generally very small we can make the following two assumptions: 1) External vertical forces (F_{cc} , F_{nc} and q) are considered parallel to the local y -axis (according to local reference systems both distributed and concentrated loads for beams 1 and 2 in Fig. A.2 are negative). 2) Each beam length corresponds to its projection on the global x axis (as reported in Table A.2, 2nd column). Expressions of θ_L, x_{LG}, y_{LG} for each beam are given in Table A.4.

Table A.2: Specific parameters of beams.

Beam	l	q	F_0	F_l	M_0	M_l
1	l_1	$-q_g$	0	$-F_{cc}$	0	$-M_{cc}$
2	$l_2 - l_1$	$-q_g$	0	0	M_2	M_3
3	$l_3 - l_2$	q_g	0	0	M_2	M_1
4	$l_{tot} - l_1$	q_g	0	F_{nc}	0	M_{nc}

The model above described is used in several application at CERN to predict or understand elastic deformations of the cold mass. Even if in our assumptions we neglected the effect of shear, its contribution can be easily added to the coefficients of each beam. The real limit is represented by the assumption of rigid supports. The elasticity of the composite material supports should be taken into account when studying the effect of transversal loads on the cold mass installed in the cryostat.

Table A.3: Internal moments exchanged between adjacent beams.

M_1	$\frac{-ql_1^2}{2} - F_{cc}l_1 - M_{cc}$
M_2	$\frac{-3}{(l_3-l_1)}(\frac{M_1(l_2-l_1)-M_3(l_3-l_2)}{6} + \frac{q}{24}((l_3-l_2)^3 + (l_2-l_1)^3) - EI(\frac{h_a}{l_3-l_2} + \frac{h_b}{l_2-l_1}))$
M_3	$\frac{-q(l_{tot}-l_3)^2}{2} - F_{nc}(l_{tot}-l_3) - M_{nc}$

Table A.4: Parameters for local to global coordinate transformation.

Beam	$tg(\theta)$	x_{LG}	y_{LG}
1	$v'_{2G}(l_1)$	l_1	$h_c + h_b$
2	$h_b/(l_2 - l_3)$	l_2	h_c
3	$h_a/(l_3 - l_2)$	l_2	h_c
4	$v'_{3G}(l_3)$	l_3	$h_c + h_a$

To correctly implement the supports and to override the assumption of no cross-talk between vertical and horizontal plane still with a light model that can be included in routines and macro interfaced to the database, we implemented a 3D beam model based on finite element method.

Appendix B

Custom finite element model

The aim of this appendix is to provide an operative example on how to approach and implement the different steps involved in the application of the finite element method. It is focused on the implementation of a 3D beam model as the one used for the cold mass. Model is linear that is material properties do not depends on stress and deformations are small. The main advantage of not using a commercial finite element code is the possibility to include the model in routines embedded in data analysis softwares as it was done with the analytical model. The reader should already be familiar with the finite element method basic principles. The following topics are covered:

- element definition
- element stiffness matrix
- nodes location
- element nodal connectivity
- local to global conversion
- assembly of global stiffness matrix
- nodal constraints and nodal forces
- distributed forces
- nodal solution
- element solution

B.1 Element definition

The element is a 3D beam with 12 d.o.f. (6 per node) as shown in Fig B.1, the x -axis goes from node 1 to node 2. In each node three translations and three rotations are allowed, respectively along and around the three nodal axes.

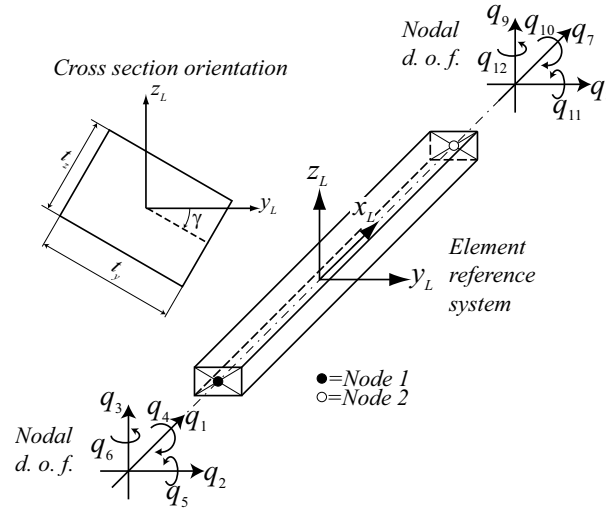


Figure B.1: 3D beam.

Beam material is elastic and isotropic. Material properties to be specified are: Young's modulus E , Poisson's ratio ν and tangential elasticity G . Material properties can be stored in an array of data structures with one field per property. Each component of the array identifies one material.

The beam element are characterized by the following geometric properties (Fig B.1): Cross sectional Area A , Thickness along y and z directions: t_y , t_z , cross section orientation γ . Moment of inertia around y and z axes: I_y and I_z , torsional moment of inertia around x axis: J . Shear coefficients (ratio between cross sectional area and the Shear Area normal to y and z directions): sh_y and sh_z . Geometric properties can be stored in an array of data structures with one field per property. Each components of the array identifies a group of beams with the same geometric properties.

B.2 Node locations

The coordinates of the n nodes can be stored in a $3 \times n$ table ('node table') in which each row corresponds to a node and the three columns to the three cartesian coordinates. It must be pointed out that in the case of straight beams the accuracy of the solution is independent from the level of discretization (that is the number of elements and nodes). In the cold mass model the number of elements required is only 10 (i.e. 11 nodes). As shown in Fig. B.2 three beams are needed to model the

three composite supports, four beams are needed to model the cold mass and finally three beams are needed to bridge the supports to the cold mass axis where the cold mass nodes lie. In case of few nodes (11 in the cold mass model) the coordinates can be entered manually, otherwise it is convenient to write a dedicated routine to divide the geometry in a number of regions (multi-dimensional interpolation).

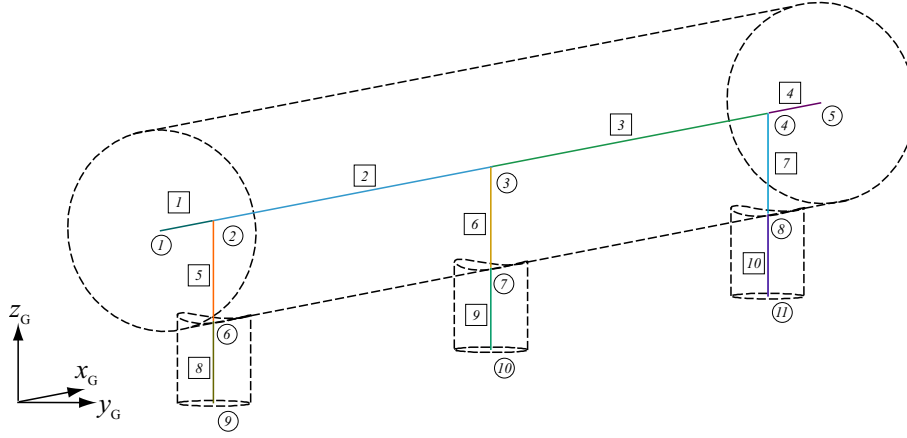


Figure B.2: Discretization of cold mass by 10 beams and 11 nodes (numbered in squares and circles , respectively).

B.3 Element nodal connectivity

Each beam element is characterized by the two nodes to which it is connected and the material and geometric properties group to which it belongs. It can be convenient to create a $m \times 4$ table ('element table', m is the total number of elements) in which for each element the first two columns contain the node numbers, the third contains the material properties group and the fourth the geometric properties group.

B.4 Element stiffness matrix

The stiffness matrix relates the forces and moments (generally called loads), applied to any node, to the displacements and rotations (generally called displacements) induced on all the nodes. Such a matrix is always square and symmetric with dimensions equal to the total number of d.o.f. of the element (i.e. 12 for the 3D beam). It depends on the material and geometric properties described above. The term ij (at the intersection of the i^{th} row with the j^{th} column) corresponds to the force (or moment) applied on the i^{th} d.o.f that produces a unitary change along the j^{th} d.o.f. (displacement or rotation). Operatively term ij can be computed as the constraint reaction along the i^{th} d.o.f. when a unitary change is applied along the j^{th} d.o.f. *and* all the other d.o.f. are constrained. Here is reported the 3D beam stiffness matrix as defined in [50]

$$[\mathbf{K}] = \begin{bmatrix}
\frac{AE}{L} & & & & & & & & & & \\
0 & \frac{12EI_z}{L^3(1+\Phi_y)} & & & & & & & & & \\
0 & 0 & \frac{12EI_y}{L^3(1+\Phi_z)} & & & & & & & & \\
0 & 0 & 0 & \frac{GJ}{L} & & & & & & & \\
0 & 0 & \frac{6EI_y}{L^2(1+\Phi_z)} & 0 & \frac{(4+\Phi_z)EI_y}{L(1+\Phi_z)} & & & & & & \\
0 & \frac{6EI_z}{L^2(1+\Phi_y)} & 0 & 0 & 0 & \frac{(4+\Phi_y)EI_z}{L(1+\Phi_y)} & & & & & \\
-\frac{AE}{L} & 0 & 0 & 0 & 0 & 0 & \frac{AE}{L} & & & & \\
0 & \frac{-12EI_z}{L^3(1+\Phi_y)} & 0 & 0 & 0 & \frac{6EI_z}{L^2(1+\Phi_y)} & 0 & \frac{12EI_z}{L^3(1+\Phi_y)} & & & \\
0 & 0 & \frac{-12EI_y}{L^3(1+\Phi_z)} & 0 & \frac{6EI_y}{L^2(1+\Phi_z)} & 0 & 0 & 0 & \frac{12EI_y}{L^3(1+\Phi_z)} & & \\
0 & 0 & 0 & \frac{-GJ}{L} & 0 & 0 & 0 & 0 & 0 & \frac{GJ}{L} & \\
0 & 0 & \frac{-6EI_y}{L^2(1+\Phi_z)} & 0 & \frac{(2-\Phi_z)EI_y}{L(1+\Phi_z)} & 0 & 0 & \frac{6EI_y}{L^2(1+\Phi_z)} & 0 & \frac{(4+\Phi_z)EI_y}{L(1+\Phi_z)} & \\
0 & \frac{6EI_z}{L^2(1+\Phi_y)} & 0 & 0 & 0 & \frac{(2-\Phi_y)EI_z}{L(1+\Phi_y)} & 0 & \frac{-6EI_z}{L^2(1+\Phi_y)} & 0 & 0 & \frac{(4+\Phi_y)EI_z}{L(1+\Phi_y)}
\end{bmatrix} \quad (\text{B.1})$$

where: $\Phi_y = \frac{12EI_z sh_z}{GAL^2}$ and $\Phi_z = \frac{12EI_y sh_y}{GAL^2}$.
 Previous matrix $[K]$ satisfies the equation

$$\{f\} = [k]\{q\} \quad (\text{B.2})$$

where the force vector f and the nodal displacements q are expressed in the local reference system of the element (shown in Fig. B.1).

Before assembling the global stiffness matrix, all the element matrices must be transformed to satisfy eq. B.2 expressed in terms of the global forces F and displacements Q :

$$\{F\} = [K]\{Q\}. \quad (\text{B.3})$$

B.5 From local to global

If $[T]$ is the transformation matrix from global to local coordinates (only function of element orientation) one can write:

$$\{f\} = [T]\{F\} \quad (\text{B.4})$$

$$\text{and: } \{q\} = [T]\{Q\} \quad (\text{B.5})$$

$$\text{that is: } \{F\} = [T]^{-1}\{f\} \quad (\text{B.6})$$

$$\text{and: } \{Q\} = [T]^{-1}\{q\} \quad (\text{B.7})$$

Substituting eq. B.5 in B.2 and the result in B.6:

$$\{F\} = [T]^{-1}[k][T]\{q\} \quad (\text{B.8})$$

As the transformation matrix $[T]$ is, by definition, orthogonal: $[T]^{-1} = [T]^T$ and the element stiffness matrix in global coordinates can be written as:

$$\{K\} = [T]\{k\}[T]^T \quad (\text{B.9})$$

The general transformation matrix in 3D can be written as the product of the three 2D rotation matrices around the *current* z, y and x -axes (*current* means that the 2^{nd} rotation is around the y -axis resulting from 1^{st} rotation; 3^{rd} rotation is around the x -axis resulting from 1^{st} and 2^{nd} rotations). First rotation of α radians around z -axis gives matrix:

$$[R_\alpha] = \begin{bmatrix} \cos(\alpha) & \sin(\alpha) & 0 \\ -\sin(\alpha) & \cos(\alpha) & 0 \\ 0 & 0 & 1 \end{bmatrix} \quad (\text{B.10})$$

the second rotation, β radians around y -axis, gives:

$$[R_\beta] = \begin{bmatrix} \cos(\beta) & 0 & \sin(\beta) \\ 0 & 1 & 0 \\ -\sin(\beta) & 0 & \cos(\beta) \end{bmatrix} \quad (\text{B.11})$$

the third rotation, γ radians around x -axis, gives:

$$[R_\gamma] = \begin{bmatrix} 1 & 0 & 0 \\ 0 & \cos(\gamma) & \sin(\gamma) \\ 0 & -\sin(\gamma) & \cos(\gamma) \end{bmatrix} \quad (\text{B.12})$$

The three angles α, β and γ are given respectively by:

$$\alpha = \text{asin}\left(\frac{y_1 - y_2}{L}\right) \quad (\text{B.13})$$

$$\beta = \text{asin}\left(\frac{z_2 - z_1}{L}\right) \quad (\text{B.14})$$

$$\gamma = \text{cross section orientation given as input.} \quad (\text{B.15})$$

$$(\text{B.16})$$

where L is the beam length, y_i and z_i the coordinates of node i ($i=1,2$). The 3D transformation matrix $M = R_\alpha R_\beta R_\gamma$ is:

$$[M] = \begin{bmatrix} c_\alpha c_\beta & -s_\alpha c_\beta & s_\beta \\ s_\alpha c_\gamma + c_\alpha s_\beta s_\gamma & c_\alpha c_\gamma - s_\alpha s_\beta s_\gamma & -c_\beta s_\gamma \\ s_\alpha s_\gamma - c_\alpha s_\beta c_\gamma & c_\alpha s_\gamma + s_\alpha s_\beta c_\gamma & c_\beta c_\gamma \end{bmatrix} \quad (\text{B.17})$$

where $c_\alpha = \cos(\alpha)$, $s_\alpha = \sin(\alpha)$, etc...

The matrix $[T]$ needed to transform all the local d.o.f. of the 3D beam element (12 d.o.f.) is:

$$[T] = \begin{bmatrix} [M] & \bar{0} & \bar{0} & \bar{0} \\ \bar{0} & [M] & \bar{0} & \bar{0} \\ \bar{0} & \bar{0} & [M] & \bar{0} \\ \bar{0} & \bar{0} & \bar{0} & [M] \end{bmatrix} \quad (\text{B.18})$$

where $\bar{0}$ are 3x3 null matrices.

B.6 Assembly of global stiffness matrix

The global stiffness matrix is composed by all the element matrices combined accordingly to the nodal connectivity. Each element matrix can be subdivided into four sub-matrices, K_{ij} ($i, j=1,2$) that relates forces and moments on node i to displacements and rotations of node j . The number of sub-matrices depends on the number of nodes connected to the element whereas the size of the sub-matrices depends on the number of degrees of freedom (d.o.f.) of each node. An example is given with respect to the system depicted in Fig. B.3 and composed by four beams and four nodes. The four element matrices, already expressed in global coordinates, are divided in sub-matrices K_{ij}^m (where superscript m is the element number) and then combined together to form the global stiffness matrix K^G .

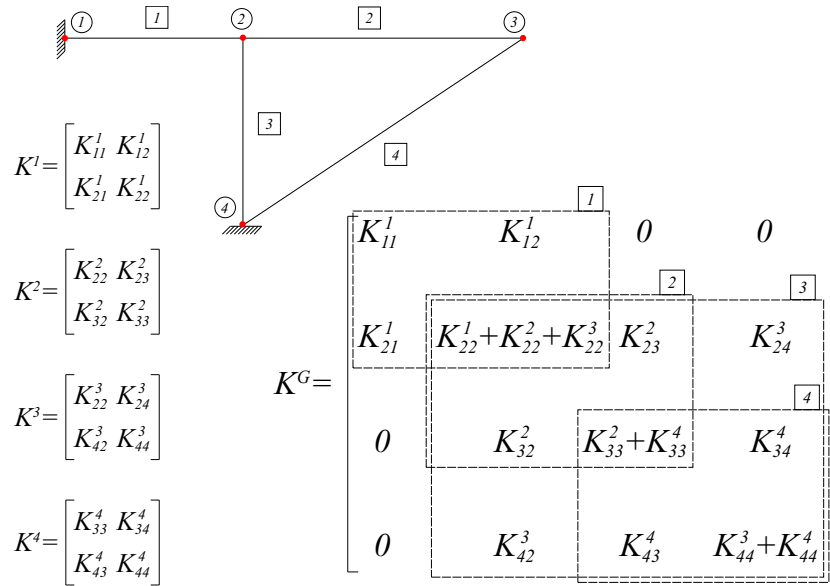


Figure B.3: System of four elements and four nodes (numbered in squares and circles, respectively). Element stiffness matrices are assembled together to form the global stiffness matrix.

Operatively the global stiffness matrix is built up by a routine that, for each node, looks up in the element table the elements connected, for each one of the connected elements it builds the element stiffness matrix k (function of geometry and material groups indicated in the element table) and the transformation matrix T function of element orientation. It computes the element stiffness matrices in global coordinates of all the element connected to the node and it sums them as shown in Fig. B.3.

B.7 Concentrated loads and constraints

Once that the global stiffness matrix is assembled, the structural problem is described by the equation:

$$\{F^G\} = [K^G]\{Q^G\} \quad (\text{B.19})$$

In which F^G is the vector (known) that contains all the forces applied along each d.o.f. of each node and Q^G is the vector (unknown) that contains all the displacements along each d.o.f. of each node. In the cold mass model the length of the vectors is 66 (11 nodes, 6 d.o.f. each) and $[K^G]$ is obviously 66x66. *From now on 'G' in F^G , K^G and Q^G will be omitted as these vectors refer to the global system and not to a single element unless specified.*

The system of equations represented by eq. B.19 cannot be directly solved because $[K]$ is singular. The singularity is due to the fact that different elements are connected to the same nodes and share therefore some d.o.f., with the result that some of the equations in the system are coupled (physically it corresponds to a structure statically undetermined). To solve the system it is necessary to reduce the number of unknowns (physically it corresponds to constraining a sufficient number of d.o.f. and operatively to assigning values to some of the unknowns of Q).

The constraint Q_i^* (for example a zero displacement on the i^{th} d.o.f.) on the degree of freedom i can be applied by modifying the global stiffness matrix K and the global force vector F in the following way

- assign value 0 to all the elements in the i^{th} row and i^{th} column
- assign value 1 to K_{ii} (intersection of i^{th} row and i^{th} column)
- assign value q_i^* to the element F_i
- assign to all the other elements of F the value $F_j - K_{ij}Q_i^*$ (with $i \neq j$)

After the constraining of the i^{th} d.o.f by Q_i^* , system B.19 will look like:

$$\begin{pmatrix} F_1 - K_{1i}Q_i^* \\ F_2 - K_{2i}Q_i^* \\ \vdots \\ F_{i-1} - K_{i-1,i}Q_i^* \\ Q_i^* \\ F_{i+1} - K_{i+1,i}Q_i^* \\ \vdots \\ F_n - K_{ni}Q_i^* \end{pmatrix} = \begin{bmatrix} K_{11} & K_{12} & \cdots & K_{1i-1} & 0 & K_{1i+1} & \cdots & K_{1n} \\ K_{21} & K_{22} & \cdots & K_{2i-1} & 0 & K_{2i+1} & \cdots & K_{2n} \\ \vdots & \vdots & \ddots & \vdots & \vdots & \vdots & \vdots & \vdots \\ K_{i-1,1} & K_{i-1,2} & \cdots & K_{i-1,i-1} & 0 & K_{i-1,i+1} & \cdots & K_{i-1,n} \\ 0 & 0 & \cdots & 0 & 1 & 0 & \cdots & 0 \\ K_{i+1,1} & K_{i+1,2} & \cdots & K_{i+1,i-1} & 0 & K_{i+1,i+1} & \cdots & K_{i+1,n} \\ \vdots & \vdots & \vdots & \vdots & \vdots & \vdots & \ddots & \vdots \\ K_{n1} & K_{n2} & \cdots & K_{ni-1} & 0 & K_{ni+1} & \cdots & K_{nn} \end{bmatrix} \begin{pmatrix} Q_1 \\ Q_2 \\ \vdots \\ Q_{i-1} \\ Q_i \\ Q_{i+1} \\ \vdots \\ Q_n \end{pmatrix} \quad (\text{B.20})$$

It is evident that the i^{th} equation of the system gives $Q_i = Q_i^*$ that corresponds the imposed displacement whereas all the other equations are unaffected. It is worth to remember that the system has been discretized to a finite number of nodes. Therefore constraints and loads can be only applied to nodes and the solution of eq. F.7 will give the nodal displacements.

The application of loads on the nodes is straightforward: the values, in the global coordinate system, can be directly entered in vector F . As vector F can contain only loads concentrated in the nodes, to apply loads that are concentrated elsewhere or distributed along the beam length, it is necessary to compute the equivalent nodal loads. The equivalent nodal loads of an element loaded by a given load distribution correspond to the constraint reactions when the element is load with the given distribution and constrained in all d.o.f.. The following example shows how to compute the nodal loads equivalent to a force uniformly distributed along the length (it is used to implement the gravity in the cold mass model). Fig. F.7, left, shows the beam element loaded by a vertical force uniformly distributed. The system is statically undetermined, it can be solved by applying the force method and by taking advantage of symmetries. Constraint reaction values are given in Fig. F.7, right. Out of the 12 reactions only the four shown have a finite value.

The general vector of forces for one beam element, in the local coordinate system,

is thus given by:

$$\{f\} = \begin{pmatrix} f_1 \\ f_2 + \frac{p_1 l}{2} \\ f_3 + \frac{p_2 l}{2} \\ f_4 \\ f_5 - \frac{p_1 l^2}{12} \\ f_6 + \frac{p_2 l^2}{12} \\ f_7 \\ f_8 + \frac{p_1 l}{2} \\ f_9 + \frac{p_2 l}{2} \\ f_{10} \\ f_{11} + \frac{p_1 l^2}{12} \\ f_{12} - \frac{p_2 l^2}{12} \end{pmatrix} \quad (\text{B.21})$$

where p_1 and p_2 are the force per unit length along y_L and z_L , respectively.

B.8 Nodal solution

Once that the system is sufficiently constrained the global stiffness matrix is normal and can be inverted so that the global displacement vector is obtained from:

$$\{Q\} = [K]^{-1} \{F\} \quad (\text{B.22})$$

Vector $\{Q\}$ contains the displacements and rotations of all the nodes in the system and can be used to derive stresses and deformation inside the elements.

B.9 Element solution

The cold mass beam model has been implemented to analyze the 3D elastic deformations induced by boundary conditions as external loads or constraints. Equivalent beam stresses do not have a direct physical meaning and their evaluation is not covered in this appendix.

In case of 3D beams there are four kinds of deformations, all described by polynomials in the element reference system:

- elongation along x_L -axis:

$$u(x_L) = a_u x_L + b_u \quad (\text{B.23})$$

- flexion in (x_L, y_L) plane:

$$v(x_L) = a_v x^4 + b_v x^3 + c_v x^2 + d_v x + e \quad (\text{B.24})$$

- flexion in (x_L, z_L) plane:

$$w(x_L) = a_w x^4 + b_w x^3 + c_w x^2 + d_w x + e \quad (\text{B.25})$$

- torsion around x_L -axis:

$$t(x_L) = a_t x + b_t \quad (\text{B.26})$$

all the polynomials coefficients can be easily found by imposing the boundary conditions represented by nodal displacements in the element reference system.

Appendix C

Azimuthal pre-stress in the shrinking cylinder

In this appendix we will show how we implemented the azimuthal pre-stress in the shrinking cylinder by using fictitious thermal expansion coefficients. A common way to implement pre-stress within the finite element method exploits differential thermal contractions between adjacent components. The pre-stress value then is triggered by setting the appropriate temperature and thermal expansion coefficient values. The concept is clear if we look at the thermal contraction induced by a temperature variation:

$$\epsilon_{\Delta t} = \alpha \Delta t \quad (\text{C.1})$$

where: $\epsilon_{\Delta t}$ is the strain induced by the temperature variation Δt and α is the thermal expansion coefficient. The stress in the material then arises if the $\epsilon_{\Delta t}$ is partially or totally constrained. If ϵ_f is the allowed deformation, the consequent stress will be:

$$\sigma = E(\epsilon_{\Delta t} - \epsilon_f) \quad (\text{C.2})$$

Where E is the material Young's modulus. To find a suitable thermal expansion coefficient for the shrinking cylinder to induce the 150 MPa azimuthal pre-stress we must study the stress distribution inside a cold mass cross-section. In Fig. C we can see an equivalent system where the collar and the yoke are represented as a single material surrounded by the shrinking cylinder. The final pre-stress in the shrinking cylinder will be given by the balance between the radial outward forces exercised by the inner material and the inward forces by the shrinking cylinder. In our 2D system we consider a plane stress state so that the active stress components lie in the section plane. In polar co-ordinate the congruence equation becomes:

$$\epsilon_r = u_{r,r} \quad (\text{C.3})$$

$$\epsilon_\theta = \frac{1}{r}(u_r + u_{\theta,\theta}) \quad (\text{C.4})$$

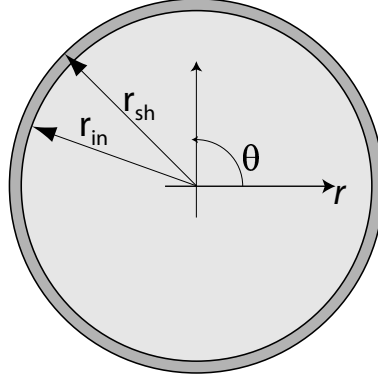


Figure C.1: Equivalent system to model the stress distribution in the cold mass cross-section.

$$\epsilon_{r,\theta} = \frac{1}{2} \left(u_{\theta,r} - \frac{u_\theta}{r} + \frac{u_{r,\theta}}{r} \right) \quad (\text{C.5})$$

The constitutive equation for the linear elastic isotropic material in this 2D case with circular symmetry becomes:

$$\sigma_r = \frac{E_{in}}{(1 - \nu_{in}^2)} [\epsilon_r + \nu_{in} \epsilon_\theta] \quad (\text{C.6})$$

$$\sigma_\theta = \frac{E_{in}}{(1 - \nu_{in}^2)} [\epsilon_\theta + \nu_{in} \epsilon_r] \quad (\text{C.7})$$

The azimuthal stress $\sigma_{\theta_{sh}}$ in the shrinking cylinder will be given by:

$$\sigma_{\theta_{sh}} = E_{sh}(\epsilon_{\Delta t} - \epsilon_{in}) \quad (\text{C.8})$$

where: $\epsilon_{\Delta t}$ is the contraction induced by the temperature variation Δt in the shrinking cylinder considered by itself whereas ϵ_{in} is the contraction of the internal part under the radial pressure exercised by the shrinking cylinder action. In a thin walled vessel as the shrinking cylinder, the relation between the azimuthal stress and the radial pressure is:

$$p = \frac{\sigma_{\theta_{sh}} t}{r} \quad (\text{C.9})$$

where: t and r are the cylinder wall thickness and radius, respectively. At the equilibrium the pressure p is counteracted by the internal part and the corresponding radial stress on the surface is:

$$\sigma_{r_{in}} = \frac{\sigma_{\theta_{sh}} t}{r} \quad (\text{C.10})$$

In this particular case of plane stress with circular symmetry the stress distribution inside the body is uniform i.e.: $\sigma_{\theta_{in}} = \sigma_{r_{in}}$ and obviously $\epsilon_{\theta_{in}} = \epsilon_{r_{in}}$. From equations C.6 and C.7 we can thus write:

$$\epsilon_{\theta_{in}} = \frac{1}{E_{in}}(1 - \nu_{in})\sigma_{r_{in}} \quad (\text{C.11})$$

Taking in to account equations C.1, C.10, C.11 we can rewrite eq. C.8 as:

$$\sigma_{\theta_{sh}} = E_{sh}(\alpha\Delta t - \frac{1}{E_{in}}(1 - \nu)\frac{\sigma_{\theta_{sh}}t}{r}) \quad (\text{C.12})$$

and thus we obtain the thermal expansion coefficient α to assign to the shrinking cylinder in order to have the desired $\sigma_{\theta_{sh}}$ for a given Δt :

$$\alpha = \frac{\sigma_{\theta_{sh}}}{\Delta t}[\frac{1}{E_{sh}} + \frac{t}{E_{in}r}(1 - \nu)] \quad (\text{C.13})$$

At the equilibrium the shrinking cylinder will present an azimuthal contraction given by $\epsilon_{\Delta t} - \epsilon_{in}$; to avoid the arise of unwanted stresses all the components attached to the shrinking cylinder will need to endure the same contraction by mean of an adequate thermal expansion coefficient. Such a coefficient is easily obtained through the following equation:

$$\epsilon_{\Delta t} - \epsilon_{in} = \alpha_p \Delta t \quad (\text{C.14})$$

in which the left side represents the cylinder contraction whereas the right, where α_p is the expansion coefficient, represents the thermal contraction of the pad.

The procedure described so far concerns only the stresses and deformations in a cross-section of the magnet. To provide a homothetic shrinkage of the structure a suitable expansion coefficient in the longitudinal direction must be assigned to all the components. Such a longitudinal coefficient will be, for the pads, the same as the transversal one, whereas for the shrinking cylinder it will have to balance the longitudinal strain resulting from the transverse stresses accordingly to the Poisson's ratio. As the cylinder is a thin vessel we can assume the stress component in the section plane σ_r be negligible with respect to σ_θ so that the longitudinal (y-direction) strain is given by:

$$\epsilon_y = \frac{\sigma_{\theta_{sh}}}{\nu_{\theta y} E_{sh}} \quad (\text{C.15})$$

To cancel this strain we have to assign to the shrinking cylinder material a thermal expansion coefficient in the longitudinal direction α_{sh_y} such that:

$$\alpha_{sh_y} \Delta t = -\epsilon_y \quad (\text{C.16})$$

that is:

$$\alpha_{sh_y} = \frac{-\sigma_{\theta_{sh}}}{\nu_{\theta y} E_{sh} \Delta t} \quad (\text{C.17})$$

For yoke and collar materials we assigned, accordingly to the laminated structure properties, a Poisson's ratio close to zero so that no longitudinal strain is induced by the stress distribution in the transversal plane. The fictitious thermal expansion coefficients are summarized in Table C.1.

Table C.1: Fictitious thermal expansion coefficient used to implement the pre-stress exerted by the shrinking cylinder.

Component	α [1/K]		
	x (rad.)	y (long.)	z (azim.)
Sh. cylinder	-	-2.0625e-6	7.6875e-6
Collar	0	1.8750e-7	0
Yoke	0	1.8750e-7	0
Supp. posts		1.8750e-7	

Appendix D

Sag error computation

In this appendix we will show how the magnet axis data, given as deviations from the theoretical shape (see Chapter 4.2), can be conveniently interpolated by a second order polynomial curve to calculate the error on sagitta.

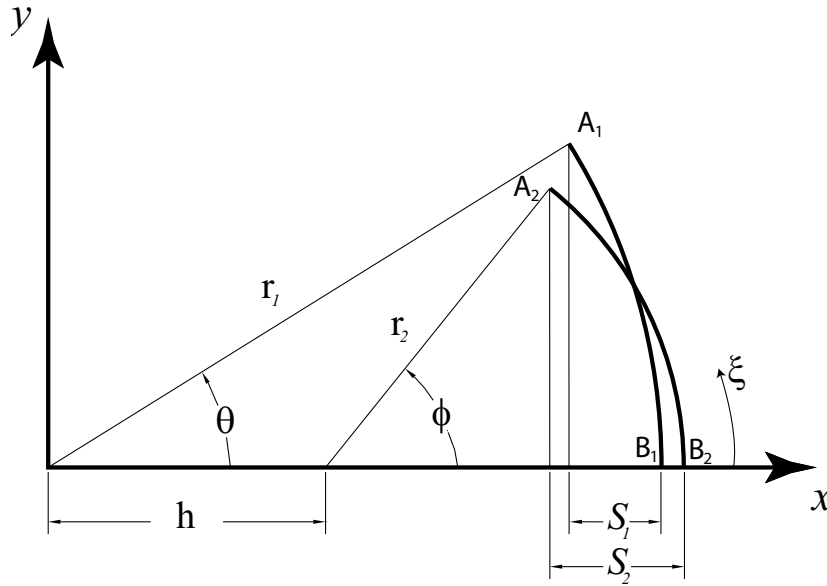


Figure D.1: Ideal representation of magnet axis shape in horizontal half plane. Arc 1 has nominal sagitta, Arc 2 bigger than nominal.

Looking at the horizontal half plane of Fig. D.1 we assume that arc 1 is (half of) the theoretical shape of the curved part of a dipole and arc 2 (half of) the best circular fit of the measured data in an aperture. The error on sagitta, that is the difference between the theoretical sagitta and the real one, is given by:

$$\Delta S_E = S_2 - S_1 \quad (\text{D.1})$$

where S_2 and S_1 are the sagittae of the arcs 1 and 2; we can write the same formula in the following way:

$$\Delta S_E = r_1(1 - \cos\theta_0) - r_2(1 - \cos\phi_0) \quad (\text{D.2})$$

where θ_0 and ϕ_0 are the half angles subtended by the curves 1 and 2. A more convenient way to write the sagitta error as a function of the displacements between curve 1 and 2 is:

$$\Delta S_E = (x_{A_1} - x_{A_2}) + (x_{B_2} - x_{B_1}) \quad (\text{D.3})$$

where the parentheses enclose the displacements of points a_2 and b_2 from the theoretical curve. The error on sagitta is thus the sagitta of the difference curve that is made by the difference between the the generic abscissa of each arc:

$$\begin{aligned} x_1 &= r_1 \cos \theta = r_1 \cos \frac{\xi}{r_1} \\ x_2 &= h + r_2 \cos \phi = h + r_2 \cos \frac{\xi}{r_2} \end{aligned}$$

with ξ the curvilinear abscissa that is $\xi = 0$ when $\theta, \phi = 0$. Since in our analysis the angle domain is restricted in few *mrad*, $\cos x$ can be approximated as:

$$\cos x = 1 - \frac{x^2}{2} + o(x^3). \quad (\text{D.4})$$

The generic difference between the abscissa x of the two curves for the same curvilinear abscissa ξ is consequently given by:

$$\Delta x = h + r_2 \cos \frac{\xi}{r_2} - r_1 \cos \frac{\xi}{r_1} = h + r_2 \left(1 - \frac{\xi^2}{2r_2^2}\right) - r_1 \left(1 - \frac{\xi^2}{2r_1^2}\right) = h + r_2 - r_1 + \frac{\xi^2}{2} \left(\frac{1}{r_1} - \frac{1}{r_2}\right) \quad (\text{D.5})$$

that is a 2^{nd} order polynomial. For this reason a 2^{nd} order polynomial interpolation can be conveniently used to fit the difference between the theoretical and the measured curved part of the dipole in order to estimate the relative error on the sagitta.

Appendix E

From extremity to central foot displacement.

In this appendix we show how we evaluated the possible central foot displacement corresponding to a measured cold mass extremity displacement. As first approximation we can consider, in the horizontal plane, the cryostat as infinitely rigid with respect to the system composed by the cold mass and the composite feet. We can also assume that the three feet have the same rigidity and that for small displacements the force/deformation relation is linear so that they can be approximated by horizontal springs connecting the cold mass and the cryostat as shown in the schematic drawing of Fig. E.1. A further assumption is to consider that the cold mass change of curvature can be approximated by a parabolic curve as explained in Appendix D. In the drawing of Fig. E.1, where the three springs represent the

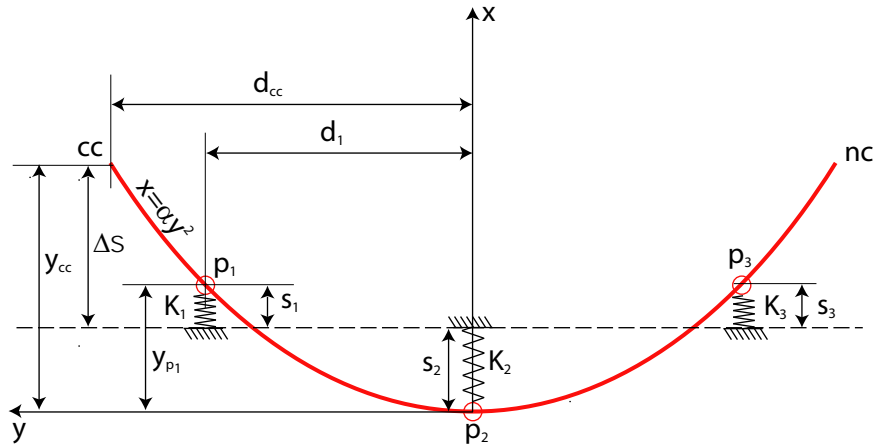


Figure E.1: Cold mass deformation associated to a curvature increase.

transversal elasticity of the supports that connect the cold mass (red line) to the cryostat (frame, dashed line), ΔS is the measured displacement of the cold mass

extremity and s_2 is the central foot displacement. As the points CC and p_1 belong to the curve $x = \alpha y^2$ we can write:

$$y_{cc} = \alpha d_{cc}^2 \quad (\text{E.1})$$

$$y_{p_1} = \alpha d_1^2 \quad (\text{E.2})$$

$$(\text{E.3})$$

Combining the two equations and substituting the values of d_1 and d_{cc} (5.4 m and 7.4 m, respectively) gives:

$$y_{cc} = 1.8779 y_{p_1} \quad (\text{E.4})$$

that is:

$$\Delta S + s_2 = 1.8779(s_1 + s_2) \quad (\text{E.5})$$

Now to know the relation between s_1 and s_2 it is sufficient to impose the equilibrium of the forces exerted by the three springs:

$$\vec{F}_1 + \vec{F}_2 + \vec{F}_3 = 0 \quad (\text{E.6})$$

that is:

$$K_1 s_1 - K_2 s_2 + K_3 s_3 = 0 \quad (\text{E.7})$$

and thus, since \vec{F}_1 and \vec{F}_2 are equal for symmetry reason and the three rigidities are equal for hypothesis:

$$s_2 = 2s_1 \quad (\text{E.8})$$

We can now rewrite eq. E.5 taking in to account eq. E.8:

$$\Delta S = (1.8779 * 1.5 - 1)s_2 \quad (\text{E.9})$$

that is:

$$s_2 = 0.55 \Delta S \quad (\text{E.10})$$

Appendix F

Screw modeling in transport restraints.

In this appendix we present the equivalent finite element model that we implemented to reproduce the screws that connect the light transport restraint to the cold mass. The need to model the screws comes from the position of the holes in the front plate i.e. critically close to the edge and to each other. The aim is to obtain a realistic distribution of stresses around the hole induced by the load transmitted by the screws. The transport restraint plate has threaded and smooth holes that host respectively headless set screws and bolts. The set screws transmit the loads from the cold mass to the restraint only by compression whereas the bolts, passing through the smooth holes and screwed in to the cold mass, transmit the loads uniquely by tension.

To implement this features in the ANSYSTM model we used element LINK10 (only compression/tension beams) in conjunction with BEAM4 to take into account screw bending. The connection between the beam representing the screw body and the hole on the restraint is implemented differently for the set screws and the bolts. To simulate the first three/four threads (that are the ones through which all the load is transmitted) of the set screws, we created two layers of radial beam arrays connecting the screw body, at the center, with each node along the hole perimeter at the corresponding layer level as can be seen in Fig. F.1 and in Fig. F.4. To simulate the pressure transmitted through the washer of the bolt to the circular corona on the external side of the restraint plate we created one layer of radial beams from the center of the bolt body to the two concentric ring of nodes of the plate closest to the hole edge (Fig.F.2). To allow realistic hole ovalizations we gave a small cross section area and a high flexural stiffness to all of the radial beams (Table F.1 and Table F.2).

The screw engagements on the cold mass side have been roughly modeled as the stress distribution on the cold mass is of negligible interest. To link each beam extremity to each corresponding tetrahedral solid element we created sets of eight trusses from the beam node to each corner node of the solid element as shown in

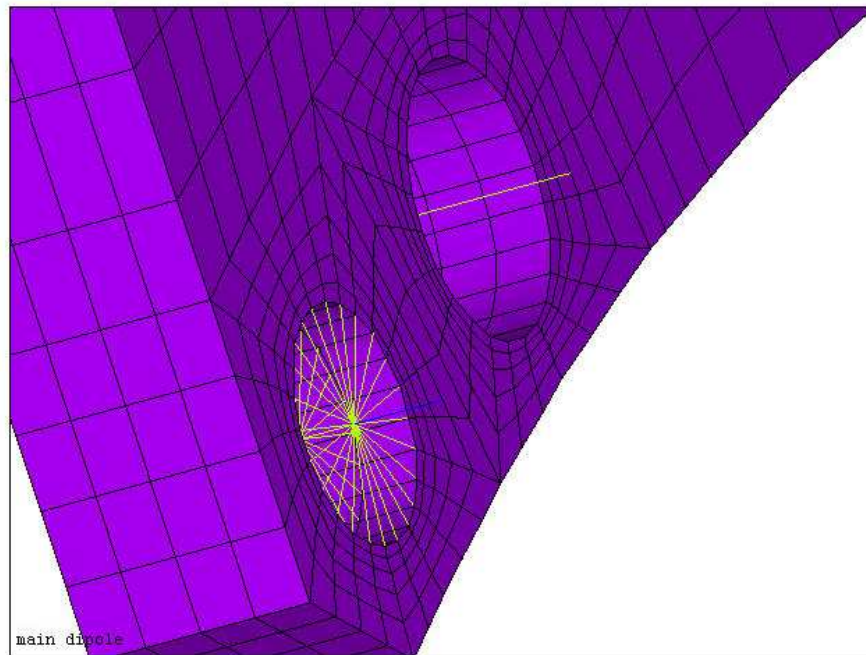


Figure F.1: Detail of setscrew model. Two layers of radial beams transmit the load to the hole walls as the first three/four threads in reality do.

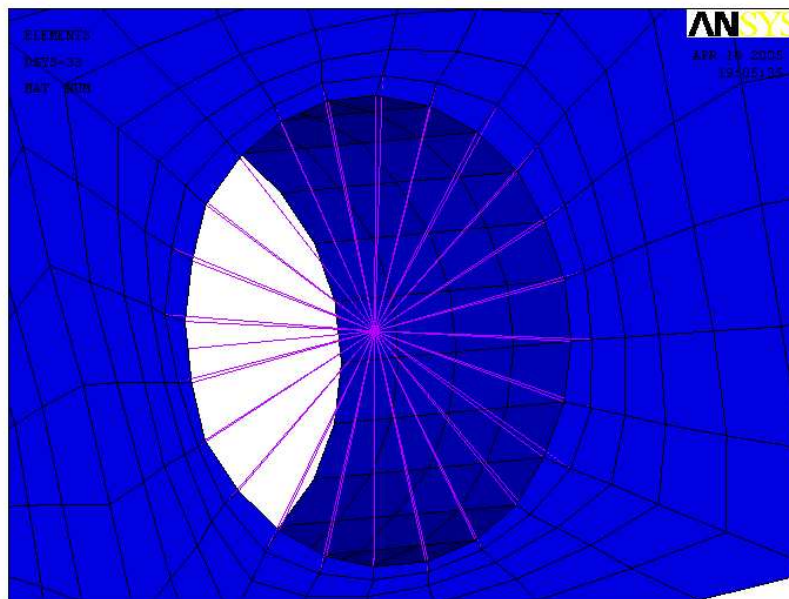


Figure F.2: Detail of bolt model. The radial beams transmit the load to a circular surface around the hole edge.

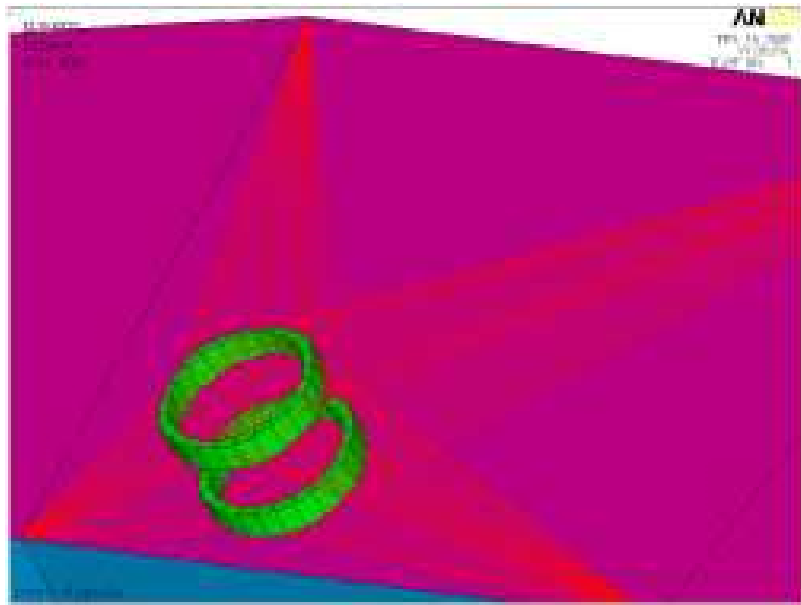


Figure F.3: Detail of cryostat/light restraint interface.

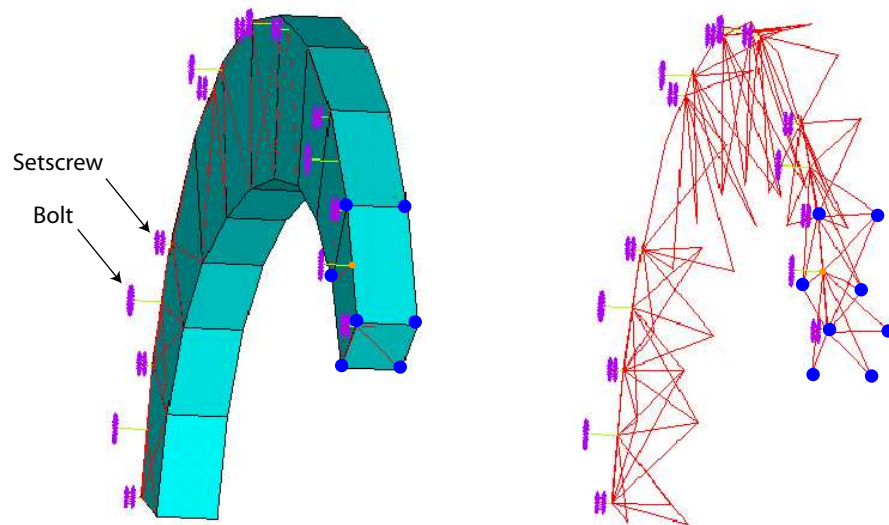


Figure F.4: Detail of light restraint/cold mass interface. For every screw a network of beams connects the screw extremity node (orange dot) to the 8 nodes (blue dots) of the closest tetrahedral element.

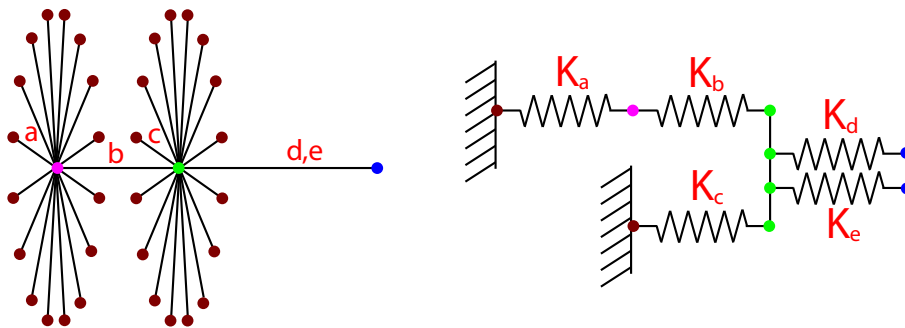


Figure F.5: Setscrew equivalent spring model.

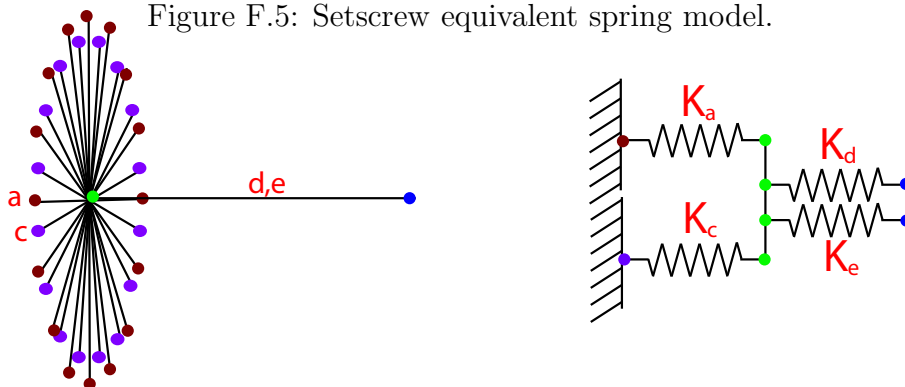
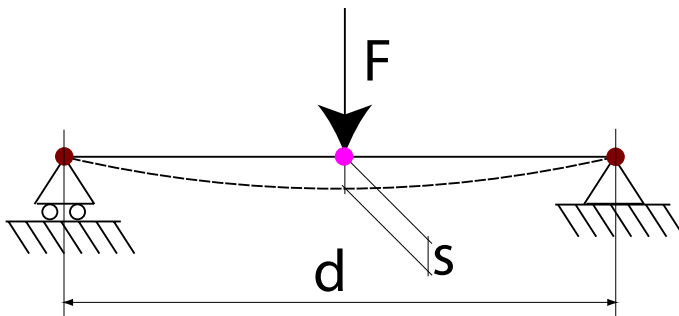


Figure F.6: Bolt equivalent spring model.

Fig. F.4.

On the restraint interface with the cryostat we created sets of beams connecting each node of the hole top and bottom edge with the closest node on the cryostat flange (Fig. F.3).

To avoid coarse errors in the analyses we want now to estimate the longitudinal rigidity of the screws, given by the beams in the body and in the radial sets that connect the screw body to the solid plate. To study the longitudinal rigidity we define an equivalent spring system for each type of screw. In Fig. F.6 and F.5 the beam models are shown along with the equivalent spring system. The spring stiffness constants K_i are obtained for the beams b, d and e as their longitudinal rigidity given

Figure F.7: Equivalent stiffness of radial beams $K = F/s$.

by:

$$K = \frac{EA}{l} \quad (\text{F.1})$$

where: E is the material Young's modulus, A is the cross-section area and l is the beam length. For the set of radial beams a and c the equivalent stiffness constant is given by the force/displacement ratio considered in the center of the radial set. Each single beam is deflected as shown in Fig. F.7 and the force/displacement (F/s) relation is given by:

$$s = \frac{1}{48} \frac{Fl^3}{EJ} \quad (\text{F.2})$$

$$K = \frac{48EJ}{l^3} \quad (\text{F.3})$$

Where: l is the beam length (equal to the hole diameter), E is the Young's modulus, J is the inertia momentum of the beam cross section. As all the 12 beams in each radial set work in parallel, the equivalent elasticity is given by the sum of all the beam contributions.

Table F.1: Geometrical properties of setscrew equivalent beam system.

Set	A [m ²]	J [m ⁴]	l [m]
a	$1.54 \cdot 10^{-5}$	$1.89 \cdot 10^{-9}$	$12 \cdot 10^{-3}$
b	$1.54 \cdot 10^{-5}$	$1.89 \cdot 10^{-9}$	$3 \cdot 10^{-3}$
c	$1.54 \cdot 10^{-4}$	$1.89 \cdot 10^{-9}$	$12 \cdot 10^{-3}$
d	$1.54 \cdot 10^{-5}$	$1.89 \cdot 10^{-9}$	$4.9 \cdot 10^{-3}$
e	$1.54 \cdot 10^{-4}$	-	$4.9 \cdot 10^{-3}$

The resultant longitudinal stiffness for the setscrews is the one of the equivalent spring system shown in Fig. F.5:

$$K_{eq} = \left(\frac{1}{\left(\frac{1}{\frac{1}{K_a} + \frac{1}{K_b}} \right) + K_c} + \frac{1}{K_d + K_e} \right)^{-1} \quad (\text{F.4})$$

The resultant longitudinal stiffness for the bolts is the one of the equivalent spring system shown in Fig. F.6:

$$K_{eq} = \left(\frac{1}{\frac{1}{K_a + K_c}} + \frac{1}{K_d + K_e} \right)^{-1} \quad (\text{F.5})$$

Table F.2: Geometrical properties of bolt equivalent beam system.

Set	A [m ²]	J [m ⁴]	l [m]
a	$1.54 \cdot 10^{-5}$	$1.89 \cdot 10^{-9}$	$14 \cdot 10^{-3}$
c	$1.54 \cdot 10^{-4}$	$1.89 \cdot 10^{-9}$	$15.4 \cdot 10^{-3}$
d	$1.54 \cdot 10^{-5}$	$1.89 \cdot 10^{-9}$	$16.9 \cdot 10^{-3}$
e	$1.54 \cdot 10^{-4}$	-	$16.9 \cdot 10^{-3}$

According to the beam element dimensions given in Table F.1 for the setscrews and in Table F.2 for the bolts, the stiffness values are:

$$K_{setscrews} = 6.06 \cdot 10^9 \frac{N}{m} \quad K_{bolts} = 1.84 \cdot 10^9 \frac{N}{m} \quad (F.6)$$

This values are in good agreement with the expected values, respectively:

$$K_{setscrews} = 6.30 \cdot 10^9 \frac{N}{m} \quad K_{bolts} = 1.82 \cdot 10^9 \frac{N}{m} \quad (F.7)$$

Derived from beam theory and computed accordingly to Eq. F.1.

Appendix G

Montecarlo based multi-station measurement simulation

In this appendix we will provide some more details on the algorithm we implemented to simulate the accuracy intrinsic in the measurement procedure followed to check the respect of the geometrical tolerances imposed on the cold mass shape. In the so-called multi-station measuring procedure, the object shape is acquired from the laser tracker positioned in different spots (Stations) around the object. The measurements are then combined together through a set of fixed point called network that is measured from each station along with the cold mass. In the simulation we consider the measurement of a single aperture in one plane and from two stations we also neglect diffraction phenomena in the aperture. The measurement simulation for each point (belonging to the network or to the cold mass) is based on the random extraction from a normal distribution whose mean value is the theoretical point position and whose dispersion is proportional to the laser tracker distance (according to laser tracker specifications). The cold mass shapes measured from two different stations are then merged in a same reference system through the superposition of the network points measured from the two stations. The network point superposition, that in the real measurement is performed by a routine embedded in the laser tracker acquisition software and called ‘bundle’, has been implemented as a least square fit of the two network point positions. After the network point measurement the laser tracker position is changed by a random shift extracted from a normal distribution with mean zero and *rms* of ± 0.1 mm, to take in to account erratic movements associated to the machine accommodation on the ground.

Legend:

Leica= Laser Tracker

G.C.S.= Global Coordinate System

L1 C.S.= Station 1 Coordinate System

L2 C.S.= Station 2 Coordinate System

$[M_{L1}]$ = transf. matrix from G.C.S. to L1 C.S.

$[M_{L2}]$ = transf. matrix from G.C.S. to L2 C.S.

$[M_{L1}] p_{si}$ = Ideal i^{th} axis point in L1 C.S.

$[M_{L2}] p_{sj}$ = Ideal j^{th} axis point in L2 C.S.

$[M_{L1}] p_{Nj}$ = Ideal j^{th} network point in L1 C.S.

$[M_{L2}] p_{Nj}$ = Ideal j^{th} network point in L2 C.S.

P_{L1i} = i^{th} axis point measured from Station1

P_{L2i} = i^{th} axis point measured from Station2

P_{L1Nj} = j^{th} network point measured from Station1

P_{L2Nj} = j^{th} network point measured from Station2

α = Laser tracker accuracy (5 p.p.m.)

$[M_{L2L1}]$ = transf. matrix from L2 C.S. to L1 C.S.

P_{L2L1i} = i^{th} axis point measured from Station2 and referred to L1 C.S.

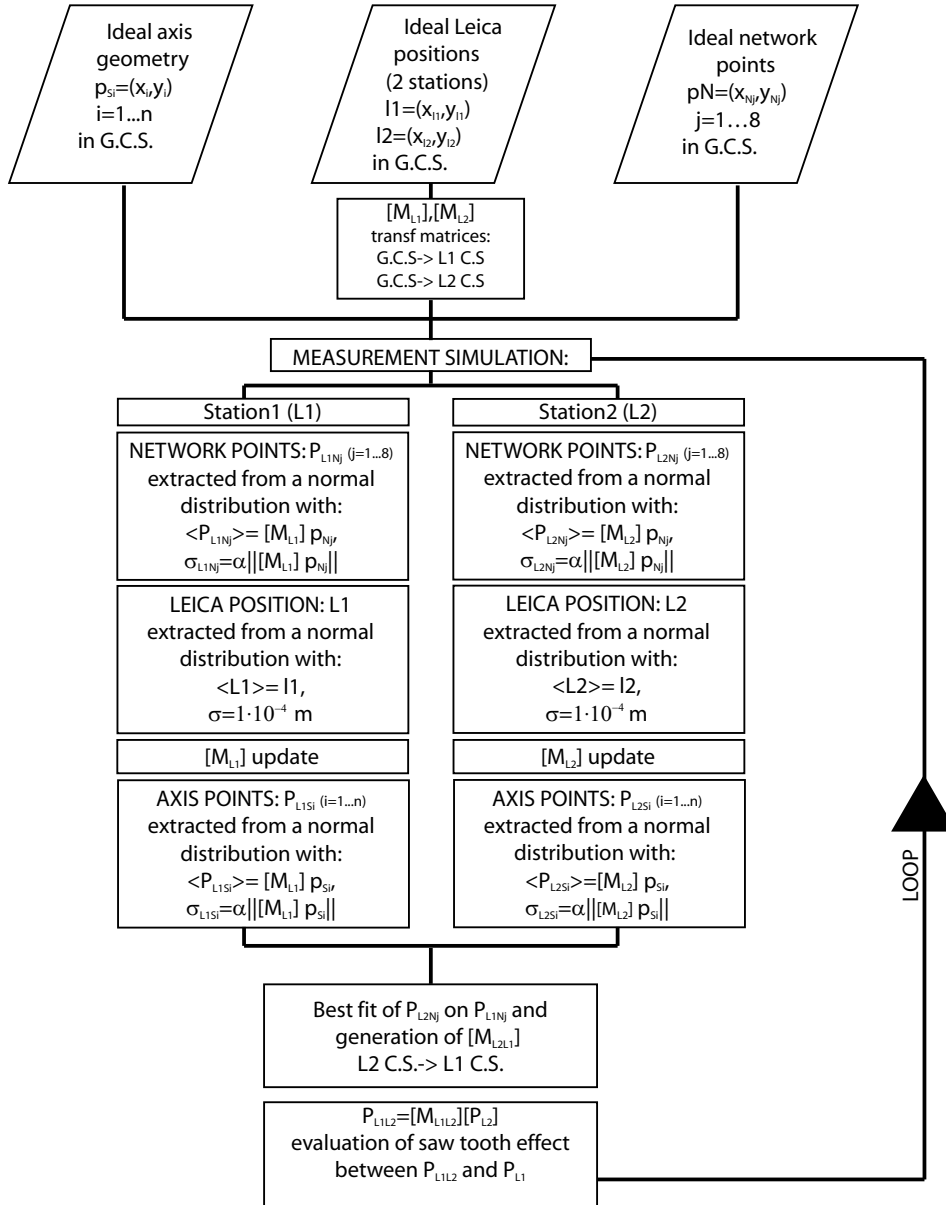


Figure G.1: Algorithm flowchart.

Bibliography

- [1] “Superconducting accelerator magnet”, CD-ROM Tutorial, published by MJB Plus, Inc, 1998. For information see www.mjb-plus.com.
- [2] H. Hirabayashi, *et al.*, “A design proposal for high field dipole magnet”, *KEK-81-1*, June 1981.
- [3] “The Large Hadron Collider, Conceptual design”, *CERN/AC/95-05*, October 1995.
- [4] R. Gupta, “A common coil design for high-field 2-in-1 accelerator magnets”, *PAC’97 1997 Particle Accelerator Conference*, Vancouver, Canada.
- [5] P. McIntyre, W. Shen, R. Scanlan, “16-Tesla block coil dipole for future Hadron Colliders”, 1995 Particle Accelerator Conference, Dallas, USA.
- [6] H. Wiedemann, “Particle Accelerator Physics I”, Springer.
- [7] K.-H. Mess, P. Schmuser, S. Wolff, “Superconducting Accelerator Magnets”, World Scientific, 1996.
- [8] D. Leroy, G. de Rijk, “The iron yoke and the quality of the magnetic field in twin-aperture LHC dipoles”, *CERN-SPS-89-37*, also in *LHC-note-106*, CERN 1989.
- [9] W. Scandale, M. Bajko, F. Savary, “Geometry and Alignment Requirements for the LHC Main Dipole”, *EPAC2000 7th European Particle Accelerator Conference*: pp. 2160-2162.
- [10] C. Garion, B. Skoczen, “Forces in the LHC interconnections”, CERN LHC CRI Technical Note 2002-05, CERN 2005.
- [11] R. Bartolini and W. Scandale, “Multipole feed-down due to dipole misalignments”, CERN-LHC-MMS Internal Note 97-12, CERN 1997.
- [12] ANSYS User’s Manual for Revision 5.3, Swanson Analysis System Inc., Houston.

- [13] M. La China *et al.*, “A Method to Determine the Flexural Rigidity of the Main Dipole for the Large Hadron Collider” *IEEE Trans. Appl. Supercond.*: 13 (2003) no. 2, pp.1305-1308, also in: CERN-LHC Project Report 622, CERN 2002.
- [14] M. La China, B. Bellesia, W. Scandale, “Influence of Test Bench Planarity on Field Orientation Measurement in the LHC Main Bending Dipole”, CERN-LHC Project Note 390, CERN 2006.
- [15] D. Simek, V. Parma, “Dipole Support Post Mechanical Tests”, AT-CRICA/DS/mll, CERN 2003.
- [16] P. Ferracin, “Mechanical and magnetic analysis of the Large Hadron Collider main dipole”, 2002 Geneva : CERN, 120 p. [CERN-THESIS-2002-009]
- [17] P. Ferracin, “Comportamento strutturale e qualita’ di campo delle bobine dei dipoli per LHC : studio e confronto con i risultati sperimentali”, 1998 Geneva : CERN, 106 p. [CERN-THESIS-2002-018]
- [18] P. Tropea, “The CERN-LHC superconducting dipole : assembly and cool-down deformation influence on the magnetic field quality” Geneva: CERN, 118 p. [CERN-THESIS-2002-011]
- [19] K. Couturier, P. Ferracin, W. Scandale, E. Todesco, D. Tommasini, “Elastic Modulus Measurements of the LHC Dipole Superconducting Coil at 300 K and at 77 K”, *AIP Conf. Proc.* 613 (2002) pp. 377-382, also in: CERN-LHC Project Report 514, CERN 2001.
- [20] P. Ferracin, W.Scandale, E. Todesco , D. Tommasini “Thermal Contraction Measurements of the Superconducting Coil of the Main Magnets for the Large Hadron Collider” *AIP Conf. Proc.*: 613 (2002) pp. 372-376, also in: CERN-LHC Project Report 513, CERN 2001.
- [21] P. Ferracin, W. Scandale, E. Todesco, D. Tommasini, “Modeling of Coil Pre-stress Loss During Cool-down in the Main Dipoles of the Large Hadron Collider” *IEEE Trans. Appl. Supercond.*: 12 (2002) no. 1, pp.1705-1708, also in: CERN-LHC Project Report 534, CERN 2002.
- [22] P. Ferracin P, P. Rastogi, W. Scandale, E. Todesco, P. Tropea, “Analysis of conductor displacements in the coil of the LHC main dipole by speckle interferometry” *IEEE Trans. Appl. Supercond.*: 12 (2002) no. 1, pp. 1709-1712, also in: CERN-LHC Project Report 546, CERN 2002.
- [23] E. Y. Wildner, J. Beauquis, G. Gubello, M. La China, W. Scandale, “The Geomtry of the LHC Main Dipole”, *EPAC2004 9th European Particle Accelerator Conference*: pp. 1648-1650.

- [24] F. Seyvett *et al.*, “Improvement of the Geometrical Stability of the LHC cryo-dipoles when Blocking the Central Support Post”, CERN-LHC Project Report 832, CERN 2005.
- [25] M. Bajko, A. Pardons, F. Savary, “Metrology of the LHC Dipole Cold Masses” *IEEE Trans. Appl. Supercond.*: 12 (2002) no. 1, pp.1718-1722, also in: CERN-LHC Project Report 538, CERN 2002.
- [26] LEICA Geosystem AG, The principle of a three-dimensional laser tracker.
- [27] M. Bajko, private communication, 2003.
- [28] *Technical Specifications for the Supply of 1158 Cold Masses of the Superconducting Dipole Magnets for the LHC collider* LHC-MB-CI-0006, CERN 2001.
- [29] N. Bourcey, “Test of the PTFE coating on a sliding support post bearing of the dipole vacuum vessel”, CERN Test Report F388/EC/TR, edms n. 364191.
- [30] A. Buenaventura, D. Bozzini, B. Skoczen, “Dynamic tests of the LHC 15 m Cryo-Dipole (MBP1A1)” CERN-LHC-CRI Technical Note 99-03, CERN 1999.
- [31] O. Capatina, K. Artoos, O. Calvet, “Experimental modal analysis and acceleration measurements during surface transport of a LHC Cryo-Dipole”, CERN-LHC-CRI Technical Note 2002-07, CERN 2002.
- [32] K. Artoos, N. Bourcey, O. Capatina, “Acceleration and support posts deformation measurements during surface transport of a LHC Cryo-Dipole”, CERN-LHC-CRI Technical Note 2002-13, CERN 2002.
- [33] K. Artoos, O. Capatina, “Road Transport of Single LHC Dipole Cryomagnet”, CERN-LHC-LB-ES-0001, CERN 2003.
- [34] M. Mathieu, T. Renaglia, C. Disdier, “Supporting System for the LHC Cold Mass”, CERN-LHC Project Report 139, CERN 1997.
- [35] A. Alzina, “Comportement en fluage du pied central d’un Cryo-Dipole soumis un chargement transversal exceptionnel”, CERN-AT-CRI Technical Note 2003-05, CERN 2003.
- [36] A. Buenaventura, “Transport of the LHC Cryo-Dipoles”, CERN-LHC Project Note 236, CERN 2000.
- [37] F. Seyvet, L. Perrollaz, “Montage et demontage des renforts d’extremities pour le transport”, LHC-QBA-AP-0001, CERN 2004.
- [38] O. Calvet, C. Hauviller, “Analyse du comportement mecanique des Cryo-Dipoles du LHC - 2eme partie : dynamique”, CERN-LHC-CRI Technical Note 2002-12, CERN 2002.

- [39] O. Capatina, “FE Analysis of dipole transport end restraints”, CERN-LHC-CRI Internal Note 2002-01, CERN 2002.
- [40] A. Poncet, private communication, 2004.
- [41] V. Parma, “Load Carrying capacity of the LHC dipole supports”, *Workshop on Main Dipole Geometry and Instability Issues*, CERN, 16 Mar 2004.
- [42] T. Colombet, “Etude de l’influence et de la resistance des brides legeres face au roulis du cryostat”, CERN-AT-CRI Technical Note 2005-04, CERN 2005.
- [43] Saban R. *et al.* “The commissioning of the LHC test string2”, *IEEE Particle Accelerator Conference PAC '01*, Chicago, IL, USA , 18-22 Jun 2001,p. 189.
- [44] P. Lebrun, L. Serio, L. Tavian, R. Van Weelderen, “Cooling Strings of Superconducting Devices below 2 K : the Helium II Bayonet Heat Exchanger”, CERN-LHC Project Report 144, CERN 1997.
- [45] J. Billan *et al.*, “Development of a Displacement Sensor for the CERN-LHC Superconducting Cryodipoles”, CERN-LHC Project Report 463.- Geneva : CERN, 2 Feb 2001 Published in: *Meas. Sci. Technol.*: 12 (2001), pp. 887-896.
- [46] B. Glisic, D. Inaudi, P. Kronenberg, S. Lloret, S. Vurpillot, *Special sensor for deformation measurements of different construction materials and structures*, SPIE 3670 (1999), pp. 505-513.
- [47] P. Lebrun, G. Riddone, L. Tavian, U. Wagner, “Cooldown and Warmup Studies for the Large Hadron Collider”, *17th International Cryogenic Engineering Conference ICEC 17*, Bournemouth, UK, 14-17 Jul 1998, pp. 813-816. Also in CERN-LHC Project Report 214, CERN 1998.
- [48] S. Aznar *et al.*, “Optical In-Situ Measurement of Relative Deformations of the LHC Main Dipole Cold Masses”, *IEEE Trans. Appl. Supercond.*: 12 (2002) no. 1, pp.1736-1740 also in: CERN-LHC Project Report 542, CERN 2002.
- [49] S. Timoshenko and J.N. Goodier, “Theory of elasticity”, 3d ed., New York, McGraw-Hill, 1970.
- [50] J.S. Przemieniecki, “Theory of Matrix Structural Analysis”, Paperback, 1985.